UNIVERSITÀ DEGLI STUDI DI TRIESTE

UNIVERSITÀ DEGLI STUDI DI TRIESTE

XXXVIII CICLO DEL DOTTORATO DI RICERCA IN SCIENZE DELLA RIPRODUZIONE E DELLO SVILUPPO

Finanziato dall'Unione europea - NextGenerationEU
Funded by the European Union - NextGenerationEU

IN VITRO CELLULAR MODELS TO INVESTIGATE MYO5B ROLE IN PROGRESSIVE FAMILIAL INTRAHEPATIC CHOLESTASIS

Settore scientifico-disciplinare: **MED/03**

DOTTORANDA
CECILIA DEL VECCHIO

COORDINATORE
PROF. ADAMO PIO D'ADAMO

SUPERVISORE DI TESI
PROF. ADAMO PIO D'ADAMO

CO-SUPERVISORA DI TESI
DOTT.SSA MARIATERESA DI STAZIO

ANNO ACCADEMICO 2024/2025

Finanziato dall'Unione europea NextGenerationEU | Ministero dell'Università e della Ricerca | Italiadomani PIANO NAZIONALE DI RIPRESA E RESILIENZA | UNIVERSITÀ DEGLI STUDI DI TRIESTE

UNIVERSITÀ
DEGLI STUDI
DI TRIESTE

UNIVERSITÀ DEGLI STUDI DI TRIESTE

XXXVIII CICLO DEL DOTTORATO DI RICERCA IN SCIENZE DELLA RIPRODUZIONE E DELLO SVILUPPO

Finanziato dall'Unione europea - NextGenerationEU
Funded by the European Union - NextGenerationEU

IN VITRO CELLULAR MODELS TO INVESTIGATE MYO5B ROLE IN PROGRESSIVE FAMILIAL INTRAHEPATIC CHOLESTASIS

Settore scientifico-disciplinare: **MED/03**

DOTTORANDA
CECILIA DEL VECCHIO

COORDINATORE
PROF. ADAMO PIO d'ADAMO

SUPERVISORE DI TESI
PROF. ADAMO PIO d'ADAMO

CO-SUPERVISORA DI TESI
DOTT.SSA MARIATERESA DI STAZIO

ANNO ACCADEMICO 2024/2025

Finanziato dall'Unione europea NextGenerationEU | Ministero dell'Università e della Ricerca | Italiadomani | UNIVERSITÀ DEGLI STUDI DI TRIESTE

PREFACE

This PhD project was conducted in accordance with the requirements of the School of Reproductive and Developmental Sciences at the University of Trieste, Cycle XXXVIII. The scholarship was funded by Italian Recovery and Resilience Plan (PNRR) – NextGeneration EU. The work was mainly performed at the Department of Medical Genetics at IRCCS "Burlo Garofolo" for Maternal and Child Health, Trieste, Italy, under the supervision of professor Adamo Pio d'Adamo. Part of the experiments were conducted at the Translational Hepatology and Stem Cell Biology group guided by prof. Tobias Cantz at Hannover Medical School, Hannover, Germany. Some of the analyses presented in this work were performed in collaboration with the research group of Dr. Cristina Bellarosa at the Italian Liver Foundation, Innovative Models Unit, Trieste, Italy.

Table of contents

1. ABSTRACT

Progressive Familial Intrahepatic Cholestasis (PFIC) constitutes a heterogeneous group of severe autosomal recessive genetic liver diseases. These conditions are characterized by defects in biliary secretion that lead to the accumulation of cytotoxic compounds within hepatocytes, resulting in progressive liver dysfunction. Although PFIC was originally attributed to alterations in bile acid transporters, recent evidences have highlighted the crucial role of mutations in genes involved in other cellular processes, such as the maintenance of epithelial barrier integrity, the regulation of gene expression for biliary homeostasis, or intracellular vesicular trafficking.

Among the most recently identified PFIC subtypes is PFIC10, which results from mutations in *MYO5B* gene. This gene encodes for an important actin-associated motor protein that regulates vesicular transport and epithelial cell polarity, therefore essential for proper hepatocyte function. However, the specific pathological mechanisms underlying many *MYO5B* mutations remain poorly understood, partly due to the lack of robust *in vitro* models capable of faithfully replicating hepatocyte polarization and biliary transport.

The present thesis aims to address these challenges by developing a non-invasive patient-specific *in vitro* cellular model designed to investigate and modulate the molecular mechanisms of MYO5B-associated cholestasis.

The initial phase of the study involved generating induced pluripotent stem cells (iPSCs) from healthy controls and patients using two distinct cell sources: renal epithelial cells isolated from urine, reprogrammed via integrative lentiviral method, and peripheral blood mononuclear cells (PBMCs), reprogrammed using non-integrative Sendai virus-based method. To expand the model's potential applications, iPSCs derived from a healthy donor's urine were modified using CRISPR/Cas9 technology to insert a biallelic *MYO5B* mutation previously associated with PFIC.

During the first stage of hepatic model development, we compared two 2D differentiation strategies applied to wild-type urine-derived iPSCs: a protocol based on scientific literature and a commercial ready-to-use kit. Although both protocols produced cells with hepatic morphology and gene expression (hepatocyte-like cells), immunofluorescence analysis conclusively demonstrated that neither strategy was able to induce the correct apico-basal polarization.

Thus, we generated 3D hepatobiliary organoids from both PBMC-derived and epithelial-derived iPSCs. The resulting structures have a polarized spheroidal morphology, characterized by an apical membrane facing the internal canalicular lumen and by a basolateral membrane oriented between cells and along the outer surface. These organoids can resume the biliary transport *in vitro*, which was evaluated employing fluorescently labelled bile acid analogues.

Organoids derived from healthy donor PBMCs showed correct polarization and time-dependent biliary transport. In parallel, we generated a line from PBMCs of a PFIC patient (identified as HC01), whose 3D model successfully recapitulated the key functional defects of the pathology. On the contrary, both wild-type and *MYO5B*-edited epithelial-derived organoids exhibited critical polarization defects. Deeper investigation revealed that these iPSCs, generated with lentiviral integrated method, retained a residual expression of viral transgenes, leading to their exclusion from subsequent phases of the study.

Patient HC01 presented a complex genetic profile, characterized by the co-presence of heterozygous variants in the *ABCB4*, *ABCB11*, and *MYO5B* genes. While these variants individually might not be sufficient to cause the disease, previous studies have shown that genetic correction of the *MYO5B* variant alone is sufficient to restore the phenotype, identifying it as the determining factor of the pathology within a context of oligogenic susceptibility.

Based on this evidence and hypothesizing that the monoallelic *MYO5B* mutation results in a critical functional haploinsufficiency, we attempted a functional restoration of BSEP through the overexpression of wild-type *MYO5B* mRNA, delivered via liver-specific lipid nanoparticles (LNPs). We cloned two isoforms of the *MYO5B* sequence (full-length and an isoform lacking Exon 30) and performed *in vitro* transcription; the resulting mRNA was encapsulated in LNPs. After verifying successful release and translation in a hepatic cell line, HC01 organoids were transfected, and bile acid transport was assessed at 12, 24, and 36 hours.

Transfection with LNPs containing full-length *MYO5B* mRNA resulted in only a minimal increase in BSEP-mediated transport. In contrast, delivery of the isoform lacking Exon 30 (which is supposedly predominant in hepatic tissue) induced a significant, although transient, restoration of BSEP-mediated transport, with a peak effect observed 12 hours post-transfection before declining at later time points. These data demonstrated that mRNA delivery via LNPs represents an effective approach for modulating intracellular processes, while highlighting the need to optimize the duration of the therapeutic effect.

In conclusion, this work developed a patient-specific *in vitro* cellular model based on iPSC-derived organoids for the study of MYO5B-associated Progressive Familial Intrahepatic Cholestasis, proving its validity in recapitulating the functional defects of the disease. Furthermore, the results obtained through LNP-mediated mRNA delivery confirmed this approach as a promising strategy for modulating the cholestatic phenotype, opening perspectives for future therapeutic developments.

2. RIASSUNTO

La Colestasi Intraepatica Familiare Progressiva (PFIC) costituisce un gruppo eterogeneo di gravi patologie genetiche epatiche a trasmissione autosomica recessiva. Tali condizioni sono caratterizzate da difetti nella secrezione biliare che determinano l'accumulo di composti citotossici negli epatociti, conducendo a una progressiva disfunzione d'organo. Sebbene la PFIC sia stata originariamente attribuita ad alterazioni nei trasportatori degli acidi biliari, recenti evidenze hanno messo in luce il ruolo cruciale di mutazioni in geni coinvolti in altri processi cellulari, quali il mantenimento dell'integrità della barriera epiteliale, la regolazione dell'espressione genica per l'omeostasi biliare o il traffico vescicolare intracellulare.

Tra i sottotipi più recentemente identificati figura la PFIC10, causata da mutazioni nel gene *MYO5B*. Tale gene codifica per una proteina motore associata all'actina, fondamentale per la regolazione del trasporto vescicolare e per la polarità delle cellule epiteliali, risultando dunque essenziale per la corretta funzionalità epatica. I meccanismi patogenetici specifici alla base di molte mutazioni di *MYO5B* rimangono tuttavia poco compresi, complice la carenza di modelli *in vitro* robusti in grado di replicare fedelmente la polarizzazione degli epatociti e il trasporto biliare.

Il presente lavoro di tesi si prefigge quindi di colmare tali lacune sviluppando un modello cellulare *in vitro* non invasivo e paziente-specifico, finalizzato all'indagine e alla modulazione dei meccanismi molecolari della colestasi associata a MYO5B.

La fase iniziale dello studio ha previsto la generazione di cellule staminali pluripotenti indotte (iPSCs) da controlli sani e da pazienti, utilizzando cellule da due diverse origini: cellule epiteliali renali isolate da urine, riprogrammate mediante metodo lentivirale integrativo, e cellule mononucleate del sangue periferico (PBMCs), riprogrammate tramite metodo non-integrativo basato sul virus Sendai. Per ampliare le potenziali applicazioni del modello, le iPSCs derivate da urine di un donatore sano sono state modificate mediante tecnologia CRISPR/Cas9 per inserire una mutazione biallelica di *MYO5B* precedentemente associata a PFIC.

In una prima fase di sviluppo del modello epatico, abbiamo eseguito un confronto tra due strategie di differenziamento 2D applicate a iPSCs wild-type derivate da urine: un protocollo basato sulla letteratura scientifica e un kit commerciale *ready-to-use*. Sebbene entrambi i protocolli abbiano prodotto cellule con morfologia ed espressione genica epatica (cellule simil-epatocitarie), l'analisi mediante immunofluorescenza ha evidenziato in modo determinante che nessuna delle due strategie è stata in grado di indurre una corretta polarizzazione apico-basale nelle cellule.

Alla luce di questi risultati, abbiamo generato organoidi epatobiliari 3D partendo sia da iPSCs derivate da PBMCs, sia da quelle di origine epiteliale. Le strutture risultanti hanno mostrato una morfologia sferoide polarizzata, caratterizzata da una membrana apicale rivolta

verso il lume canalicolare interno e da una membrana basolaterale orientata verso l'esterno. La funzionalità di tali organoidi nel ricapitolare il trasporto biliare *in vitro* è stata valutata mediante l'utilizzo di analoghi fluorescenti degli acidi biliari.

Gli organoidi derivati da PBMCs di donatori sani hanno mostrato la corretta polarizzazione e un trasporto biliare tempo-dipendente. Parallelamente, abbiamo generato una linea da PBMCs di un paziente affetto da PFIC (identificato come HC01), il cui modello 3D ha ricapitolato con successo i difetti funzionali chiave della patologia. Al contrario, gli organoidi derivati da iPSCs di origine epiteliale (sia wild-type che editati per *MYO5B*) hanno manifestato critici difetti di polarizzazione. Indagini più approfondite hanno rivelato che tali iPSCs, generate con metodo lentivirale integrativo, mantenevano un'espressione residua dei transgeni virali, motivo per cui sono state escluse dalle fasi successive dello studio.

Il paziente HC01 presentava un profilo genetico complesso, caratterizzato dalla co-presenza di varianti in eterozigosi nei geni *ABCB4*, *ABCB11* e *MYO5B*. Sebbene tali varianti singolarmente possano non essere sufficienti a causare la malattia, studi precedenti hanno dimostrato che la correzione genica della sola variante in *MYO5B* è sufficiente a ripristinare il fenotipo, identificandola come il fattore determinante della patologia in un contesto di suscettibilità oligogenica.

Basandosi su queste evidenze, e ipotizzando che la mutazione monoallelica di *MYO5B* determini un'aploinsufficienza funzionale critica, abbiamo tentato un ripristino funzionale di BSEP tramite la sovraespressione di mRNA di *MYO5B* wild-type. Quest'ultimo è stato veicolato da nanoparticelle lipidiche (LNPs) con tropismo epatico. Abbiamo clonato due isoforme della sequenza di *MYO5B* (full-length e una isoforma priva dell'Esone 30) ed eseguito la trascrizione *in vitro*; l'mRNA risultante è stato incapsulato nelle LNPs. Dopo aver verificato il corretto rilascio e la traduzione in una linea cellulare epatica, gli organoidi di HC01 sono stati trasfettati, valutando il trasporto degli acidi biliari dopo 12, 24 e 36 ore.

La trasfezione di LNPs contenenti mRNA di *MYO5B* full-length ha determinato solo un minimo incremento del trasporto mediato da BSEP. Invece, la veicolazione dell'isoforma priva dell'Esone 30 (presumibilmente predominante nel tessuto epatico) ha indotto un significativo ripristino del trasporto mediato da BSEP, sebbene transitorio, con un picco di efficacia a 12 ore post-trasfezione seguito da un declino ai tempi successivi. Questi dati dimostrano che la veicolazione di mRNA mediante LNPs rappresenta un approccio efficace per modulare i processi intracellulari, evidenziando al contempo la necessità di ottimizzare la durata dell'effetto terapeutico.

In conclusione, in questo lavoro abbiamo sviluppato un modello cellulare *in vitro* paziente-specifico basato su organoidi derivati da iPSCs per lo studio della Colestasi Intraepatica Familiare Progressiva associata a MYO5B, dimostrando la sua validità nel ricapitolare i difetti funzionali della patologia. Inoltre, i risultati ottenuti mediante veicolazione di mRNA attraverso LNP confermano questo approccio come una strategia promettente per la modulazione del fenotipo colestatico, aprendo prospettive per futuri sviluppi terapeutici.

3. INTRODUCTION

3.1. Overview of liver anatomy and bile production

The liver represents a complex metabolic organ and the biggest gland of the human organism, performing several crucial functions and relying on an organized structure; among its most critical physiological roles is the production and secretion of bile, a process responsible for the emulsification of dietary fats and for the primary excretory pathway for cholesterol, bilirubin, and potentially toxic metabolic products (Krishna 2013; Di Ciaula et al. 2017).

The efficacy of this secretory function is connected to the liver's anatomical architecture and the polarization of its main epithelial cells, the hepatocytes; these cells exhibit a polygonal geometry, organized to have the highest possible contact with the sinusoidal blood supply while simultaneously forming the bile lumen (or canaliculus) as a space between two adjacent hepatocytes, whose apical membranes are strongly sealed by tight junctions (Boyer 2013).

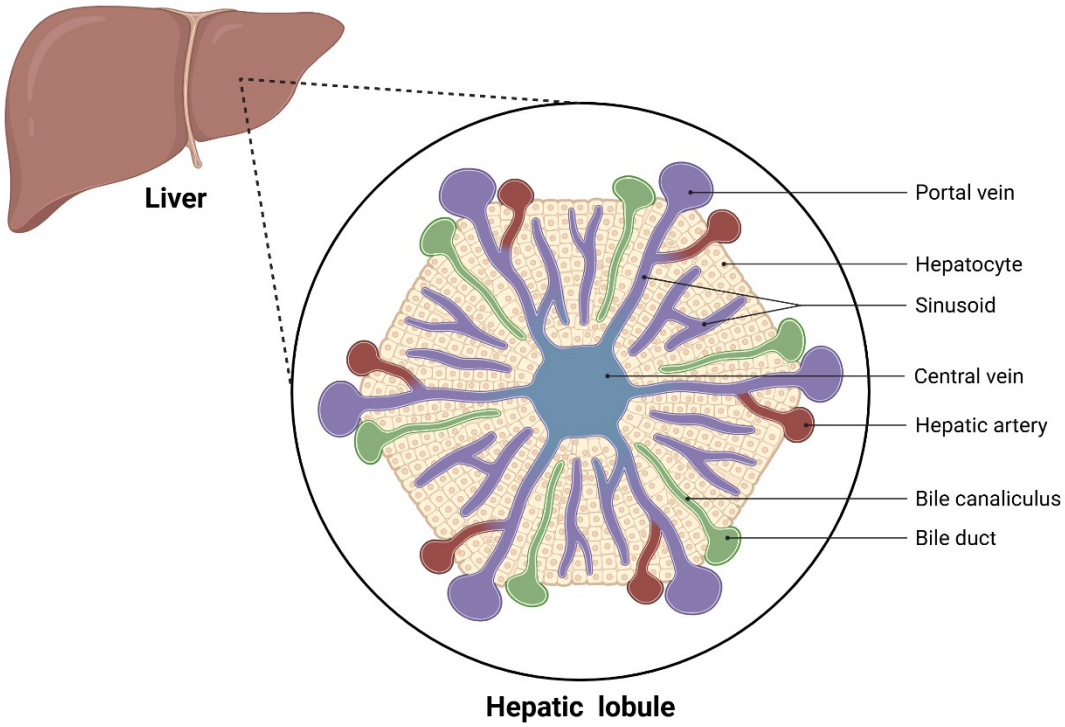

Figure 1: Representation of the human liver lobule, picture created in https://BioRender.com.

The liver parenchyma is organized into functional units, named lobules, that optimize the bidirectional exchange of substrates between the blood and the hepatocytes (Figure 1). Lobules can be described as hexagonal structures, where a central vein is devoted to collect blood from the organ, and at the corners of the structure lies a portal vein from the intestine, an artery branch to deliver oxygenated blood, and a bile duct, which is the results of the convergence of the intricate network of bile canaliculi. In the lobules, blood flows from the periphery to the

centre, while the bile produced by the hepatocytes flows on the opposite direction from the canaliculi towards the bile ducts; this counter-current flow ensures that the bile is moved away from the direction of venous drainage (Boyer 2013).

The bile is a complex aqueous solution containing endogenous solutes such as bile acids, phospholipids, cholesterol or bilirubin, as well as exogenous molecules to be excreted. Bile acids (BAs) are amphipathic cholesterol derived molecules, produced and metabolized by the hepatocytes and presents as the most abundant solute in the bile. The main role of BAs is the intestinal absorption of lipids and fat-soluble vitamins, but these molecules also have a function in endocrine signalling pathways by activating receptors able to modulate lipid, glucose, and energy metabolism. Two main primary BAs are described, cholic acid (CA) and chenodeoxycholic acid (CDCA), both of which are further conjugated with taurine or glycine. The gut microbiota metabolizes BAs into secondary or tertiary bile acids; in the distal intestine BAs are almost entirely reabsorbed and enter the enterohepatic circulation system (Boyer 2013; Di Ciaula et al. 2017; Fleishman and Kumar 2024).

The movement of BAs across the hepatocyte membranes is mediated by a coordinated system of transport proteins located on the sinusoidal (or basolateral) and canalicular (or apical) membranes (Figure 2); therefore, this system relies on the polarity of hepatocytes and the characterization of two distinct membranes. Transporters located on the basolateral membrane mediate the uptake of BAs and other organic solutes from the blood: Sodium-Taurocholate Cotransporting Polypeptide (NTCP) is the key transporter of conjugated BAs from portal blood, while Organic Anion Transporting Polypeptides (OATPs family), specifically OATP1B1 and OATP1B3 in the human liver, preferably transport unconjugated BAs. On the

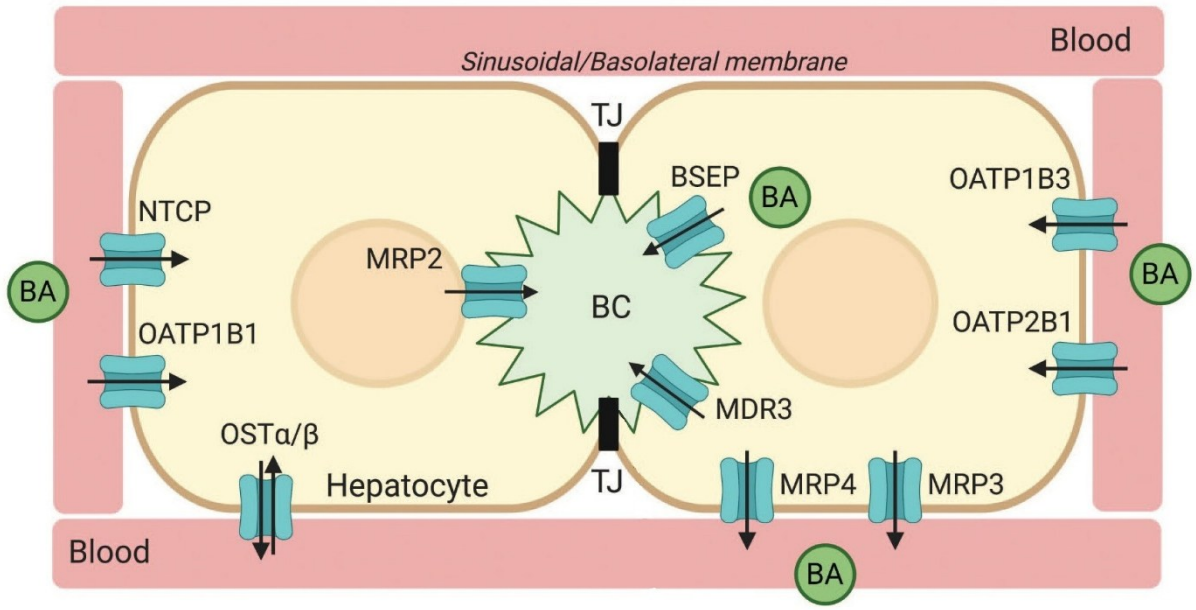

Figure 2: Representation of bile acid (BA, green circles) transport in the hepatocytes; adapted from Saran and Brouwer, 2023. Between two hepatocytes (in yellow) is the bile canaliculi (BC) sealed by tight junction (TJ, in black); surrounding the hepatocytes the blood vessels, which delimitates the basolateral membrane.

canalicular membrane the ATP-dependent export pumps are responsible for the secretion of BAs in the bile lumen; Bile Salt Export Pump (BSEP) and Multidrug Resistance-associated Protein 2 (MRP2) regulate the movement of BAs through this membrane (Saran and Brouwer 2023; Fleishman and Kumar 2024).

3.2. Progressive Familial Intrahepatic Cholestasis (PFIC)

Progressive Familial Intrahepatic Cholestasis (PFIC) is a heterogeneous group of autosomal recessive diseases defined by severe defects in the mechanisms regulating bile secretion in hepatocytes. The patients carrying this disease manifest problems in the bile flow, leading to an accumulation of toxic compounds in the hepatocytes and therefore cytotoxicity and liver disfunction (Bull and Thompson 2018; Hassan and Hertel 2022).

PFIC is usually diagnosed early in life, with clinical manifestation including persistent jaundice, debilitating pruritus, hepatosplenomegaly, malabsorption of fat-soluble vitamins and profound fatigue. The therapeutic approaches usually aim to alleviate these symptoms, however the progression of these disorders often leads to the development of cirrhosis and terminal liver failure during late childhood, highlighting the necessity for deep investigation on the mechanism of this disease (Pinon and Kamath 2024).

The overall incidence of PFIC is described to be between 1 in 50.000 and 1 in 100.000 births; nevertheless, epidemiological data, while limited, suggest that PFIC accounts for a considerable portion of childhood liver disease. Studies utilizing genetic diagnostics have estimated that PFIC is responsible for approximately 10% to 15% of diagnosed cases in infants and children presenting with cholestasis (Baker et al. 2019).

PFIC can be classified according to the gene carrying the mutation; most of the genes involved encode for bile acid transporters, both for the uptake on the basal hepatocyte membrane and for the secretion in the canaliculi through the hepatocyte apical membrane (Bull and Thompson 2018). Historically, PFIC was classified into three primary subtypes (PFIC types 1, 2, and 3); however, the advancements in high-throughput genetic testing over the last decade have dramatically expanded this classification, documenting numerous additional types and demonstrating that defects in regulatory or trafficking machinery are equally relevant to core transporter failures (Hassan and Hertel 2022). PFIC classification with associated genes and encoded protein main function can be found in Table 1.

Table 1: PFIC genetic classification. Adapted from OMIM® - Online Mendelian Inheritance in Man® (https://omim.org/entry/211600) and GeneCards database (https://www.genecards.org).

PHENOTYPE	GENE	LOCATION	PROTEIN	MAIN FUNCTION
Progressive familial intrahepatic cholestasis 1	ATP8B1	18q21.31	FIC1	Translocase, maintenance of the canalicular membrane integrity.
Progressive familial intrahepatic cholestasis 2	ABCB11	2q31.1	BSEP	Secretion of major hydrophobic bile salts.
Progressive familial intrahepatic cholestasis 3	ABCB4	7q21.12	MDR3	Floppase, phospholipid efflux translocator.
Progressive familial intrahepatic cholestasis 4	TJP2	9q21.11	ZO-2	Component of the tight junction barrier.
Progressive familial intrahepatic cholestasis 5	NR1H4	12q23.1	FXR	Transcription factor, regulates the expression of genes involved in bile acid synthesis and transport.
Progressive familial intrahepatic cholestasis 6	SLC51A	3q29	OSTα	Intestinal basolateral transporter responsible for bile acid export from enterocytes into portal blood.
Progressive familial intrahepatic cholestasis 7	USP53	4q26	USP53	Modulator of the barrier properties and mechanical stability of tight junctions.
Progressive familial intrahepatic cholestasis 8	KIF12	9q32	KIF12	Kinesin family of microtubule-associated motors; involved in intracellular transport and cell division.
Progressive familial intrahepatic cholestasis 9	ZFYVE19	15q15.1	ANCHR	Key regulator of abscission step in cytokinesis.
Progressive familial intrahepatic cholestasis 10	MYO5B	18q21.1	MYO5B	Involved in vesicular trafficking, participates in epithelial cell polarization.
Progressive familial intrahepatic cholestasis 11	SEMA7A	15q24.1	SEMA7A	Role in integrin-mediated signalling, cell migration regulation and immune response.
Progressive familial intrahepatic cholestasis 12	VPS33B	15q26.1	VPS33B	Role in epithelial cells in the apical recycling pathway and in the maintenance of the apical-basolateral polarity.
Progressive familial intrahepatic cholestasis 13	PSKH1	16q22.1	PSKH1	Regulation of pre-mRNA processing.

3.3. MYO5B protein

Myosin Vb (MYO5B) is a pivotal component of the cell's structural and transport machinery, belonging to the Class V of myosin motor proteins; myosins are actin-associated mechanoenzymes, able to hydrolyse ATP as a source of energy to transform into mechanical movement along actin filaments. This family of proteins can be divided in 12 classes, encoded

by more than 40 genes; myosins involved in muscle movement are called conventional myosins (Class II) while every other – including Class V – are named unconventional myosins. The latter classes are involved in essential cellular processes, such as cell division, cell migration and intracellular endosomal trafficking (Trivedi et al. 2020).

Mammalian Class V of myosins includes three isoforms named Myosin VA, VB and VC; each isoform presents tissue specificity, where MYO5B is mainly expressed in epithelial cells. Myosins V operate as homodimers and possess four key functional domains: the N-terminal motor domain is responsible for generating movement along the filaments, thanks to the actin-binding site and the hydrolysis of ATP; then, lever arms made of 6 IQ motifs are in charge of amplifying the conformational changes, and these are followed by a coil-coil domain for dimerization; lastly, the C-terminal domain is composed by a globular tail which binds to cargo protein with the mediation of small GTPases of the Ras protein family (Q. Li 2023; Bridgman and Ahmed 2009). Figure 3 shows a schematic representation of Class V Myosin structure.

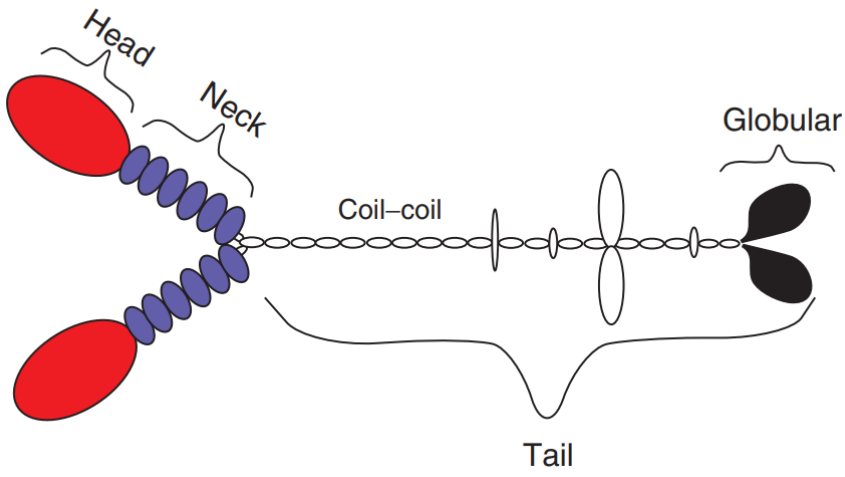

Figure 3: Schematic representation of Class V Myosin proteins; adapted from Bridgman and Ahmed, 2009. From the left: in red the N-terminal motor domain (head), in purple the lever arms (neck), the dimerization domain (coil-coil) and in black the C-terminal globular domain (globular).

The function of MYO5B as a molecular motor is tightly controlled by its interaction with Rab GTPases, which represent the largest family of proteins dedicated to regulating membrane traffic. Rab proteins serve as molecular switches, forming platforms for the assembly of multi-protein complexes on distinct vesicle membranes to regulate specific trafficking pathways (Figure 4). The specificity of MYO5B in regulating alternate trafficking pathways depends critically on the combination with Rab GTPases: the interaction with Rab11a, Rab8a and Rab10 make MYO5B known to be involved in recycling endosomes trafficking. MYO5B role in the intracellular vesicular movement indicates a major role of this protein in maintaining cellular polarity as well, since an impairment of delivery of membrane components to the proper surface is a key factor to discriminate between apical and basolateral membrane (Roland et al. 2011; Q. Li 2023; Duclaux-Loras et al. 2023).

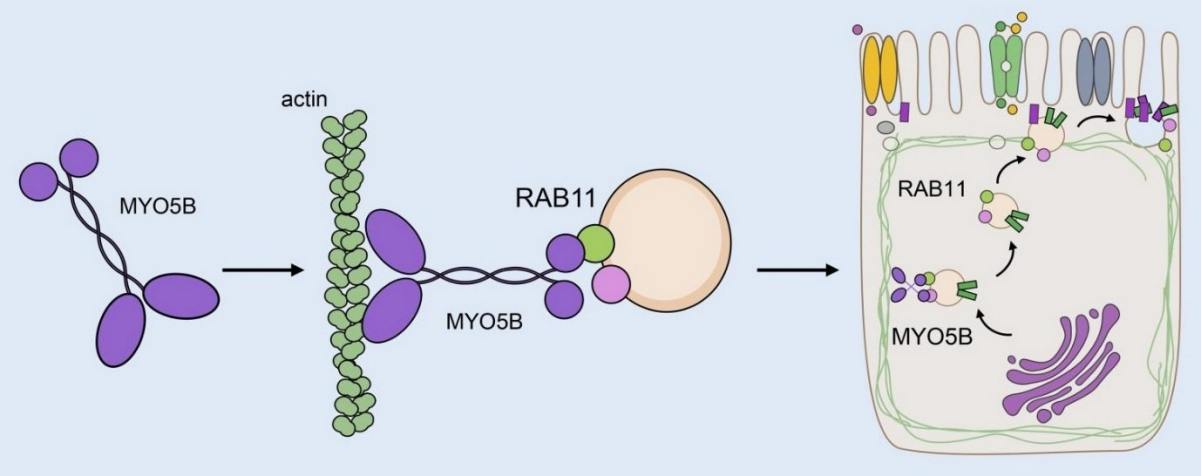

Figure 4: Schematic representation of MYO5B-Rab interaction; adapted from Duclaux-Loras et al. 2023. MYO5B works as a homodimer which binds to actin filament on the motor domain and interacts with Rab proteins (RAB11 in this figure) on the opposite globular domain. Rab proteins mediate the intracellular vesicle binding and the delivery to the cell membrane.

MYO5B gene is located on chromosome 18q21.1 and encodes for 40 exons, translated into a protein composed of 1848 amino acids (Lou et al. 2024). Alternative splicing of the *MYO5B* gene serves as a critical regulatory mechanism that dictates its interaction with specific members of the Rab protein family. This molecular switch provides a sophisticated layer of control, enabling the cell to tailor MYO5B's function to different physiological contexts and trafficking demands (Roland, Lapierre, and Goldenring 2009).

The primary alternative splicing event occurs in the cargo-binding tail region of the MYO5B protein, which includes or exclude a specific region called Exon D, which corresponds to Exon 30; this differential inclusion of a single exon alters the protein's structure and consequently its function, and the impact of this mechanism is made apparent by the highly regulated, tissue-specific expression of these two isoforms (Roland, Lapierre, and Goldenring 2009).

According to a gene expression analysis performed in 2009, only the Exon 30 depleted *MYO5B* isoform is detectable in human liver cDNA (Roland, Lapierre, and Goldenring 2009); this isoform restriction in specialized epithelial tissues is further corroborated by findings that intestinal enterocytes also predominantly express the isoform lacking Exon D (Knowles et al. 2014). This highly regulated, tissue-specific expression seems to imply that the presence or absence of the Exon D-encoded region has critical functional consequences on MYO5B's role in epithelial cell biology, and therefore for MYO5B interaction with Rab GTPases. Indeed, the study mentioned above has shown that Rab10 interaction with MYO5B is dependent on the presence of Exon D, Rab8a binds only if Exon D is lacking, while Rab11a appears to be able to bind MYO5B independently (Roland, Lapierre, and Goldenring 2009).

However, these findings about *MYO5B* splicing and associated connection with Rab family GTPases in the liver tissue are still not deepen investigated and confirmed, thus should still be considered hypothesis.

Given MYO5B important role in the cell, mutations on these gene are associated with disease onset; the first described associated disorder is MVID, Microvillus Inclusion Disease, where severe loss-of-function *MYO5B* mutations lead to the development of this genetic rare intestinal condition characterized by severe diarrhea and malnutrition in newborns. Enterocytes of MVID patients display a complete loss of cell polarity and presents intracellular inclusions of apical membrane components; patients are inevitably bound to lifetime parenteral nutrition or to intestine and liver transplant to treat the symptoms. With the progression of the disease, MVID patients can develop cholestasis, often recurrent and chronic; interestingly, several cholestatic patients have been reported with *MYO5B* mutations (mostly missense) and no intestinal involvement, indicating that these gene, and thus mutation on its sequence, are also associated with PFIC and bile flow impairments (Bowman et al. 2025).

3.4. PFIC 10 – *MYO5B* associated

PFIC10, originally referred to as PFIC6, has been associated to mutation on *MYO5B* gene; it presents primarily as an isolated cholestasis, characterized by neonatal or infantile jaundice (often transient), severe chronic pruritus, and hepatomegaly (Roquelaure et al. 2025). Clinically, PFIC10 phenotype typically lacks the defining intestinal pathology and intractable diarrhea associated with MVID (Vitale et al. 2025), it is biochemically characterized instead by low to normal levels of gamma-glutamyl transferase (GGT) and elevated serum bile acid concentrations; the clinical course of PFIC10 patients is generally noted to be milder than that observed in other subtype, such as PFIC2 (Roquelaure et al. 2025).

The exact incidence of PFIC10 is difficult to quantify precisely due to its recent identification and phenotypic overlapping with other forms of low GTT cholestasis; however, the importance of PFIC10 can be emphasized by the fact that *MYO5B* mutations can explain up to 20% of these previously undiagnosed cases (Matarazzo et al. 2022).

Since MYO5B protein has a role in maintaining hepatocyte polarity and intracellular vesicles trafficking to the proper membrane, the supposed pathogenic mechanism underneath MYO5B-associated cholestasis relies in an altered localisation of bile acid transporters and therefore in an impaired bile flow (Gonzales et al. 2017; Qiu et al. 2017). For example, in Gonzales manuscript from 2017 *Patient 3* presented a homozygous missense mutation on the motor domain (Exon 4) of *MYO5B* gene, and liver biopsies showed an impaired expression and localization of the canalicular transporter BSEP; however, no functional cellular characterization was carried out and no pathological mechanism was hypothesized (Gonzales et al. 2017).

Nevertheless, in a small fraction of PFIC10 patients recent observations have detected a correct BSEP expression and localization (Cockar et al. 2020; Vij and Shah 2022; Matarazzo

et al. 2022), indicating that for some patients with *MYO5B*-associated cholestasis the pathological mechanisms remain uncertain and more investigations are required.

The existence of the two distinct phenotypes – intestinal MVID and liver PFIC10 – associated with mutation on the same gene indicates the presence of an underlying genotype-phenotype correlation. A possible interpretation is that the specific functional defect that dictates the phenotypic outcome must be tissue-dependent or relate to the severity of the MYO5B impairment. It is hypothesized that mutations causing liver-specific PFIC10 are partially functional or result in an isoform whose defect is specifically amplified in the hepatocyte, while retaining sufficient function in enterocytes to prevent the complete collapse of the microvillus brush border characteristic of MVID. On the contrary, complete loss-of-function mutations or severe truncations typically result in the mixed phenotype of MVID accompanied by intrahepatic cholestasis (Zheng et al. 2022; Bowman et al. 2025). This suggests that the study of tissue-specific MYO5B isoforms may be essential to unravel PFIC10 pathological mechanisms.

3.5. *In vitro* models to study cholestasis

The primary requirement for an *in vitro* hepatic model designed to investigate cholestasis is the recapitulation of hepatobiliary transport. This necessitates functional cell polarization, characterized by the establishment of distinct apical and basolateral membranes, which ensures the correct localisation of bile acid uptake and efflux transporters.

3.5.1. Immortalized cell lines and Primary Human Hepatocytes

Immortalized cell lines have been widely used for toxicological research for decades due to their low cost, almost unlimited proliferation, and ease of standardization; however, their application in cholestasis research is limited, mainly because of their transporters' expression.

Nowadays, the most diffuse human liver derived commercial cell lines are HepG2 and HepaRG, derived respectively from hepatoblastoma and liver carcinoma cells. HepG2 are not a valid model to study cholestasis because they do not exhibit stable and reproducible bile canaliculi with correct localisation of the bile acid transporters (Penman et al. 2019). HepaRG cells upon reaching confluence and inducing differentiation form a polarized monolayer of hepatocyte-like and biliary-like cells and can develop functional bile canaliculi; however, their neoplastic origin remains a significant obstacle for studying genetic cholestasis, as they maintain metabolic and morphological deviations from healthy human physiology (Nelson et al. 2017; Le Vee et al. 2006).

The functional limits of the commercial cell lines can be overcome by using Primary Human Hepatocytes (PHH) isolated from liver tissue, which are the reference standard for all

hepatic functions; however, PHH application is challenged by their instability *ex vivo*, because of their fast trend to de-differentiate and their rapid loss of hepatic-like functions and viability (Kaur et al. 2023). These limits can be partially solved with 2D sandwich-cultured hepatocytes, where the inclusion into two layers of extracellular matrix induce the hepatocytes to repolarize and form bile canaliculi (Deharde et al. 2016). Still, the sandwich culture deteriorates after 7-10 days. (Bell et al. 2018).

PHHs have shown to be a valid cell line also for 3D spheroid cultures, where the issues of longevity and phenotypic stability of 2D cultures are partially overcome. PHH are able to spontaneously aggregate in spherical structures, stable for at least 4-5 weeks (Bell et al. 2016). Despite all of this, PHH 3D culture still presents the drawbacks of using primary cells; moreover, PHH have a significant inter-donor variability in protein expression, and therefore a low reproducibility (Gijbels et al. 2019).

3.5.2. iPSCs-derived 2D models

One of the biggest breakthroughs in cellular models was the discovery and development of Induced Pluripotent Stem Cells (iPSCs) in 2006; by reprogramming adult human cells to a pluripotent staminal state, this technology offers an unlimited platform of undifferentiated cells from any individual without surgical procedures. The reprogramming process is driven by the expression of 4 transcription factors, named "Yamanaka factors" (Oct4, Sox2, Klf4, and c-Myc), which conduct a profound remodelling of the cell's epigenetic landscape, gene expression, and metabolism (Takahashi and Yamanaka 2006). The applications of iPSCs are vast and rapidly expanding; these cells can be differentiated towards any adult cell type and exploited as a model for different research fields, such as disease investigation of molecular mechanisms and pathological phenotypes, drug development and screening, specific cell therapy testing in regenerative medicine (Cerneckis, Cai, and Shi 2024).

Somatic cells can be reprogrammed into iPSCs with different methods which can be classified into 2 categories, viral and non-viral; first methods introduce the required reprogramming factors through viral transfection, and the transgenes can be either integrated in the host cell DNA, or they can be transiently expressed in the non-integrating methods. On the other hand, non-viral delivery methods are based mainly on electroporation or nanoparticles, and the reprogramming factors are delivered as nucleic acid (episomal vectors or mRNA) or proteins. The selection of the reprogramming method depends on experiments requirements and laboratory resources; viral methods offer higher efficiency but require specialized facilities, whereas non-viral methods are easier to handle but may suffer from lower reprogramming efficiency (Zahumenska et al. 2020).

As mentioned, iPSCs can be differentiated *in vitro* towards every cell type, including hepatocytes; the process of generating hepatocytes from iPSCs in two-dimensional culture is based on the sequential recapitulation of the signalling events the govern the hepatic

embryogenesis *in vivo*. The first critical step is guiding pluripotent cells out of the undifferentiated state to the definitive endoderm lineage; this can be accomplished *in vitro* by feeding the cells with a mix of small molecules and cytokines able to mimic the signals inducing the epithelial-mesenchymal transition necessary for endoderm formation. Once definitive endoderm is established, cells must be directed to an anterior endoderm and subsequently specified into hepatoblasts, and lastly the cells are pushed towards the maturation into hepatocyte-like cells (HLCs) (Ju et al. 2024).

Despite transcriptomic analyses revealed that iPSCs-derived HLCs are not completely mature hepatocytes and keep some features of a fetal immature stage, this model has been widely used to investigate *in vitro* different liver features; HLCs provide a valid platform for disease modelling, personalized therapies, and regenerative medicine (Ju et al. 2024; Suleman et al. 2025).

At present, several protocols are available in literature to differentiate iPSCs to 2D hepatocyte-like cells; in the relevance of this thesis work, we primarily concentrated on two of them. The first one was published by Liu and colleagues in 2018 (Liu, Lamprecht, and Duncan 2018), and it was chosen among others because of the deep validation of the protocol shown by performing several assays on the HLCs, and because of the efficiency and reproducibility they state to have achieved. The second one is based on the commercial kit produced by STEMCELL Technologies called *STEMdiff™ Hepatocyte Kit*; to date, this product have been used only on one recently published manuscript (Nirgude et al. 2025), where they investigated the lipid metabolism in differentiated hepatocytes. We decided to focus on this kit because of the reproducibility given by using commercially provided media, even if there are no information about cell polarity and membrane transporters activity.

3.5.3. iPSCs-derived 3D models

To overcome structural and functional 2D culture limits, researchers often turn to three-dimensional culture systems, which includes scaffold-free spheroids and organoids encapsulated in extracellular matrix (ECM). Spheroids are generated by cell aggregation in low-attachment plates, and in this model the high cell-cell contact is important for studying metabolism in high-density contexts; iPSCs-derived organoids, instead, grow surrounded by a stiff matrix or a scaffold, which provides mechanical and biochemical signals promoting polarization (Suominen et al. 2023).

Recent protocols have enabled the generation of iPSCs derived hepatobiliary organoids, able to produce more mature hepatocytes and recapitulate *in vitro* biliary canaliculi or duct structures. These models have proven to be robust and reproducible, where the organoids exhibit critical physiological liver features, including hepatocyte polarization, bile canaliculi formation, bile acid production, albumin secretion, and drug metabolism at levels comparable to primary human hepatocytes. Therefore, hepatic organoids can serve as powerful models for

investigating genetic liver diseases: organoids derived from patients with Alagille syndrome and hereditary cholestasis accurately replicated the pathologies, such as impaired bile duct formation and defective bile transport, providing insight into disease mechanisms (Shinozawa et al. 2021; Guan et al. 2023; P. Li et al. 2024; Sgodda et al. 2025). A schematic representation of the mentioned *in vitro* liver models can be found in Figure 5.

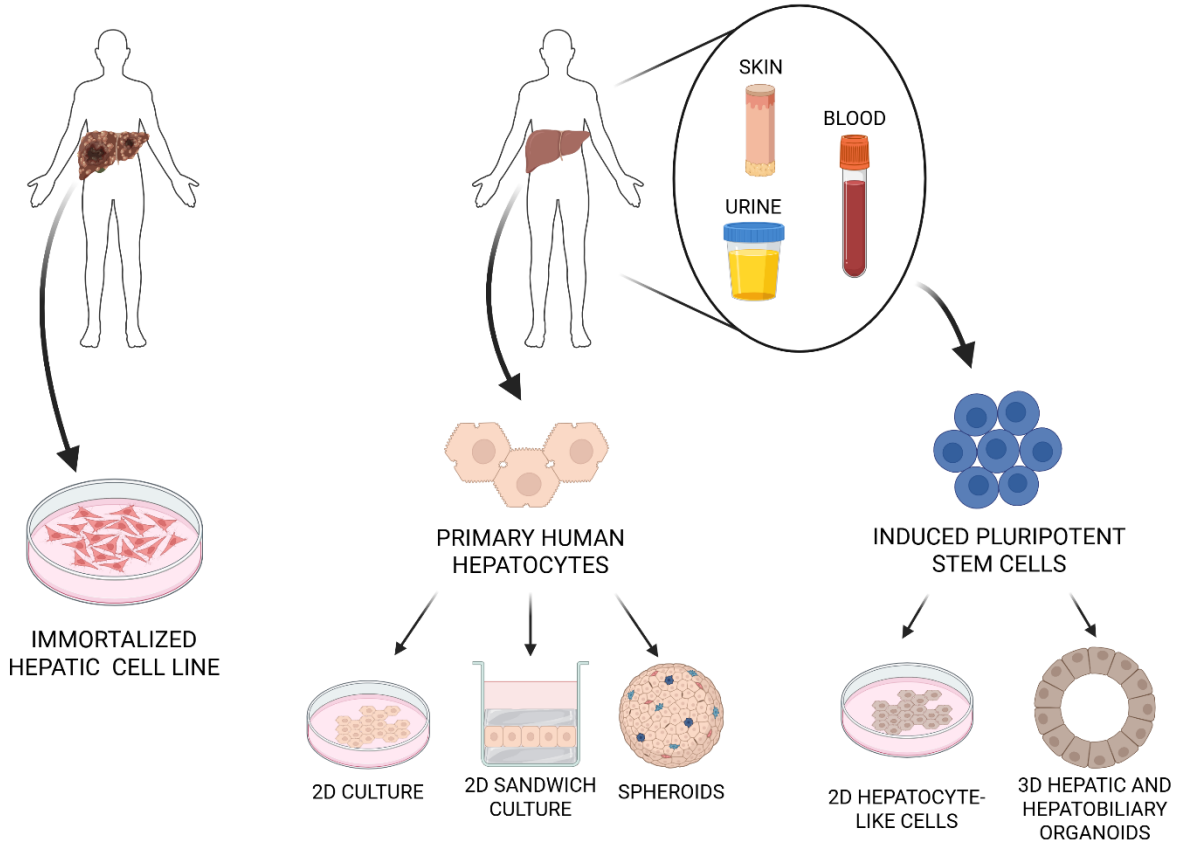

Figure 5: Schematic representation of the main available in vitro hepatic model; created in https://BioRender.com. From cancer isolated cells, hepatic immortalized cell lines have been produced; from healthy or patient liver, primary hepatocyte can be isolated and cultured as a 2D monolayer, as 2D sandwich cultures and as self-assembled spheroids. From different human samples, such as blood, urine and skin, adult cells can be isolated and reprogrammed to induced pluripotent stem cells (iPSCs), which can be then differentiated to 2D hepatocyte-like cells or 3D hepatic or hepatobiliary organoids.

3.6. Patient HC01

The patient named HC01 was enrolled as a part of *HiChol, German Network for Hereditary Intrahepatic Cholestasis*, funded by the German Federal Ministry of Research, Technology and Space. Human material and data were obtained in accordance with the principles of the Declaration of Helsinki, has been approved by the ethics committee of Hannover Medical School (No 2967-2015) and the patient provided written informed consent.

HC01 was first diagnosed with metabolic dysfunction-associated steatotic liver disease (MASLD) (Sgodda et al. 2025), a complex multisystem condition described as the most common cause of chronic liver disease (Targher, Byrne, and Tilg 2024). This patient also suffered from frequent events of intrahepatic cholestasis and developed a cholangiocarcinoma; genetic analysis was performed to discover 3 heterozygous variants in genes associated with PFIC onset, meaning *ABCB4* (NM_018849: c.1769G>A, p.Arg590Gln; rs45575636) encoding for the membrane flippase MDR3; *ABCB11* (NM_003742: c.2628C>G, p.Ile876Met; rs200127070), which translates into BSEP; lastly, *MYO5B* (NM_001080467: c.2122C>T, p.Arg708Trp; rs200856386). While the *ABCB4* variant was reported to be likely pathogenic (Behrendt et al. 2022), the variants on *ABCB11* and *MYO5B* are classified as variants of unknown significance (VUS) on ClinVar database (Sgodda et al. 2025).

Immunofluorescence analysis of healthy and HC01 liver sections was performed to evaluate cell polarization (Figure 6); the uptake transporter OATP1B1 was stained as a basolateral marker, while the tight-junction protein ZO-1 and the bile acid transporters BSEP and MRP2 were used to detect the apical membrane surrounding the bile canaliculi. The liver from the healthy donor showed correct localization of every marker and therefore a correct

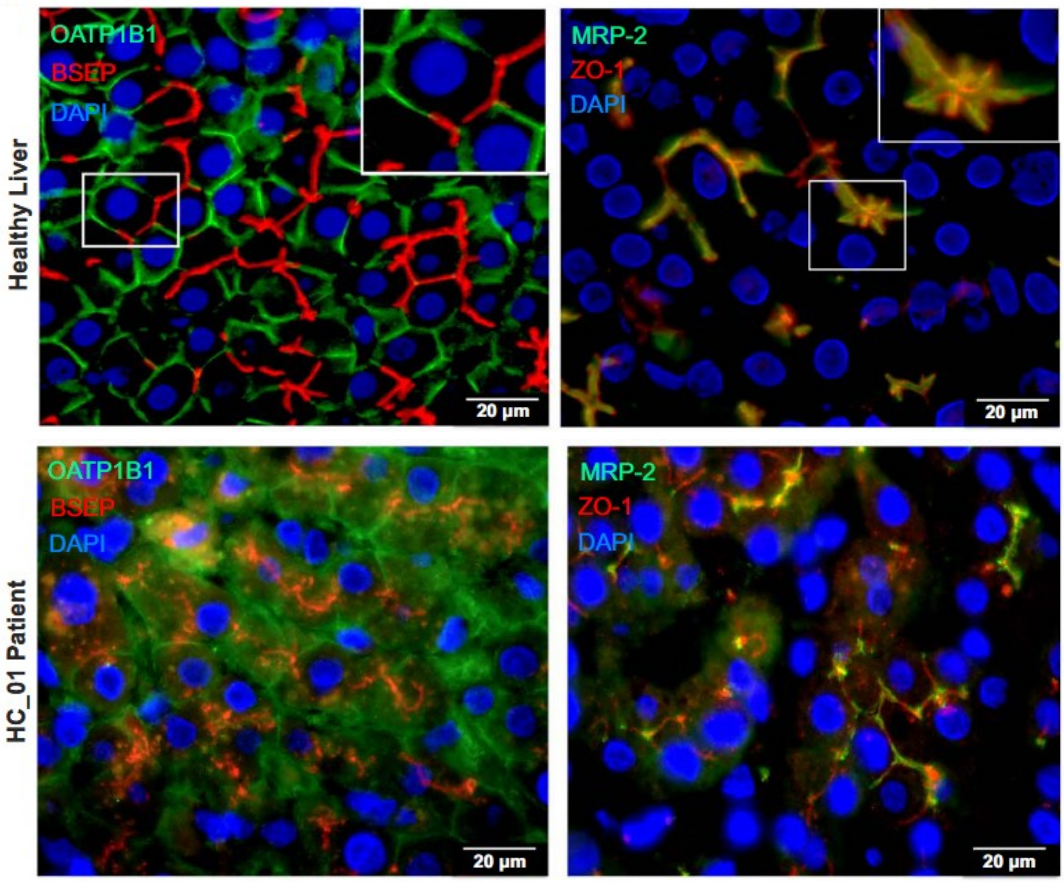

Figure 6: Immunofluorescence staining of healthy liver and HC01 liver, adapted from Sgodda et al., 2025. On the upper line, the healthy liver shows correct localisation of BSEP and MRP2 on the canalicular membrane, and a distinguished localisation of OATP1B1 on the basolateral membrane. On the lower line, HC01 liver displays a diffuse and altered localisation of each protein, with some areas of enriched BSEP and MRP2 on the cell membrane.

hepatocyte polarization. On the contrary, HC01 liver presented an heterogenous phenotype: some areas exhibited distinct basolateral OATP1B1 and apical BSEP expression, however in other adjacent regions both proteins localized to the cytoplasm. Moreover, both membrane and cytoplasmic expression patterns presented areas suggesting a granulated protein localization of BSEP and ZO-1. Similarly, MRP2 expression was predominantly apical, although some regions showed cytoplasmic localization (Sgodda et al. 2025).

Hepatobiliary organoids were generated from HC01 iPSCs; these structures generally exhibited a polarized phenotype with an inner lumen surrounded by ZO-1 and proper MRP2 localization. However, the BSEP transporter did not demonstrate a distinct localization pattern within the organoids, appearing cytoplasmic instead, suggesting dysfunctional intracellular trafficking (Sgodda et al. 2025).

The bile acid secretion of these organoids was confirmed thanks to an assay with bile acid fluorescent analogues, Cholyl-lysyl-fluorescein (CLF) transported by MRP2 and Tauro-nor-THCA-24-DBD (Tauro-DBD) transported by BSEP. Furthermore, the specificity of this assay was demonstrated by inhibiting either MRP2 or BSEP to detect a unique failure of the corresponding molecule transport. HC01 biliary transport assay showed a successful MRP2-mediated CLF transport but a total loss of BSEP-mediated Tauro-DBD transport, indicating a functional deficiency in BSEP function. For comparison, *MYO5B*-deficient control organoids showed a marked reduction in both MRP2-mediated CLF and BSEP-mediated Tauro-DBD transport, consistent with severe disturbed polarization (Sgodda et al. 2025).

To investigate the contribution of the single heterozygous mutation to the defect detected in HC01 organoids, the authors performed gene correction of *ABCB11* and *MYO5B* mutations separately, as well as double gene correction of both variants. CRISPR/Cas9-mediated correction of the mutated *ABCB11* allele alone did not restore BSEP function, indicating that this *ABCB11* variant had only a minor effect on the overall loss of BSEP-mediated transport activity. On the contrary, the correction of the heterozygous *MYO5B* variant resulted in a restoration of the BSEP-mediated Tauro-DBD transport in HC01 organoids to a significant level, and BSEP protein showed predominant apical localization. Lastly, restoring the wild-type sequences in both *MYO5B* and *ABCB11* induced BSEP-mediated Tauro-DBD transport to the same levels of the healthy control, and BSEP expression was fully restricted to the apical membrane domain (Sgodda et al. 2025).

This study concluded that the heterozygous *MYO5B* variant was the main driver of the defective BSEP transport in HC01 organoids, revealing that it increases the susceptibility to disturbed hepatobiliary BSEP-mediated transport in cholestatic patients (Sgodda et al. 2025).

4. AIM OF THE STUDY

Progressive Familial Intrahepatic Cholestasis (PFIC) is a rare genetic disorder caused by mutations in a specific set of genes. While major pathological mechanisms involving bile acid transporter defects are well characterized, the molecular basis of cholestasis in certain PFIC subtypes, such as MYO5B-associated PFIC10, remains incompletely understood. Specifically, the mechanisms by which *MYO5B* mutations disrupt vesicular trafficking and Bile Salt Export Pump (BSEP) localization require further investigation.

Despite the availability of several *in vitro* hepatic models, the development of a simple, non-invasive, and reproducible cellular model specifically for PFIC has only recently become an object of research. Therefore, the main aim of this PhD project was to validate and enhance an *in vitro* hepatic model to investigate MYO5B-associated cholestasis. A valid model must display a polarized arrangement of cells and reproduce bile acid transport mediated by properly localized membrane transporters.

This aim was pursued using Induced Pluripotent Stem Cells (iPSCs) obtained via non-invasive procedures. iPSCs were differentiated into 2D and 3D hepatic lineages to evaluate differences in polarity establishment and biliary transport between healthy and cholestatic cells. Furthermore, liver-specific lipid nanoparticles were utilized to modulate the cholestatic phenotype through the delivery of mRNA.

5. MATERIALS AND METHODS

5.1. Renal epithelial cells isolation from urine

The study and human sample collection was approved by the Friuli Venezia Giulia Regional Ethics Committee (CEUR, Comitato Etico Unico Regionale). The renal epithelial cells were isolated from healthy donor urine samples starting from a published protocol (Zhou et al. 2012) which was further optimized by our group at Burlo Garofolo Hospital, and by Doctor Cristina Bellarosa group at Italian Liver Foundation. Both optimizations were successful; for this thesis work, I will elaborate the protocol developed by our research group, which was enhanced by following a more recent manuscript (Baliña-Sánchez et al. 2023).

A minimum of 100mL of urine was collected in sterile container from each donor; immediately after the collection, the samples were divided into 3 falcon tubes (approximately 35mL per tube) and 15mL of Resuspension Media (DMEM High Glucose, Euroclone, 10% FBS, Euroclone, 100 units/mL Penicillin and 100 µg/mL Streptomycin, Euroclone, 2,5 µg/mL Amphotericin B, Euroclone) was added to each tube, corresponding to approximately 50% of the sample volume. The samples were either processed immediately or kept at 4°C for 24 hours.

At the moment of plating, the falcon tubes containing the diluted samples were centrifuged at 400xg for 10 minutes; the supernatant was decanted and the cell pellets were washed with 10mL of Washing Buffer (PBS w/o Calcium and w/o Magnesium, Euroclone, 100 units/mL Penicillin and 100 µg/mL Streptomycin, Euroclone, 2.5 µg/mL Amphotericin B, Euroclone), combining cells coming from the same sample in a 15mL falcon tube and centrifuging at 300xg, 10 minutes. After washing, the supernatant was aspirated and the cell pellet was resuspended in 1mL of Primary Medium (DMEM High Glucose, Euroclone, Ham's F12 Nutrient Mix, Euroclone, 10% FBS, Euroclone, REGM SingleQuot kit, Lonza, 100 units/mL Penicillin and 100 µg/mL Streptomycin, Euroclone, 2,5 µg/mL Amphotericin B, Euroclone, 10 µM ROCK inhibitor, Y-27632 Tocris Bioscience) and plated on a previously gelatine-coated 24-multiwell plate (EmbryoMax® Gelatin Solution, Millipore); cells were incubated in a humified environment at 37°C, 5% CO_2.

The day after plating, 1 additional mL of Primary Medium was added; then, every 2 days half of media volume was replaced until renal epithelial cells colonies appeared, which was in most cases between Day 5 and Day 10. When colonies started to grow the media was changed completely every 2 days; the cells were then passaged with Trypsin-EDTA 0,25% (Gibco), centrifuged at 200xg, 5 minutes and plated in 1:1 volume ratio of Primary Medium and Proliferation Medium (REGM® Renal Epithelial Cell Growth Medium BulletKit®, Lonza, 100 units/mL Penicillin and 100 µg/mL Streptomycin, Euroclone, 10 µM ROCK inhibitor, Y-27632 Tocris Bioscience). From the first media change onward, only Proliferation Medium without ROCK inhibitor was used.

Renal epithelial cells, also called urinary cells, were therefore expanded and resuspend in FBS (Euroclone) 10% Dimethyl sulfoxide (DMSO, Sigma-Aldrich) at passage 1 to 3 to be stored in liquid nitrogen.

5.2. Epithelial cells reprogramming into iPSCs with integrating method

Renal epithelial cells isolated from urine samples were reprogrammed to Induced Pluripotent Stem Cells (iPSCs) thanks to a collaboration with Dr. Cristina Bellarosa group at the Italian Liver Foundation (Fondazione Italiana Fegato, FIF), Trieste; the reprogramming was performed following Zhou and colleagues protocol published in 2012 (Zhou et al. 2012).

Shortly, the experimental design includes the use of HEK293T cell line for the retrovirus production; the cells were seeded on appropriate support and transfected after 24 hours with lipofection to deliver the packaging vector, the viral envelope protein vector and the plasmid containing the reprogramming factors (OCT4, SOX2, KLF4, c-Myc). 36 and 60 hours post transfection, the HEK293T supernatant containing the virus was collected and filtered. Renal epithelial cells isolated with the protocol optimized by Doctor Bellarosa group were appropriately seeded 24 hours before infection; two cycles of infection were performed 24 hours apart, the first with the 36-hours and the second with the 60-hours viral supernatant.

First iPSCs colonies appeared at around 16-25 days post infection; when colonies were ready, they were manually picked and plated on Vitronectin-coated plates (VTN Recombinant Human Protein, Truncated, Gibco™). Established iPSCs cell lines were cultured in Essential 8™ Medium (Gibco™) and splitted as fragments with 0,5mM EDTA (UltraPure™ EDTA, pH 8.0, Invitrogen™) or as single cells with accutase (StemPro™ Accutase™ Cell Dissociation Reagent, Gibco™).

5.3. PBMCs (CD34 positive) isolation from peripheral blood

CD34 positive (CD34+) cells were isolated from PBMCs collected from fresh blood samples; these procedures were performed at the Translational Hepatology and Stem Cell Biology group guided by prof. Tobias Cantz at the Hannover Medical School, Germany (Sgodda et al. 2025).

Human material and data used in this study was obtained in accordance with the principles of the Declaration of Helsinki, has been approved by the ethics committee of Hannover Medical School (No 2967-2015) and all patients and/or their parents provided written informed consent.

Peripheral blood samples were diluted with PBMC isolation buffer (PBS 2% FBS, 5mM EDTA) and BioColl® separation solution (Bio&SELL GmbH) was added on top – being careful not to mix it with the blood sample – followed by centrifugation at 400xg for 40

minutes; PBMCs appeared as a white interphase ring that can be isolated from the rest of the phases. Then, the isolated cells were treated to lyse red blood cells (Red Blood Cell Lysis Buffer, BioLegend) for 5 minutes, washed twice with PBMC isolation buffer, counted and resuspended. At this time, part of the cells where frozen and part were used to isolate the subpopulation of CD34+ hematopoietic stem cells.

The CD34+ cells isolation was performed with the *CD34 MicroBead Kit* (Miltenyi Biotec) according to manufacturer instructions. This method employs a direct magnetic labelling system. PBMCs were first incubated with a FcR blocking reagent to reduce unspecific binding to the human Fc receptor, then CD34 Beads were added to the sample and incubated at 4°C. After washing, cells were transferred into specific column placed in a magnetic field, leading to the binding of the CD34+ cells enriched beads to the column. Then the magnetic force is released and the CD34+ cells were collected and plated with a density of $1x10^5$ cells/mL in suspension culture plates in CD34+ specific medium (*StemSpan™ SFEM*, STEMCELL Technologies, 2% Penicillin and Streptomicin, 100ng/mL hSCF, Peprotech, 50ng/mL hTPO, Peprotech, 100ng/mL hFlt3, Peprotech).

5.4. PBMCs reprogramming into iPSCs with non-integrating method

CD34+ cells were reprogrammed with *CytoTune™-iPS 2.0 Sendai Reprogramming Kit* (Thermo Fisher Scientific), following manufacturer instructions, at prof. Cantz laboratories at Hannover Medical School.

96 hours post transfection, isolated blood cells were plated on CF1 murine feeder cells in ES-media (39% KnockOut™ DMEM, 39% KnockOut™ DMEM-F12, 19% KnockOut™ Serum Replacement, 1% MEM Non-Essential Amino Acids, 1% Pen/Strep, 1% L-Glutamine, all Thermo Fisher Scientific; FGF2 20ng/ml, ActiveBiosience); after additional 48 hours, media was changed every 2 days until colonies with iPSCs morphology appeared. When passaging, iPSCs were detached with Collagenase Type IV (Thermo Fisher Scientific) and 3mm glass beads (Roth); resulting cells fragments were plated again on CF1 feeder cells (Sgodda et al. 2025).

Before differentiation, blood-derived iPSCs were adapted to feeder-free culturing conditions; cells were seeded on Geltrex-coated supports (Geltrex™ LDEV-Free Reduced Growth Factor Basement Membrane Matrix, Thermo Fisher Scientific) with complete Essential 8™ Medium (Thermo Fisher Scientific) supplemented with ROCK Inhibitor at a density of $3x10^4$ to $6x10^4$ cells/cm^2.

The characterization of pluripotency and genetic aberration was performed by prof. Cantz group at Hannover Medical School following International Society for Stem Cell Research (ISSCR) guidelines; the detailed description of the methods and procedures performed with this purpose is present in the manuscript recently published by prof. Cantz group. Briefly,

expression of pluripotency markers was evaluated with flow cytometry (membrane markers TRA1-60 and SSEA-4), and immunofluorescent staining (nuclear OCT4, NANOG, SOX2); Real-Time qPCR was used to determine pluripotency gene expression (*POU5F1*, *NANOG*, *SOX2*), other than Sendai virus clearance. Moreover, genetic abnormalities were excluded with karyotype analysis (Sgodda et al. 2025).

5.5. RNA isolation and reverse transcription

RNA from samples of interest was isolated with TriFast™ (Euroclone) following manufacturer instructions; shortly, TriFast™ reagent was added to the cells and the lysed suspension was collected in an appropriate tube to add chloroform. After centrifugation, the lysate divides into three phases: the aqueous one, containing RNA, was isolated and isopropanol was added to precipitate RNA. Upon two ethanol washing, the sample were dissolved in RNase-free water and stored at -80°C.

When needed, 1µg of the RNA samples was reverse transcribed with *Transcriptor First Strand cDNA Synthesis Kit* (F. Hoffmann-La Roche Ltd) to generate complementary DNA (cDNA) which was used as template for PCR or Real Time quantitative PCR.

5.6. Polymerase Chain Reaction (PCR)

Polymerase Chain Reaction (PCR) was used throughout the whole project to amplify DNA of interest to either check gene expression or perform DNA sequencing.

Unless specified otherwise, *KAPA HiFi HotStart Ready Mix* (Roche Molecular Systems, Inc.) was used to perform PCR following manufacturer instructions; the list of the primers used for different purposed can be found in Table 2.

Table 2: List of primers used with KAPA HiFi HotStart Ready Mix.

NAME	REFERENCE	FORWARD PRIMER 5'–3'	REVERSE PRIMER 5'–3'	AMPLICON SIZE
MYO5B_1	Self-designed	GGCATGTGTATGAATGGATG	CTTTGACTTCCTTTTGGCCC	530bp
MYO5B_2Fmut	Self-designed	GTTGCCATTAATCCATATGAG	CTTTGACTTCCTTTTGGCCC	430bp
MYO5B_2Fwt	Self-designed	TATGAACAGTTGCCAATCTA	CTTTGACTTCCTTTTGGCCC	430bp
HPRT	(Namipashaki et al. 2023)	AAGAATGTTGTGATAAAA GGTGATGCT	TCAAGGGCATATC CTACAACAA	698bp
Transgene RT	Adapted from (Zhang et al. 2011)	AGAAGAAAGACCAAGACCCT GATGAAGAAG	CTCAACGTTAGCTTCAC CAACAGGAACTATG	721bp

The PCR products were loaded on agarose gel (GellyPhor® LE, Euroclone) to perform nucleic acid separation by electrophoresis.

5.7. CRISPR/Cas9 mediated *MYO5B* gene editing

CRISPR/Cas9 mediated gene editing was performed to insert mutation of interest located on the *MYO5B* gene; we delivered the Cas9 enzyme as a ribonucleoprotein (RNP) applying either lipofection or nucleofection as transfection method. Precise gene modification was achieved through the promotion of homology-directed repair (HDR) by co-delivering a DNA template containing the desired nucleotide substitution alongside the RNP complex.

We designed and tested RNA guides (SgRNA) targeting *Patient 3* homozygous *MYO5B* mutation (c.356A>G; p.Tyr119Cys) published in 2017 (Gonzales et al. 2017). As mentioned, liver biopsies from this patient displayed an altered localisation of the apical bile acid transporter BSEP, but no functional characterization was performed; therefore, we decided to insert this mutation in wild-type donor iPSCs generated with lentiviral reprogramming on urinary cells.

Alt-R™ S.p. Cas9 Nuclease V3 was purchased from Integrated DNA Technologies (IDT) together with the guide RNAs designed with the IDT free online tool (*Custom Alt-R™ CRISPR-Cas9 guide RNA*, https://eu.idtdna.com/site/order/designtool/index/CRISPR_CUSTOM). The SgRNA consists of two elements: a target-specific crRNA which allows the binding to the region of interest, and a green fluorescently labelled (ATTO488) tracrRNA which acts as a scaffold and as a selection driver.

To test the designed guides, we used lipofection with Lipofectamine™ Stem Transfection Reagent (Invitrogen™) following a published protocol, from which we also obtained a SgRNA control guide on *HPRT* gene (Namipashaki et al. 2023). In detail, to assemble the SgRNA the two composing elements were combined with a final concentration of 1µM each, incubated at 95°C for 5 minutes and then the mix was allowed to cool to room temperature. The assembled SgRNA was incubated with the SpCas9 enzyme at room temperature for 5 minutes to form the RNP complex (final elements concentrations 0,3µM); 2µL of Lipofectamine per well were diluted in Opti-MEM™ I Reduced Serum Medium (Gibco™) and incubated with the RNPs for 20 minutes at room temperature. Every transfection was done on $1{,}5x10^5$ iPSCs on vitronectin-coated 24-mw plates. 48 hours after transfection, genomic DNA was isolated with *QuickExtract DNA Extraction Solution* (LGC Biosearch Technologies) and the concentration was quantified with a microvolume DNA spectrophotometer (NanoPhotometer®, IMPLEN).

To assess the editing efficiency of the designed SgRNAs, we performed a T7 Endonuclease I (T7EI) assay, exploiting the *Alt-R™ Genome Editing Detection Kit* (IDT) as a control; the T7EI enzyme recognizes and cleaves DNA where a mismatch is located. Loci were amplified from genomic DNA and PCR product denatured and immediately slowly annealed to form

heteroduplexes. After T7EI digestion, the products were separated by gel electrophoresis and differences in the pattern indicated editing efficiency.

Table 3 contains the guides sequences and the length of the segments resulting after T7EI assay was performed on the PCR product (Primer pair MYO5B_1 and HPRT from Table 2).

Table 3: Single guide RNA sequences and corresponding fragments after T7EI assay.

	SEQUENCE 5'-3'	UNEDITED FRAGMENT	EDITED FRAGMENTS
SgRNA16	TATGAACAGTTGCCAATCTA	530bp	410bp + 120bp
SgRNA20	AAACATGGGAGACATGGACC	530bp	370bp + 160bp
SgRNA21	GGACCCCCACATCTTTGCTG	530bp	320bp + 210bp
SgRNA HPRT	AATTATGGGGATTACTAGGA	698bp	450bp + 248bp

The single strand HDR donor templates (single-stranded oligodeoxynucleotides, ssODN) were designed with the available free online IDT tool (*Alt-R™ HDR Design Tool*, https://eu.idtdna.com/site/order/designtool/index/HDRDESIGN) following the advices from the IDT manual named "*Improved methods for CRISPRCas9 homology-directed repair (HDR) for efficient, high-fidelity genome editing*", which can be downloaded from IDT website upon request.

After selecting the most efficient SgRNA and designed the ssODN, we performed the knock-in experiment by nucleofecting the iPSCs, following a protocol adapted from the available online manual by IDT named "*Homology-directed repair using the Alt-R™ CRISPR-Cas9 System and Alt-R HDR Donor Oligos in iPSCs*". The RNP complex formation is similar to the one mentioned for the guide selection, with differences in the SgRNA concentration (50µM for both tracrRNA and crRNA) and the final complex concentration (gRNA 4,8µM, Cas9 4µM); the donor template was added with a final concentration of 4µM.

The nucleofection was performed with the *4D-Nucleofector® System* by Lonza and the *P3 Primary Cell Nucleofector™ Kit* (Lonza). After 48 hours, the cells were analysed through cytometry (BD FACSMelody™ Cell Sorter, Becton Dickinson) to isolate the ATTO488 positive subpopulation which was sorted as single cells in previously VTN-coated 96-mw plates. The colonies arose from single cells in about 2 to 4 weeks post transfection; to select the positively edited clones, we first performed a PCR with wild-type and mutation-specific primers (MYO5B_2Fmut from Table 2), then we confirmed by Sanger sequencing the edit in the positive clones.

5.8. 2D model and characterization

iPSCs can be differentiated to hepatocyte-like cells through 2D differentiation protocols; there are many different protocols available online, but they all approximately require the same steps: from iPSCs to definitive endoderm (DE), from endoderm to hepatic progenitors (HP) and lastly from hepatic progenitors to hepatocyte-like cells (HLC). As already described, the final cells are not mature hepatocytes, but they can reproduce simple hepatic functions, depending on the different need or field of research.

For this project, we tested 2 different protocols: one was published by Liu and colleagues in 2018 (Liu, Lamprecht, and Duncan 2018), and the second one is based on the commercial kit produced by STEMCELL Technologies called *STEMdiff™ Hepatocyte Kit* (https://www.stemcell.com/products/stemdiff-hepatocyte-kit.html); to date, this product have been used only on one recently published manuscript (Nirgude et al. 2025) where they investigated the lipid metabolism in differentiated hepatocyte. The schematic formulation of every medium of the different protocols is shown in Table 4.

Table 4: 2D differentiation protocol media composition and corresponding day of feeding.

	ENDODERM		**HEPATIC PROGENITORS**		**HEPATOCYTE-LIKE CELLS**
Liu et al, 2018	RPMI-1640 + B27 w/o insulin Activin A BMP4 bFGF	RPMI-1640 + B27 w/o insulin Activin A	RPMI-1640 + B27 BMP4 bFGF	RPMI-1640 + B27 HGF	Hepatocyte Culture Medium (HCM, Lonza) + Oncostatin M
DAY 0: 7x10⁴ cells/cm²	DAY 1-2	DAY 3-5	DAY 6-11	DAY 11-15	DAY 16-20
STEMdiff™ Hepatocyte Kit	STEMdiff™ Endoderm Basal Medium MR/CJ	STEMdiff™ Endoderm Basal Medium CJ	STEMdiff™ Hepatic Progenitor Medium		STEMdiff™ Hepatocyte Medium
DAY 0: 2x10⁵ cells/cm²	DAY 1	DAY 2-4	DAY 5-9		DAY 10-21

iPSCs were seeded on Matrigel-coated (Matrigel® hESC-Qualified Matrix, LDEV-free, Corning®) 24-mw plates with the cell density indicated in the Table 4; media were prepared freshly and changed daily. The hepatocyte-like cells obtained with these protocols were evaluated on hepatic gene expression and hepatic proteins expression and localization.

RNA was extracted from cells at the DE, HP and HLC stages and reverse transcribed as previously described. Gene expression of the markers listed in Table 5 was evaluated by Real-Time Quantitative PCR (RT-qPCR) by Doctor Bellarosa group at FIF according to the *iQ5 SYBR Green Supermix* (Bio Rad) protocol using CFX Connect Real-Time System (Bio Rad);

the primers were designed with the Beacon Designer 8 software (PREMIER Biosoft International). Plus, RNA from Upcyte® Hepatocytes (Upcyte Technologies, CliniSciences Group) was collected and reverse transcribed same as already described and was used as a hepatic positive control.

Table 5: iPSC and hepatic markers used for gene expression evaluation.

	TARGET	FORWARD PRIMER (5' – 3')	REVERSE PRIMER (5' – 3')	ACCESSION
iPSC markers	POU5F1	GACAACAATGAGAACCTTCAG GAGATATGC	CCAAGCTGATTGGCGATGTGA GTGATCTGC	NM_001173531.3
	SOX2	GTGAACCAGCGCATGGACAG CTACGCGC	TCGTAGCGGTGCATCGGTTGC ATCTGTGC	NM_003106.4
Hepatic markers	AFP	AGAACCTGTCACAAGCTGTG	GACAGCAAGCTGAGGATGTC	NM_001134.3
	ALB	CCTTTGGCACAATGAAGTGGG TAACC	CAGCAGTCAGCCATTTCACCA TAGG	NM_000477.7
	ApoF	GGAAGCGATCAAACCTACCA	ATCAGCCTGACAACCAGCTT	NM_001638.4
	HNF4A	CTGCTCGGAGCCACCAAGAGA TCCATG	ATCATCTGCCACGTGATGCTC TGCA	NM_000457.6
	TTR	GCCGTGCATGTGTTCAGAAAG	GACAGCCGTGGTGGAATAGG A	NM_000371.4
	ASGR2	CGTGGGTGACAAGATCACAT	GGGAAGTGCTTCAGATGGAA	NM_001181.4
	SERPINA1	CCGAAGAGGCCAAGAAACAG	GGTCTCTCCCATTTGCCTTT	NM_000295.5
Housekeeping gene	ACTB	CACCTTCTACAATGAGCTGC	CACAGCCTGGATAGCAACG	NM_001101.5

Proteins expression and localization were evaluated with immunofluorescent (IF) staining; we applied the protocol from Matakovic et al. published in 2022 without any major modification (Matakovic et al. 2022). The list of markers, primary and secondary antibodies are attached in the following Table 6.

Table 6: Pluripotency, hepatic and polarization antibodies used in immunofluorescence analysis.

	TARGET	PRIMARY ANTIBODY	DILUTION	SECONDARY ANTIBODY	DILUTION
iPSC Marker	OCT4	Santa Cruz - sc5379	1:300	Alexa Fluor™ 488 goat anti-mouse – Invitrogen	1:2000
Hepatic Markers	HNF4A	Santa Cruz - sc374229	1:200	Alexa Fluor™ 488 goat anti-mouse – Invitrogen	1:2000
	ALB	R&D Systems - MAB1455	1:100	Alexa Fluor™ 488 goat anti-mouse – Invitrogen	1:2000
Hepatic and Polarization Markers	BSEP	Atlas Antibodies - HPA019035	1:500	Alexa Fluor™ 488 goat anti-rabbit – Invitrogen	1:1000
	MRP2	Sigma-Aldrich - M8316	1:100	Alexa Fluor™ 488 goat anti-rabbit – Invitrogen	1:1000
	ZO-1	Invitrogen – 339100	1:100	Alexa Fluor™ 488 goat anti-mouse – Invitrogen	1:2000
	E-cadherin	R&D Systems - AF648	1:100	Alexa Fluor™ 488 donkey anti-goat – Invitrogen	1:1000

For IF staining, on Day 0 cells were seeded on 8-well culture glass slides (Falcon, Corning) with the density indicated in Table 4. At the last day of differentiation, wells were washed with PBS and fixed with 4% PFA for 30 minutes, then washed again and permeabilized with PBS 0,2% Triton X-100 (Merck) at 37°C for 10 minutes. After another washing, non-specific binding sites were blocked with PBS 1% BSA (Merck) at 37°C for 60 minutes and then cells were incubated with primary antibody diluted as indicated in Table 6 in blocking buffer and kept overnight at 4°C. The day after, the cells were washed and incubated with fluorescent secondary antibody diluted in blocking buffer as indicated in Table 6 and placed at 37°C for another 30 minutes. Upon another washing step, *UltraCruz® Aqueous Mounting Medium with DAPI* (Santa Cruz Biotechnology) was applied to seal the coverslip and stain the nuclei. Pictures were acquired thanks to the confocal microscope LSM 990 from ZEISS and ZEISS ZEN 3.9 Microscopy Software.

5.9. 3D organoids generation

The differentiation procedure from iPSCs to organoids was performed following the protocol from prof. Cantz group at Hannover Medical School (Sgodda et al. 2025), which was optimized by the previous work from Shinozawa and colleagues (Shinozawa et al. 2021).

This protocol requires two steps, a first 2D differentiation from iPSCs to foregut endoderm, followed by a 3D differentiation step to spheroid structures. The main advantage of this method is that the cells assembled in the resulting organoids exhibit a polarized arrangement, showing the apical membrane inside towards a canalicular space, and the basal membrane facing outside; therefore, these organoids can reproduce biliary transport.

A schematic representation of the required media is shown in Table 7. In detail, on Day 0 $1.2x10^5$ iPSCs per cm^2 were seeded as single cells on Geltrex coated (1:100) 12-multiwell plate in Essential 8™ Medium (Gibco™) with 10µM ROCK inhibitor. From Day 1, media was changed daily according to the Table 7; at the 7^{th} day the differentiated foregut endoderm cells were detached with accutase and stored in liquid nitrogen in IMDM (Gibco™) 10% DMSO (Sigma).

To generate the 3D organoids, the foregut endoderm cells were seeded into pure Geltrex plus ROCK inhibitor with a density of $1x10^5$ cells/well in a 12mw plate; this creates a stiff matrix shaped as a dome, where the cells are embedded and able to proliferate into three dimensional structures. The medium was changed daily according to Table 7.

At the 12^{th} day the organoids are completely developed and can be isolated from the matrix to perform subsequent assays; the isolation was accomplished with Corning™ Cell Recovery Solution, which was added with firm pressure at the middle of the Geltrex domes and incubated on a plate shaker at 4°C to promote the matrix to dissolve. Every pipette tip and tube were coated with 1% BSA to avoid the organoids binding to the plastic; when the Geltrex was

dissolved, the samples were washed twice with ice-cold PBS and centrifuged at 4°C, 70g for 5 minutes, with slow deceleration.

Table 7: Schematic report of 2D and 3D media used for the generation of hepatobiliary organoids.

<table>
<tr><th colspan="3">2D DIFFERENTIATION</th><th colspan="3">3D ORGANOID GENERATION</th></tr>
<tr><td colspan="2">EIM
Endoderm Induction Media</td><td>FIM
Foregut Induction Media</td><td>HLO
Hepatic Liver Organoid Generation Media</td><td colspan="2">LIS
Liver Specification Media</td><td>LM
Liver Maturation Media</td></tr>
<tr><td>RPMI 1640 +
Activin A
BMP4</td><td>RPMI 1640 +
Activin A
FBS</td><td>Advanced DMEM/F12 +
B27
N2
L-Glutamine
FGF4
CHIR99021</td><td>IMDM/F12 nutrient mix +
B27
N2
L-Glutamine
1-thioglycerol
Ascorbic acid
bFGF
VEGF
EGF
CHIR99021
A83-01</td><td colspan="2">IMDM/F12 nutrient mix +
B27
N2
L-Glutamine
1-thioglycerol
Ascorbic acid
IWP-2
Retinoic acid</td><td rowspan="2">Hepatocyte Culture Medium (HCM) +
HGF
Dexamethason
Oncostatin-M</td></tr>
<tr><td colspan="3"></td><td>PD0325901
LDN</td><td>BMP4
A83-01</td></tr>
<tr><td>DAY 1</td><td>DAY 2-3</td><td>DAY 4-6</td><td>DAY 1-4</td><td>DAY 5</td><td>DAY 6-8</td><td>DAY 9-11</td></tr>
</table>

The organoids originated with this protocol show a spheric morphology with an inner lumen, and present strong mRNA expression of both bile acid transporters (BSEP and MRP2), other than MYO5B and some hepatic markers such as ALB, HNF4α and TTR, indicating the affinity with the hepatic phenotype. The organoid characterization was not part of this thesis work, since it was already recently demonstrated by prof. Cantz group (Sgodda et al. 2025).

5.10. Biliary transport assay

The hepatobiliary transport assay was performed using fluorescent bile acid analogues that are transported from the outside to the inner lumen of the organoids; this assay allows a qualitative and semi-quantitative evaluation of the efficiency of the biliary transport of these 3D structures. The protocol for this assay was optimized by professor Cantz group at Hannover Medical School, which validated and demonstrated the specificity of BSEP and MRP2 transport also with transport inhibitors (Sgodda et al. 2025).

In detail, the organoids at Day 12 of differentiation were isolated as described in the previous chapter; after washing the samples twice in ice-cold PBS, the pelleted organoids were collected in a 1,5mL BSA-coated tube and resuspended in HCM media (Lonza) supplemented with ROCK-inhibitor and two fluorescent bile acid analogues: Cholyl-L-Lysine Fluorescein disodium salt (CLF, Avanti Research™) which is transported by MRP2 and exhibits a green fluorescence, and Tauro-nor-THCA-24DBD (Tauro-DBD, GenoMembrane), transported by

BSEP and emitting a red fluorescent signal. The incubation was carried out at 37°C at different time points (0 min, 5 min, 10 min, 20 min, 30 min, 45 min, 60 min, 90 min); after each incubation, the samples were washed 3 times with ice-cold PBS to stop the transport. Then, the organoids were plated with warm HCM media to perform imaging analysis with an inverted fluorescence microscope (Olympus IX70) and CellSens Software. At least 30-50 single organoids were analysed for every time point, capturing a minimum of 7 pictures in the brightfield, green and red channel.

Post-acquisition analysis and semi-quantitative evaluation of organoids transport were performed with ImageJ (Schneider, Rasband, and Eliceiri 2012); first, the area of the organoids was manually marked and automatically measured from the brightfield picture, then for each fluorophore channel a signal intensity threshold was set and maintained throughout the analysis of the whole experiment. Positive organoids areas were summed up and the ratio with the corresponding total area was calculated and converted to a percentage value (Sgodda et al. 2025).

5.11. Organoids staining

Organoids at Day 12 of differentiation were harvested and collected same as described for the hepatobiliary transport assay. After washing, the samples were fixed in 4% PFA (either 1 hour at room temperature or overnight at 4°C) and embedded in 1,5% agarose drops to facilitate the handling. Then, the agarose drops were transferred to 40µm nylon mesh and closed into tissue cassettes to be dehydrated and paraffin embedded with an automated tissue processor (Leica) and an embedding centre (Shandon HistoCentre 2). After paraffin embedding, 2µm sections were cut with a microtome (HistoCore MULTICUT, Leica) and arranged on glass slides; slides were then deparaffinized manually (20min xylol 2 times, 8min 100% ethanol 2 times, 8min 75% ethanol, 8min 50% ethanol, 8min deionised water 2 times) and unmasked in a dedicated buffer (10mM Tris, 1mM EDTA, 0.05% Tween-20, pH:9) at 96°C for 45 minutes to gain antigen retrieval.

Table 8: Primary and secondary antibodies used for organoids staining.

TARGET	PRIMARY ANTIBODY	DILUTION	SECONDARY ANTIBODY	DILUTION
BSEP	(Noé, Stieger, and Meier 2002; Ellinger et al. 2017)	1:100	Alexa Fluor™ 488 donkey anti-rabbit – Invitrogen	1:400
MRP2	(JEDLITSCHKY et al. 1997)	1:100	Alexa Fluor™ 488 donkey anti-rabbit – Invitrogen	1:400
ZO-1	Invitrogen - 339100	1:100	Alexa Fluor™ 594 donkey anti-mouse – Invitrogen	1:400
OATP1B1	(König et al. 2000)	1:100	Alexa Fluor™ 488 donkey anti-rabbit – Invitrogen	1:400

Samples slides were blocked in PBS 1% BSA for 1 hour at room temperature, then washed with PBS and incubated at 4°C overnight with primary antibodies diluted in PBS 0.1% BSA. After another washing, samples were incubated with secondary antibodies at room temperature for 1 hour and then stained with DAPI (500ng/ml, Sigma); lastly, coverslip were placed with mounting medium (Agilent) and pictures were taken with an inverted fluorescence microscope (Olympus IX70) and analysed with CellSens software. Primary and secondary antibodies are listed in Table 8.

5.12. Membrane protein flow cytometry analysis

Flow cytometry analysis was exploited to verify endoderm marker expression on urine- and blood-derived cells. $2x10^5$ cells were centrifuged at 300xg for 5 minutes and incubated with Allophycocyanin (APC) labelled anti-CXCR4 antibody (Invitrogen) and Phycoerythrin (PE) labelled anti-CD117 antibody (Invitrogen) in FACS buffer (PBS, 2% FBS, 2mM EDTA) for 30 minutes at 4°C. At the end of antibody incubation, cells were washed with PBS and analysed with CytoFlexS cytometer (BeckmanCoulter) and CytExpert software; unstained cells of the same origin were used as autofluorescence control.

5.13. Site directed mutagenesis and HiFi cloning

The plasmid containing *MYO5B* full-length ORF sequence (NM_001080467.3) was purchased from OriGene Technologies; the plasmid (Figure 7) includes two tag sequences downstream of the *MYO5B* sequence – a MYC-tag and a FLAG/DDK-tag – and a Kanamycin resistance gene to perform selection during bacteria transformation.

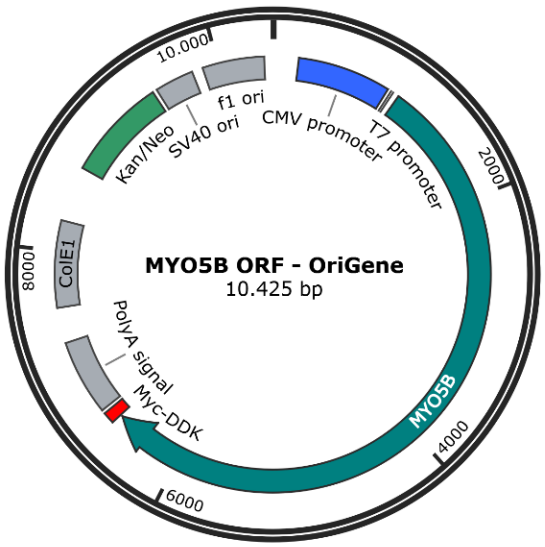

Figure 7: MYO5B Origene plasmid map created with SnapGene.

The *MYO5B* ORF sequence presents two restriction enzyme sites recognised by the enzyme BspQI that we had to delete for experimental purposes. To achieve this deletion, we performed site-directed mutagenesis (SDM) using *Q5® Site-Directed Mutagenesis Kit* by New England Biolabs (NEB); this kit allows for a rapid site-specific modification on double-stranded plasmid DNA. The two BspQI restriction sites must be deleted one at the time, performing two different SDM experiments in a row; after that, with the same experimental procedure we deleted Exon 30 from the *MYO5B* sequence as well.

First, a primer pair set is designed for each edit and for Exon30 deletion (M5B BspQI_1, M5B BspQI_2 and M5B Ex30 DEL from Table 9); in the single nucleotide mutagenesis set of primers, one of the primers carries the mutation of interest and the two sequences do not overlap each other, while in the deletion primer set the 5' ends of both sequences were designed in order to flank Exon 30 sequence. The amplification was performed thanks to a high-fidelity DNA polymerase (*Phusion™ High-Fidelity DNA Polymerase* by Thermo Fisher Scientific), during which either the mutation is inserted in the plasmid sequence or the exon sequence is deleted.

Table 9: Primers designed for site-directed mutagenesis to delete BspQI restriction site and Exon30, and HiFi cloning in the IVT Backbone.

NAME	FORWARD PRIMER (5' – 3')	REVERSE PRIMER (5' – 3')
M5B BspQI_1	GTATGAGGAGCAGATCAATATCC	ACCGTGTCTCTGTTTTTCTCC
M5B BspQI_2	CAGCTGTTCTACATGATCAAC	TTTGAATACCTGCAGGATGATC
M5B Ex30 DEL	GCTGCTGGAGGCTCAGCTG	CTGTTTGTCTGGCAGACCCC
HiFi MYO5B-IVT BB	AGAACCCGCCACCATGTCGGTGGGCGA	AGTACCAGCTCGAGTCATTAAACCTTATCGTCG

After PCR, in a single reaction including a kinase-ligase-DpnI (KLD) enzyme mix, the amplified material is circularized and the original unedited template is removed; the plasmid is now ready to be transformed into competent bacteria. To accomplish a highly efficient transformation we used NEB® Stable Competent *E. coli*, following manufacturer protocol; after transformation, the bacteria were plated on kanamycin enriched LB-agar plates to allow selection of the positively transformed cells.

The day after, colonies were manually picked and let grown overnight into LB media supplemented with kanamycin. Then, plasmid DNA was extracted with *QIAprep Spin Miniprep Kit* from QIAGEN following manufacturer instructions, and a control BspQI (NEB) digestion was performed to check if the restriction site has been erased. The correctly edited clones were then selected and the second round of SDM was performed; after the second BspQI restriction site was edited, we proceeded with deleting Exon 30. To verify Exon 30 deletion, we digested with XhoI restriction enzyme (NEB), which lead to a different digestion pattern whether Exon 30 is included or not.

After SDM, the *MYO5B* ORF sequence was cloned into an *in vitro* transcription-specific backbone vector, specifically a vector named pHO67-pT7-AG-UTR from BioNTech in

cooperation with Cell and Gene Therapy group at Hannover Medical School guided by professor Michael Ott, who kindly donated it to us; for simplicity's sake, it will be referred to as IVT backbone or IVT BB. This plasmid contains all the regulatory regions required for the following *in vitro* transcription and the stability of the resulting mRNA, such as the T7 promoter followed by the AG transcription initiator, the 5'UTR and 3'UTR, and the PolyA tail; moreover, a BspQI restriction enzyme site is located at the end of the PolyA tail to linearize it (Figure 8).

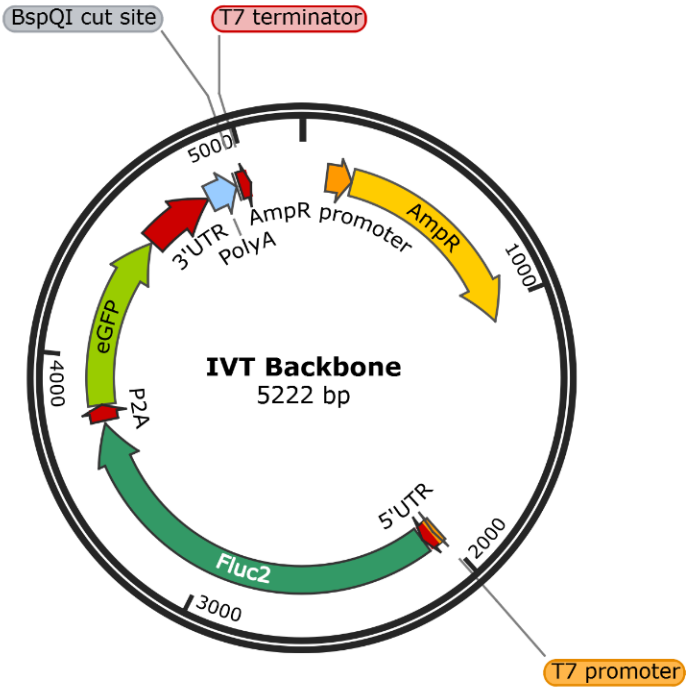

Figure 8: In vitro transcription (IVT) backbone plasmid map created with SnapGene.

The cloning was performed with *NEBuilder® HiFi DNA Assembly Cloning Kit* by NEB; this cloning is based on the Gibson Assembly, which combines three enzymatic activities in a single-tube reaction: a 5' exonuclease, which trims the 5' ends of the DNA fragments allowing the complementary sequences to anneal, a DNA polymerase, which synthesized the missing gaps, and a DNA ligase, that joins the DNA fragments together leading to a circular plasmid.

Before the cloning process, we designed a set of HiFi primers to include backbone-overlapping sequences upstream and downstream the *MYO5B* sequence (HiFi MYO5B-IVT BB from Table 9); PCR was performed with *Phusion™ High-Fidelity DNA Polymerases* by Thermo Fisher Scientific and the PCR product was loaded on an agarose gel. The correct band was cut from the gel under UV light with a clean scalpel and the DNA was extracted with the *Monarch® DNA Gel Extraction Kit* from NEB.

Then, the IVT backbone was digested with two restriction enzymes (XhoI and NcoI, NEB) to separate the region of interest from the plasmid; the DNA was then isolated from agarose gel as mentioned before. HiFi cloning was performed as already described, choosing a molar ratio of 2:1 of the insert (*MYO5B* sequence) to the IVT backbone; the resulting plasmid was

transformed into NEB® Stable Competent *E. coli* and plated on ampicillin LB-agar plates. The next day, colonies were manually picked and amplified overnight in LB medium; plasmid DNA was extracted with *QIAprep Spin Miniprep Kit* by QIAGEN and a control digestion was performed to evaluate the success of the cloning procedure. The full plasmid from one positive clone was sequenced through an external facility (Microsynth AG) to be selected and proceed to the *in vitro* transcription.

5.14. *In vitro* transcription and lipid nanoparticles (LNPs) production

The *in vitro* transcription was performed with *HiScribe® T7 mRNA Kit with CleanCap® Reagent AG* from NEB; this kit allows the production of high amount of mRNA (up to 90µg RNA from 1µg of plasmid) including the Cap-1 structure, which helps the stability of the mRNA and protects from the cell degradation, leading to a higher translation efficiency. A modified version of UTP, specifically 5-Methyl-UTP (m5UTP, Jena Bioscience GmbH), was used in the reagent mix to increase stability and decrease immunogenicity.

The plasmid resulting from the former SDM and cloning procedures was linearized with BspQI digestion and purified with *QIAquick PCR Purification Kit* (QIAGEN) following manufacturer instructions; then 1µg of DNA was mixed with all the supplied IVT reagents and enzymes to produce mRNA. After that, a DNase treatment was completed and the RNA was purified with *Monarch® Spin RNA Cleanup Kit* (NEB) and quantified. To check if the procedure succeeded and the mRNA is intact, we loaded 250ng and 500ng on an agarose gel after denaturation according to the *ssRNA Ladder* (NEB) and *RNA Loading Dye* (NEB) protocol.

The lipid liver mix and the LNP production protocol were optimized by Dr. Sebastian Hook from prof. Michael Ott group at Hannover Medical School, who kindly shared it with us.

The liver-specific lipid mix was composed of C12-200 (C12, Corden Pharma Switzerland), 1,2-dioleoyl-sn-glycero-3phosphoethanolamine (DOPE, Avanti), Cholesterol (Chol, Sigma Aldrich) and 1,2-Dimyristoyl-rac-glycero-3-methoxypolyethylenglycol-2000 (DMG-PEG, Avanti) dissolved in 99.9% ethanol to a final concentration of 12.5 mM solution (molar ratio 35:16:46:2.5/C12:DOPE:Chol:DMG-PEG) (Hook 2023).

The LNP production involves different steps: the *in vitro* transcribed mRNA is encapsulated in the nanoparticles, then these goes through a dialysis process overnight to purify the solution, and the next day the LNPs are concentrated and aliquoted to be stored at -80°C. After the whole production procedure, the encapsulated RNA was quantified with a specific assay.

To start, the mRNA of interest was diluted in 10mM citrate buffer, pH4, and the desired amount was loaded on a syringe, as well as the liver-specific lipid mix; the syringes were applied to the *NanoAssemblr™ Ignite™* nanoparticle formulation system (Cytiva), which

exploits a microfluidic approach to mix the solutions into the small channels of a *Ignite™ NxGen™* single-use cartridge (Cytiva), where the interaction between the lipid mix and the mRNA leads to the nanoparticle self-assembly. The so-formed mRNA-LNP were diluted with PBS and loaded on a dialysis cassette (Slide-A-Lyzer™ G3 Dialysis Cassettes, 20K MWCO, Thermo Fisher Scientific™) and left overnight in 5L of PBS at 4°C with gentle spinning to remove residual citrate and ethanol.

The next day, LNP solution was collected from the cassette and transferred to a filter centrifuge tube (Amicon® Ultra-4 10K Centrifugal Filter, Merck Millipore Ltd) and centrifuged at 2000xg at 12°C for approximately 20-40 minutes to concentrate the solution. When the desired LNP mix volume was reached (500-800 µL), sucrose to a final concentration of 5% was added to help freeze-thaw cycles, and lastly the solution was filtered, aliquoted and shock-froze in liquid nitrogen; the aliquots were then stored at -80°C.

One aliquot was used to measure the LNP-encapsulated mRNA with *Quant-iT™ RiboGreen™ RNA Kit* (Invitrogen), following manufacturer instructions. Shortly, the kit involves a ribosomal RNA standard curve and two buffers, one of which dissolves the lipid nanoparticles; the samples are diluted into both buffers, as wells as the standard RNA at different concentrations, then the fluorescent dye binding nucleic acids is added and fluorescence is measured at 528nm. Thanks to the standard curve built with the given RNA we were able to interpolate the samples concentration and distinguish between the free and the encapsulated RNA.

5.15. LNPs Huh7 transfection

Once *MYO5B*-mRNA LNPs were produced, we tested them on Huh7 line to confirm the release of the mRNA in hepatic cell lines based on the FLAG-Tag. Huh7 were cultured in DMEM High Glucose GlutaMAX™ Supplemented (Gibco™), 10% FBS (Gibco™), Penicillin 100 units/mL and Streptomycin 100 µg/mL (Gibco™), MEM Non-Essential Amino Acids Solution (Gibco™).

The day before transfection, Huh7 cells were seeded with a density of $4x10^4$ cells/cm^2 in a 12mw plate; the day of transfection, the cells were fed with 1mL of media per well supplemented with increasing amounts of LNPs (5 ng, 10 ng, 25 ng, 50 ng, 75 ng, 100 ng, 150 ng), both full-length and Exon 30 depleted isoforms. After 24 hours, the cells were harvested with trypsin (TrypLE™ Select Enzyme, Gibco™) and treated for intracellular staining of FLAG tag; cells were first blocked in 4% PFA for 10 minutes at room temperature, then washed with PBS and incubated with a permeabilization buffer (PBS, 0.4% Tween20, Sigma, 0.1% Igepal, Sigma) for 15 minutes at room temperature. Upon washing in PBS, the samples were incubated at 4°C for 30 minutes with a FITC-conjugated anti-FLAG antibody (DYKDDDDK Antibody, REAfinity™, Miltenyi Biotec) diluted in FACS buffer (PBS, 2% FBS, 2mM

EDTA). Cells were washed again in PBS and analysed with CytoFlexS cytometer (BeckmanCoulter) and CytExpert software to detect FITC-positive Huh7 population; the mRNA release was evaluated through the MFI (Mean Fluorescence Intensity) shift of the LNP treated samples compared to the untreated negative control.

5.16. LNPs organoids transfection

To attempt a functional recovery of biliary transport we transfected HC01 organoids to induce a wild-type *MYO5B* mRNA overexpression.

At Day 11 of the organoid generation, Geltrex domes were dissolved same as described for the hepatobiliary transport assay; once the organoids were washed and isolated, they were incubated in HCM media (Lonza) supplemented with 200ng or 500ng of *MYO5B*-LNPs and Apolipoprotein E (ApoE), which mediates the LNP endocytosis through LDL-receptor, highly expressed on hepatocytes cell membrane (Hook 2023). After 90 minutes at 37°C with gentle shaking, the samples were washed with PBS and encapsulated again in pure Geltrex domes and fed with LM media for additional 12, 24 or 36 hours; the organoids isolation and biliary transport assay were performed as already described.

6. RESULTS

6.1. Urine-derived iPSCs

Renal epithelial cells were isolated from donor urine samples following already published protocols which were further optimized; the sample were collected from 10 healthy subjects, age 22 to 50 years old, both male and female (male=2, female=8). We performed a total of 21 cell isolation from the cohort of 10 donors, including 14 without any optimization and 7 optimized as described in the methods section; out of the 7 optimized samples, 3 were stored at 4°C for 24 hours to simulate the possible shipment of the urine from the patient to our laboratories.

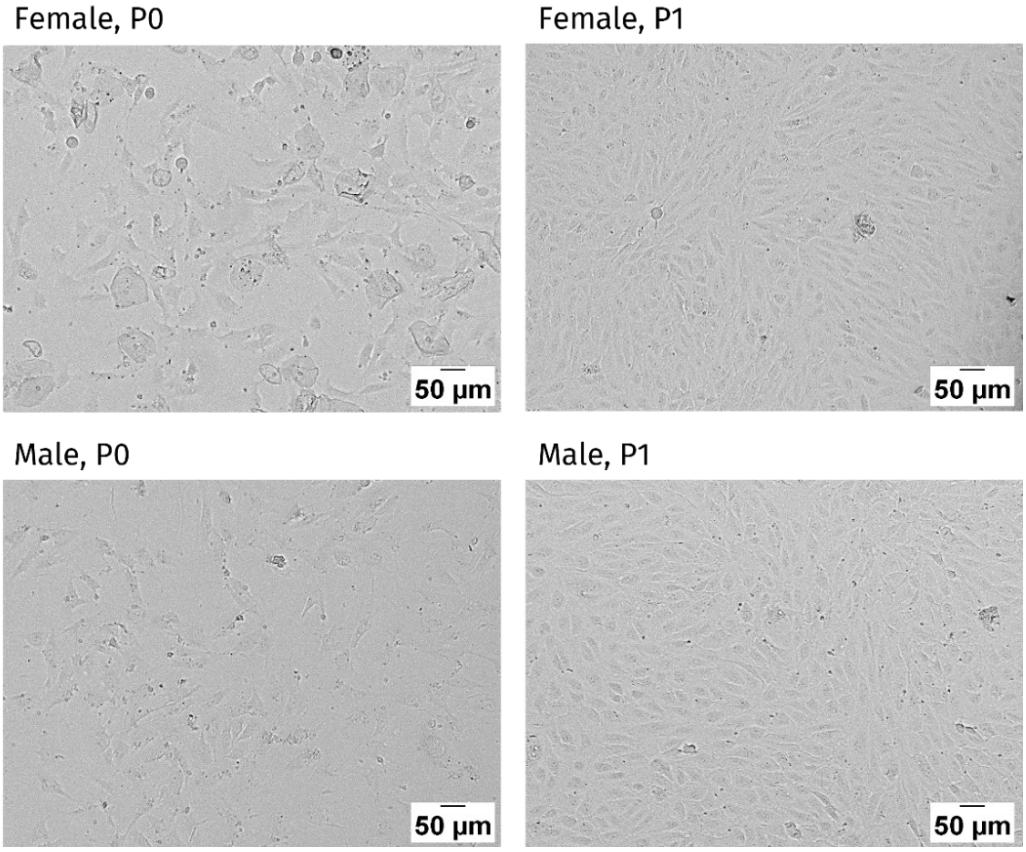

Figure 9: Pictures of isolated renal epithelial cells at P0 on the left and P1 on the right, from female donor on the upper line and male donor on the lower line. P0 samples are still contaminated by other cell types and urine sediments, while P1 samples appear as a unique cell line with an epithelial-like morphology.

From the first day after seeding (Passage 0, P0), the wells showed different cell types and other sediments, especially in the female samples were squamous and blood cells were more evident (Figure 9, Female and Male P0); these undesired urine constituents did not attach to the support and were eventually lost with the multiple media replacements. The epithelial cells were easily recognizable because they arose as compact colonies, 1 to 3 colonies per well, and

exhibited a steady proliferation rate; the first passaging step was performed when the colonies stopped proliferating uniformly, which occurred 2 to 5 days after colonies arose. We passaged the cells with a 1:1 or 1:2 split ratio depending on the number of colonies per well, obtaining a unique cell line which grew uniformly on the well surface as a thin monolayer which compacted after additional 2-3 days (Figure 9, Female and Male Passage 1, P1); no significant difference between the samples of different origin was detected at this step, and cells were stored in liquid nitrogen at P1 or following expansion at P2 or P3.

The percentages of successful and unsuccessful cell isolation are shown in Figure 10; for a total of 21 sample processing, we were able to increase the efficiency by improving the protocol and reach 100% isolation efficiency, meaning that this procedure can be implemented as a solid method to isolate and expand renal epithelial cells from urine samples. Moreover, the optimization proved to be efficient also when the samples were stored temporarily at 4°C, suggesting that a shipment of the samples to the laboratory designed for the isolation is possible.

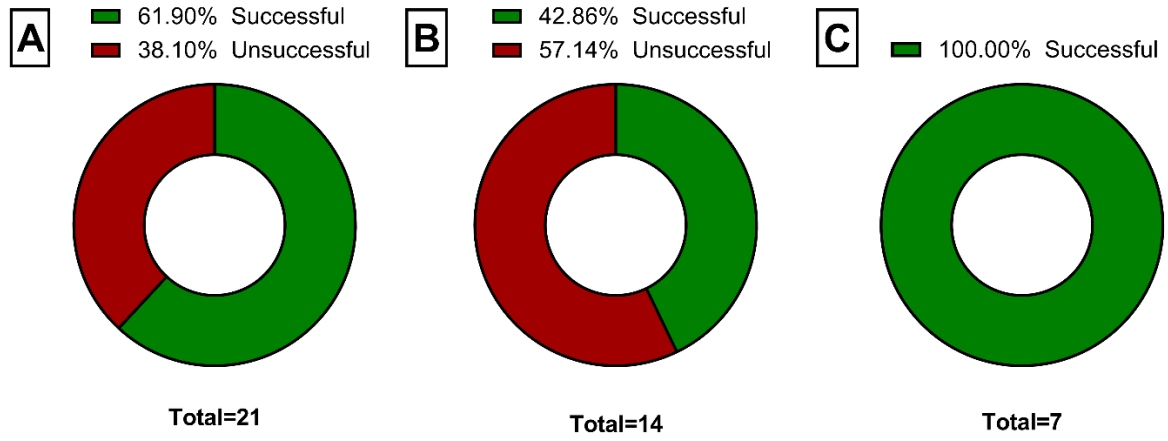

Figure 10: Percentage of successful and unsuccessful renal epithelial cells isolation from urine samples. (A): total samples, before and after protocol optimization; (B): samples before optimization; (C): samples after optimization.

The colonies from different isolation, including samples from the same donor, arose at different time points, with no evident correlation with any considered parameter (age or gender of the donor, protocol optimization, storage). Cell colonies started to be visible from Day 5 to Day 13, with higher number of samples at Day 9 (n=2) and Day 10 (n=3) and only one sample with a delayed colonies onset at Day 19. The data on colonies onset of the set of 21 samples we processed are summarized in Figure 11.

The results are consistent with already published data about renal epithelial cell isolation from urine, where some authors described the onset of the colonies around Day 2 to 5 (Zhou et al. 2012; Tayhan et al. 2017) and some others around Day 5 to 15 (Baliña-Sánchez et al. 2023; Culenova et al. 2021).

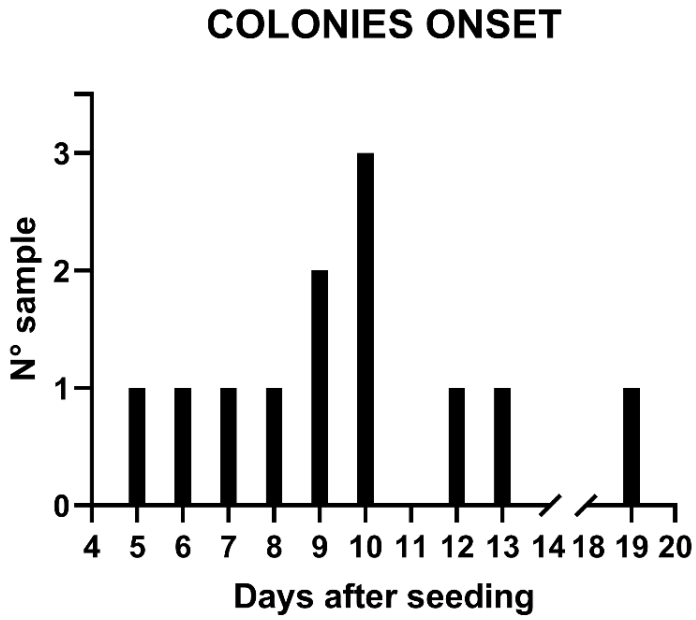

Figure 11: Cell colonies onset related to the day after seeding; on x axis the days after seeding, starting from Day 4 to Day 19, on y axis the number of samples where at least one renal epithelial colony appeared on that day.

Doctor Cristina Bellarosa group at the Italian Liver Foundation, Trieste, performed some alternative optimization starting from the same protocol we employed (Zhou et al. 2012), gaining comparable results. After isolation and expansion of renal epithelial cells, doctor Bellarosa group proceeded to reprogram them with lentiviral integrated method following the protocol from Zhou and colleagues (Zhou et al. 2012), and as a part of the collaboration between the research groups they shared with us the Induced Pluripotent Stem Cells they generated.

6.2. *MYO5B* Gene editing

CRISPR/Cas9 mediated gene editing was performed on urine-derived iPSCs to insert a missense homozygous *MYO5B* mutation which was published by Gonzales and colleagues in 2017 without performing functional assays (Gonzales et al. 2017). Among the available SgRNA designing tool, we selected the IDT online tool to help designing three guides named SgRNA16, SgRNA20 and SgRNA21; plus, we selected from literature a guide sequence on *HPRT* gene to use as a transfection and editing positive control (Namipashaki et al. 2023). We transfected through lipofection the iPSCs with the RNP complexes and collected the DNA after 48h as described in the method section.

The genomic region where the Cas9-mediated editing occurred was amplified (Primer pair MYO5B_1 for SgRNA20, SgRNA16 and SgRNA21, Table 2; primer pair HPRT for *HPRT* gene, Table 2) and then we tested the editing efficiency with the T7 Endonuclease I assay. The

PCR products were denatured and slowly re-annealed with a gradient decrease of temperature to allow the formation of heteroduplexes; next, DNA was digested by T7EI and loaded on an agarose gel. On the gel, the upper band corresponds to the undigested portion of the sample, while the two lower bands correspond to the fragments resulting from the enzyme digestion of the amplified region; by comparing the intensity of the digested to the undigested fragments we can qualitatively determine which guide led to the highest editing efficiency.

Figure 12 shows the results of the T7EI assay of *MYO5B* guides, *HPRT* guide, and the negative and positive controls from the *Alt-R Genome Editing Detection Kit*.

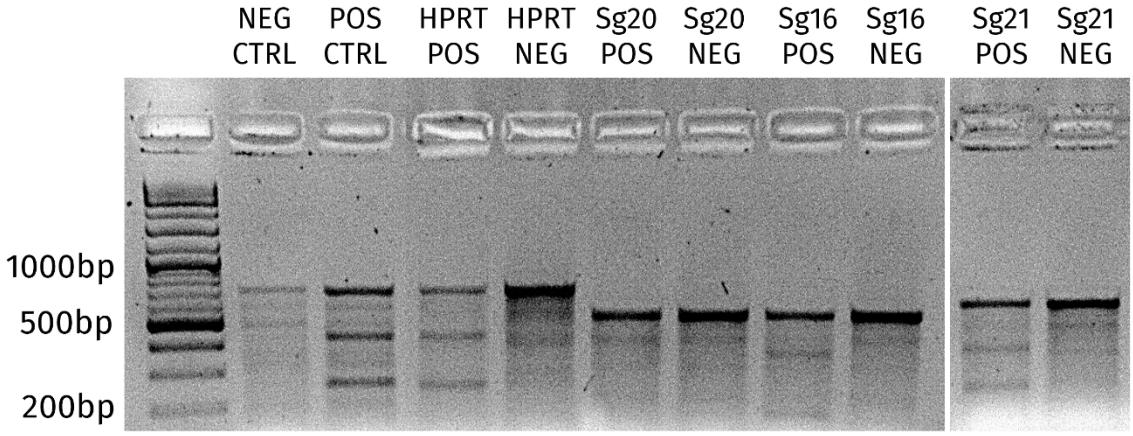

Figure 12: Results of the T7EI assay to test the editing efficiency of the SgRNA designed for MYO5B c.A356G. Quick-Load® 1 kb Plus DNA Ladder from NEB was used as molecular weight marker. For every sample, the negative lane (NEG) represents unedited DNA while positive lane (POS) represents edited DNA, where the upper amplicon is the unedited portion and the 2 lower amplicons are the edited portions. From the right: NEG CTRL (670bp) and POS CTRL (670bp + 442bp and 268bp) from Alt-R Genome Editing Detection Kit by IDT; HPRT POS (698bp + 450bp and 248bp) and NEG (698bp) as transfection and editing control; Sg20 POS (530bp + 370bp and 160bp) and NEG (530bp); Sg16 POS (530bp + 410bp and 120bp) and NEG (530bp); Sg21 POS (530bp + 320bp and 210bp) and NEG (530bp).

The assay showed a successful editing of *HPRT*, suggesting that the RNP complex assembly and transfection procedures worked; the correct fragments from the control kit were detected, indicating that the T7EI assay was valid. The guide with the highest editing efficiency appeared to be SgRNA16, where the differences between the positive and negative control are more visible; thus, SgRNA16 was selected to proceed with the knock-in experiment.

The ssODN was designed following IDT suggestion from the company manual: in the region of our interest, the mutation is PAM-distal and it's outside the optimal distance range from the cut site, thus the non-targeting strand was preferred; the homology arms were designed as symmetric (39bp each side), and we inserted two silent mutation (T>A and A>G) to prevent recutting of Cas9 enzyme: the first on the PAM sequence and the second on the guide sequence. Moreover, the first silent mutation allows for the insertion of a NdeI (NEB) restriction site which can be utilized to check editing efficiency, while both can be exploited for an edit-specific amplification (Primer MYO5B_2Fmut from Table 2).

Figure 13 shows the portion of the *MYO5B* gene sequence that include the edit of interest with the ssODN we designed and the corresponding features.

Figure 13: Portion of MYO5B gene sequence, adapted from SnapGene Viewer. In bright pink, the mutation of interest (c.A356G;p.Y119C); highlighted in blue, the DNA corresponding to the ssODN; in light blue, the SgRNA16 and the PAM sequence (NGG) highlighted in green; marked with a vertical blue bar, the cut site; in purple, the primer specific for the edited DNA (here named 2Fmut); in orange, the two silent mutations, one of which (T>A) allows the insertion of a restriction enzyme site (NdeI).

The knock-in testing was performed with RNPs and nucleofection as described in the dedicated method section. The knock-in efficiency was evaluated with the edit-specific PCR (Primer MYO5B_2Fmut, Table 2, 430bp amplicon) and with NdeI digestion of the PCR products of the sequence of interest (Primer pair MYO5B_1, Table 2), which results in 3 fragments: 530bp for the unedited portion, 415bp plus 115bp for the edited part. Alongside, we performed the T7EI assay to confirm the editing efficiency of the selected SgRNA. The results of these tests are presented in Figure 14.

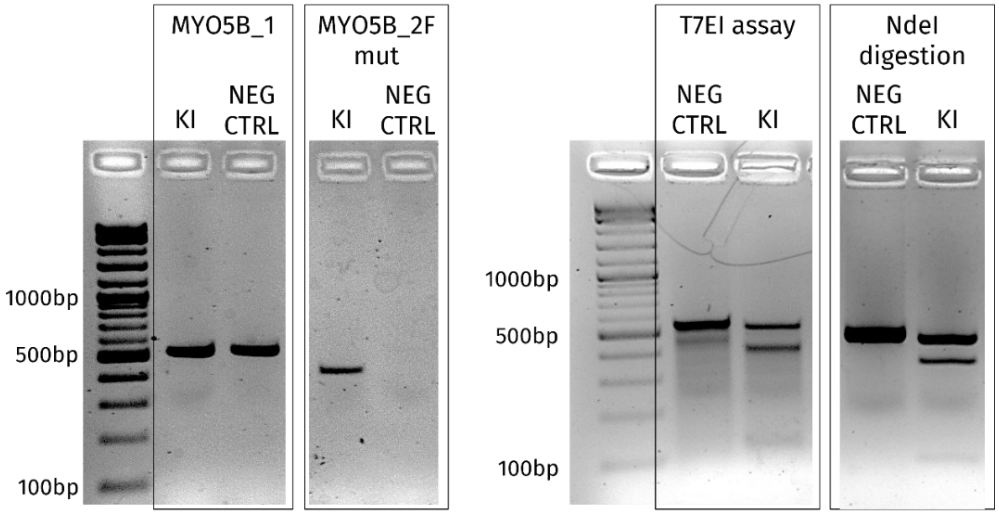

Figure 14: Results of the editing efficiency and knock-in efficiency testing; Quick-Load® 1 kb Plus DNA Ladder from NEB was used as molecular weight marker. KI represents the edited sample; NEG CTRL indicates DNA extracted from non-edited cells. From left to right: PCR amplification of the region of interest (Primer pair MYO5B_1); edit-specific amplification (Primer pair MYO5B_2Fmut); T7EI assay; NdeI digestion.

The editing efficiency of the selected guide was confirmed by the T7EI assay; plus, the edit-specific amplification worked only on the transfected samples and did not produce any amplicon from the negative control, implying specificity of the primer and an efficient knock-in. In line with this result, the NdeI digestion was positive only on the transfected pool of cells, suggesting again that the ssODN driven HDR was successful enough to proceed with the editing and clone selection.

Therefore, $1x10^6$ iPSCs were electroporated and plated on a VTN-coated 6mw plate; after 48 hours, we detached the cells, selected the ATTO488-positive subpopulation through flow cytometry and sorted one cell per well in a VTN-coated 96mw plate. The clones grew into single colonies, which were ready to be detached in about 15 days; at that time, part of the cell population was used to extract genomic DNA to evaluate the editing.

To identify the positively edited single clones, the DNA was extracted, amplified with primers flanking the region of editing and digested with NdeI enzyme; alongside, the DNA was amplified using edit-specific primers and wild-type primers (Primer MYO5B_2Fwt from Table 2, 430bp amplicon), the latter binding only if the edit had not occurred, to determine whether the mutation of interest have been inserted in homozygous or heterozygous form.

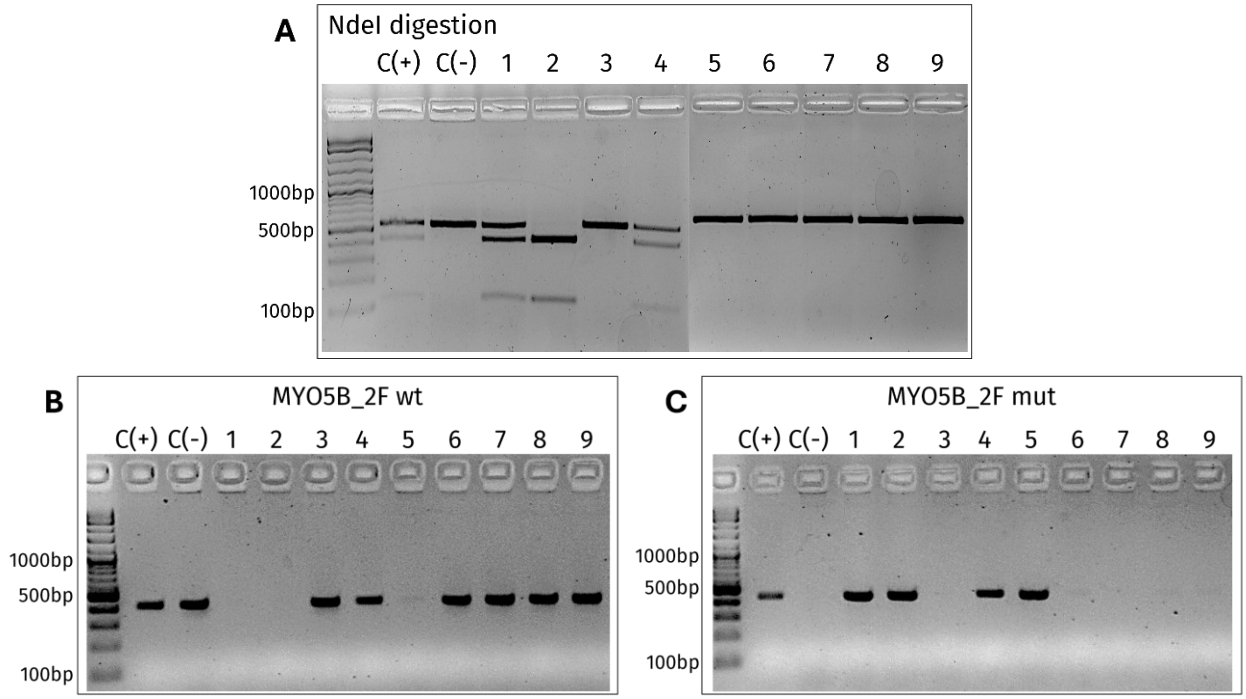

Figure 15: Screening of positive edited clones with NdeI digestion, edit-specific and wild-type amplification. C(+) represent the positive control, meaning DNA extracted from the bulk of cells after KI testing; C(-) represents the negative control, meaning DNA extracted from non-edited cells. Numbers 1 to 9 indicate DNA extracted from single clones obtained with single cell sorting after RNP/ssODN transfection. Quick-Load® 1 kb Plus DNA Ladder from NEB was used as molecular weight marker. (A): NdeI digestion of the region of edit amplified with MYO5B_1 primers from Table 2. (B): Wild-type PCR amplification, MYO5B_2Fwt primers from Table 2. (C): Edit-specific PCR amplification, MYO5B_2Fmut primers from Table 2.

Figure 15 shows the results of the screening of positive single clones: the clones positively amplified both with wild-type and edit-specific primer suggest that the mutation insertion occurred in heterozygosis; the clones amplified only with wild-type primers indicate that the editing did not happen, while the clones amplified only with edit-specific primers denote a homozygous insertion of the mutation. According to our results, clones 1, 2 and 5 are homozygous, clone 4 is heterozygous, and clones 3 as wells as 6 to 9 have not been edited.

When looking at the NdeI digestion, the restriction patter showed some conflicting data compared to the PCR: clones 1 and 4 appears to be heterozygous, while the only homozygous clone was clone 2; the not-edited clones are confirmed, with the addition of clone 5.

To confirm the DNA editing, we performed Sanger sequencing of the region of interest of the clones 1 and 2, as well as of clones 4 and 5, which PCR amplification and NdeI digestion did not match (Figure 16). The sequencing result confirmed all the above tests: clones 1, 2 and 5 presented the edit of interest in homozygosis, as the PCR indicated; similarly, the edit in clone 4 was inserted in heterozygosis. Interestingly, the silent mutations insertion did not correspond to the edit in every clone: Clone 2 and Clone 4 showed accordance in the zygosity of both silent mutations and the edit (every insertion in homozygosity for Clone 2 and heterozygosity for Clone 4); Clones 1 and 5, instead, were edited correspondingly for the missense edit and the second silent mutation (both homozygous in both clones), while the NdeI

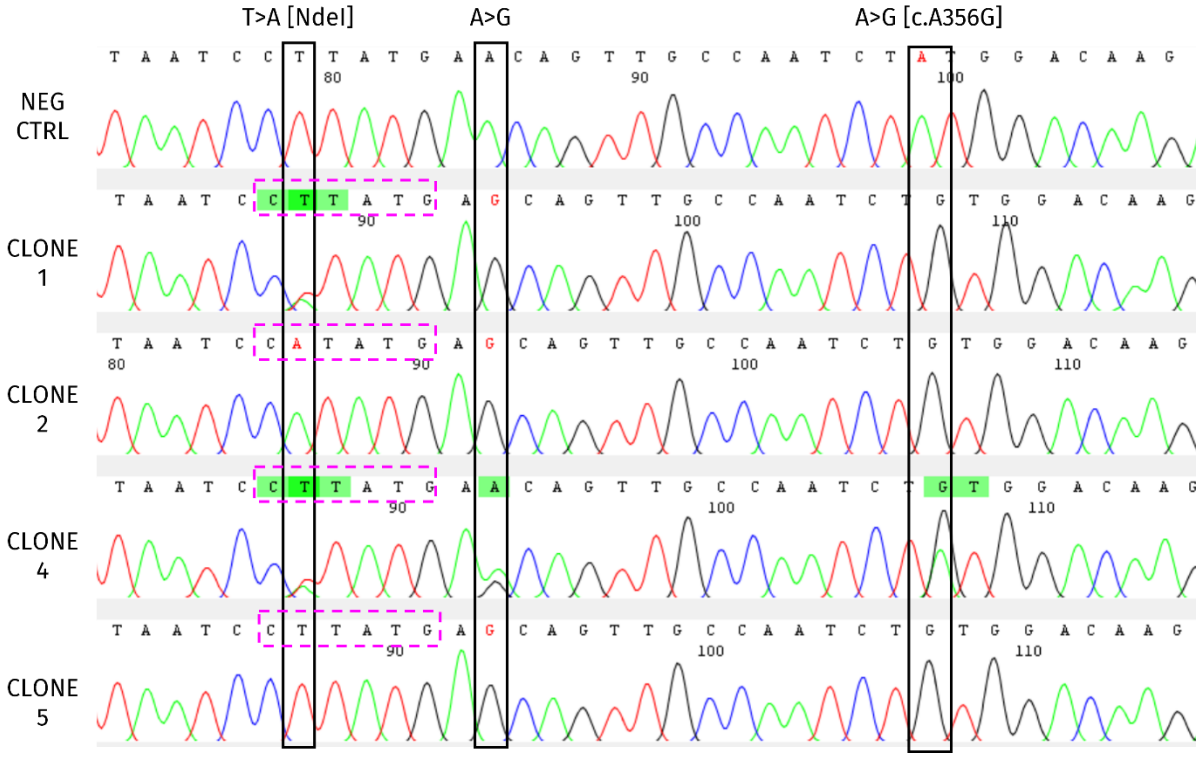

Figure 16: Sequencing results of clones 1,2,4 and 5 to confirm PCR and NdeI digestion results, compared with the sequence of a negative control (NEG CTRL). Highlighted with black boxes, the single nucleotide edits: T>A, silent mutation to insert a NdeI restriction site, first A>G, silent mutation, second A>G, missense edit of interest (c.A356G). In purple dotted boxes, the portion of the DNA corresponding to NdeI recognition sequence when the silent mutation is inserted (CATATG).

mutation was heterozygous in Clone 1 and was not inserted in Clone 5, as suggested by the former NdeI digestion.

Thus, designing the ssODN to include silent mutations that enable binding of an edit-specific primer and restriction enzyme digestion proved to be an effective strategy for screening positively edited clones, as all amplification and NdeI digestion results were consistent with the Sanger sequencing data.

6.3. 2D differentiation to hepatocyte-like cells

Among several *in vitro* hepatic models available nowadays, we started by testing two protocols to differentiate iPSCs to 2D hepatocyte-like cells. We aim to develop a model which replicates basic hepatic markers expression; plus, since the goal is investigating the mechanisms that lead to the cholestatic phenotype, it's crucial that the cells we obtain are polarized and able to reproduce *in vitro* the hepatocyte bile transport.

We tested one well described published protocol (Liu, Lamprecht, and Duncan 2018) and a kit from STEMCELL which, to date, have been published on a single manuscript but there are no information about membrane transporters (Nirgude et al. 2025). The protocols last 20 and 21 days total, divided into 4 intermediate steps: iPSCs, definitive endoderm (DE), hepatic progenitors (HP), hepatocyte-like cells (HLC). The media of the commercial kit are ready to use, while the specific media for each step of Liu et al protocol were prepared freshly according to the composition of Table 4 and changed daily. Representative pictures of the cells at every step are shown in Figure 17 and 18.

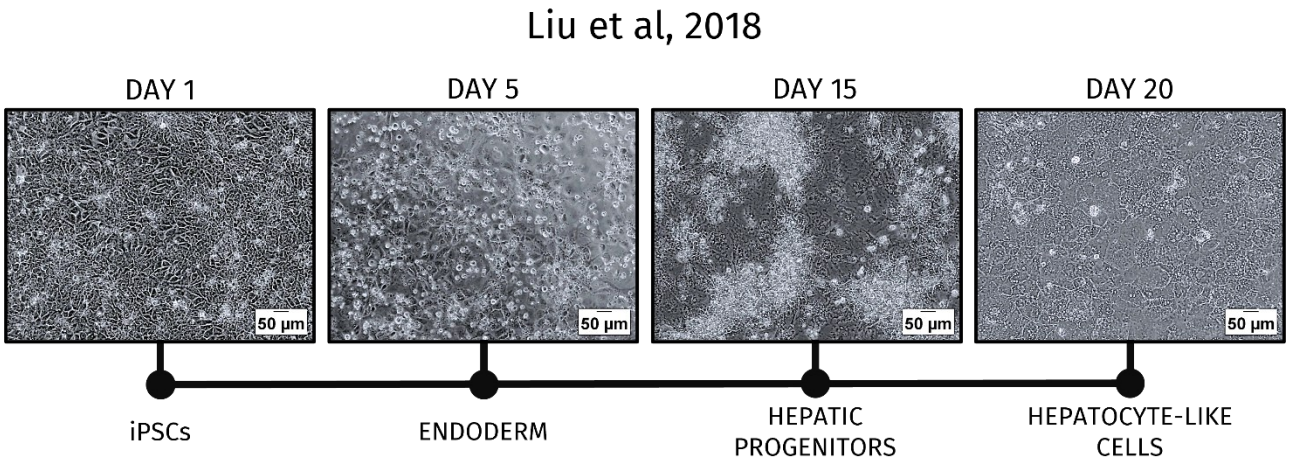

Figure 17: Brightfield pictures of the main steps of 2D differentiation protocol by Liu et al, 2018. The typical iPSC morphology, high nucleus-to-cytoplasm ratio, changes during endoderm shift to a rather cobblestone-like morphology which goes concurrently with an increase in cytoplasm. During hepatic precursor differentiation the cells gain a more hexagonal, epithelial shape which was even more pronounced at the end of the differentiation, where HLC exhibited a large polygonal morphology.

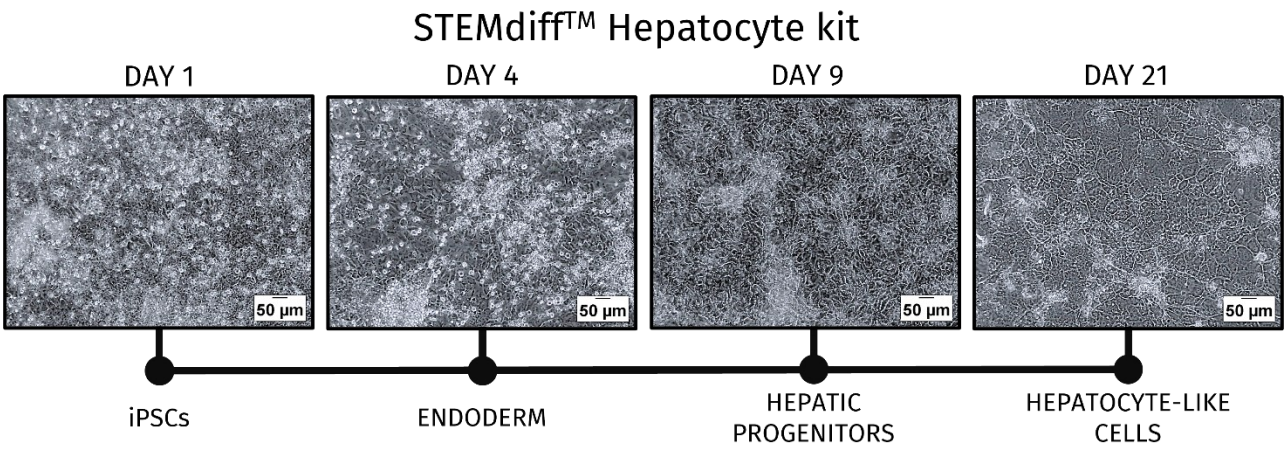

Figure 18: Brightfield pictures of the main steps of 2D differentiation protocol by STEMCELL kit. The iPSCs are seeded with a very high density, therefore cell death is more evident in the first picture; cell morphology changes when media drives towards endoderm stage, while maintaining compactness the cytoplasm widen, and cells assume a more rounded morphology. This morphology change continues in the next step, until reaching the HLC step were the cells displayed the expected polygonal shape with a large cytoplasm.

The morphology of the cells changed according to the protocol progression; starting from typical iPSCs characterized by high nucleus-to-cytoplasm ratio, the endoderm step cells appeared as a uniform and dense monolayer, accompanied by increased cytoplasmic volume. This morphology change was maintained when cells were driven to the hepatic lineage; the hepatic progenitors of Liu et al protocol already adopted a polyhedral shape, which is even more marked at the last step, where the cells appeared large and polygonal, displaying the characteristic epithelial morphology of hepatocytes with abundant cytoplasm and well-defined cell borders. In the STEMCELL kit differentiation, the hepatic progenitors still exhibited a dense layer and less pronounced cytoplasm enlargement compared to the first protocol; nevertheless, the HLCs after 21 days showed the typical hepatocyte morphology as described for the Liu et al protocol. In fact, although the endoderm and hepatic progenitor stages exhibited comparable yet not fully overlapping features between the two protocols, the resulting hepatocyte-like cells showed remarkably similar morphology.

At the end of every step, RNA was collected and reverse-transcribed to analyse changes in gene expression; thanks to quantitative Real-Time PCR the expression was compared to iPSCs as a pluripotency control and to Upcyte® hepatocytes (Upcyte technologies, CliniSciences Group) as a positive hepatic control. We detected the gene expression of 3 pluripotency markers (*SOX2*, *POU5F1*, *NANOG*) to confirm a decrease, and 7 hepatic markers (*ASGR2*, *SERPINA1*, *ALBUMIN*, *APOF*, *TTR*, *HNF4A*, *AFP*) to verify an increase in their expression. Gene expression was always normalized to GAPDH and ΔΔCt method was applied to relate the samples expression to controls; results are summarized in Figure 19 and 20.

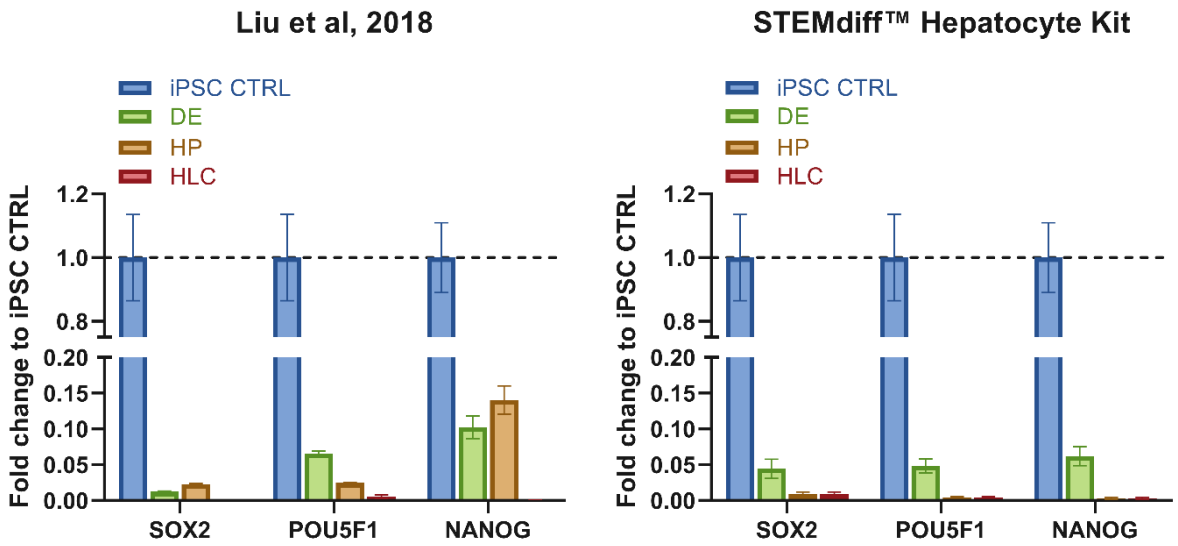

Figure 20: Gene expression of pluripotency genes of cells at different steps differentiated with 2D protocols. Gene expression was normalized to GAPDH expression and related to control iPSCs.

Overall, pluripotency genes expression decreases as the differentiation protocols continue; at the stage of endoderm and hepatic progenitors we detected some residual expression of these genes, but at the final stage of HLC there is no residual expression of any pluripotency marker, indicating that the pluripotency is eventually lost.

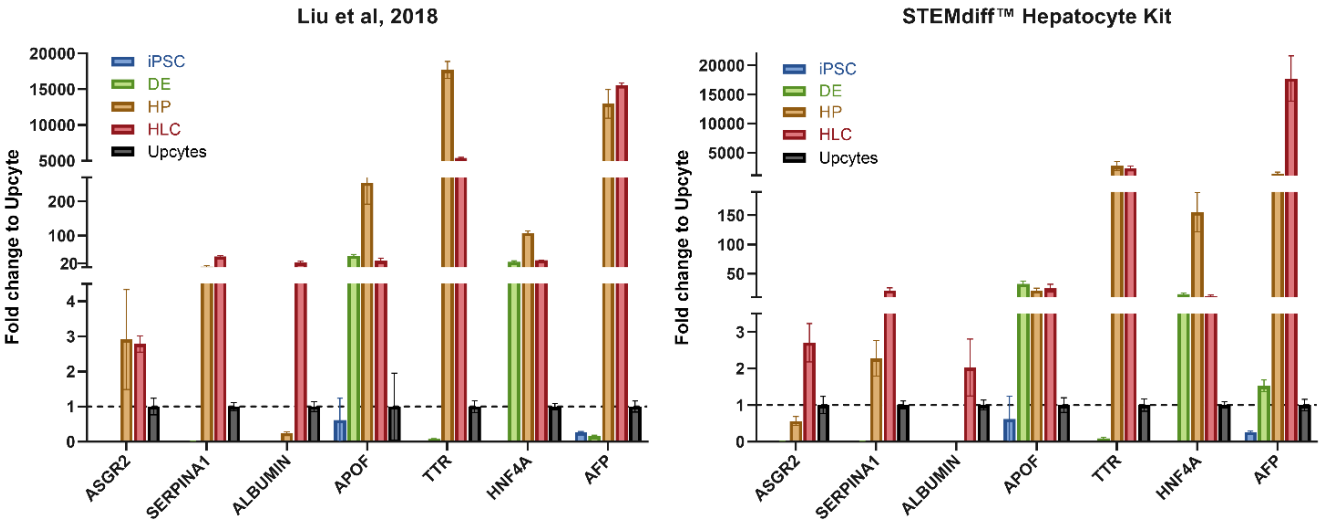

Figure 19: Hepatic markers gene expression at every step of the differentiation protocol; the values have been normalized to GAPDH and related to Upcyte expression. iPSCs are included as negative control.

Hepatic markers expression showed some differences between the protocols, but the overall picture is consistent between the two. The markers of hepatic protein secretion (*ASGR2*, *SERPINA1*, *ALBUMIN* and *TTR*) are expressed only in the last stages of induction (HP and HLC) with a general predominancy of expression in the very last days. *APOF*, which is involved in the lipid metabolism, and *HNF4A*, a transcription regulator of several hepatic

genes, were detected already at the DE stage; this corresponds to previously published differentiation data (Hay et al. 2008). Lastly, *AFP* encodes for the alpha-fetoprotein, which is a marker of immature hepatocytes and it's not expressed in healthy adult human liver; the expression of this gene in our samples is drastically higher than the expression in Upcyte cells, however it should be considered that the latter are primary cells isolated from human liver, thus a difference in *AFP* expression with 2D-differentiated hepatocytes should be expected.

We characterized these protocols also with immunofluorescence staining at the final stage (HLC) to confirm the silencing of a pluripotency marker (OCT4) and the expression of hepatic indicators (Albumin and HNF4α), plus to explore the expression and localization of some polarity markers, both basolateral (E-Cadherin) and apical (ZO-1, BSEP, MRP2).

As illustrated in Figure 21 and 22, the hepatocyte-like cells obtained after 20 or 21 days of differentiation, showed no expression of the pluripotency marker OCT4 and a correct expression and localisation of two standard hepatic markers, the albumin in the cytoplasm and the transcription factor HNF4α in the nucleus. E-cadherin, a cell-cell junction basolateral marker, and ZO-1, a tight junction protein of the apical membrane, were detected throughout the entire cell membrane, while MRP2 and BSEP signals were interspersed in the cytoplasm with a dotted pattern and some non-specific signal in the nucleus.

In these protocols, if the hepatocytes are arranged in a polarized manner the basolateral membrane would be the portion in contact with the matrix-coated support and between the cells, while the apical membrane would be facing upwards the cell monolayer (C. Z. Li et al. 2022). To verify through immunofluorescence if there are evidence of cell polarity, we performed a Z-stack imaging of the hepatocyte-like cells (Figure 23).

Across both protocols, ZO-1 seemed to be correctly localised as discrete clusters between one cell and the next, however E-cadherin exhibited some membrane localization but lacked basolateral specification. The canalicular transporters BSEP and MRP2 displayed a diffuse cytoplasmic distribution; BSEP in Liu et al protocol showed some membrane signal enrichment, nevertheless Z-stack imaging demonstrated that no polarization is present. On the contrary, MRP2 staining in the *STEMdiff kit* HLC was strong and specific, yet unfortunately it wasn't membrane associated as desired.

Taken together, gene expression and imaging analyses revealed that iPSCs can be differentiated into hepatocyte-like cells in 2D culture, but these cells lacks the apical-basolateral polarization required to model cholestasis.

Liu et al, 2018

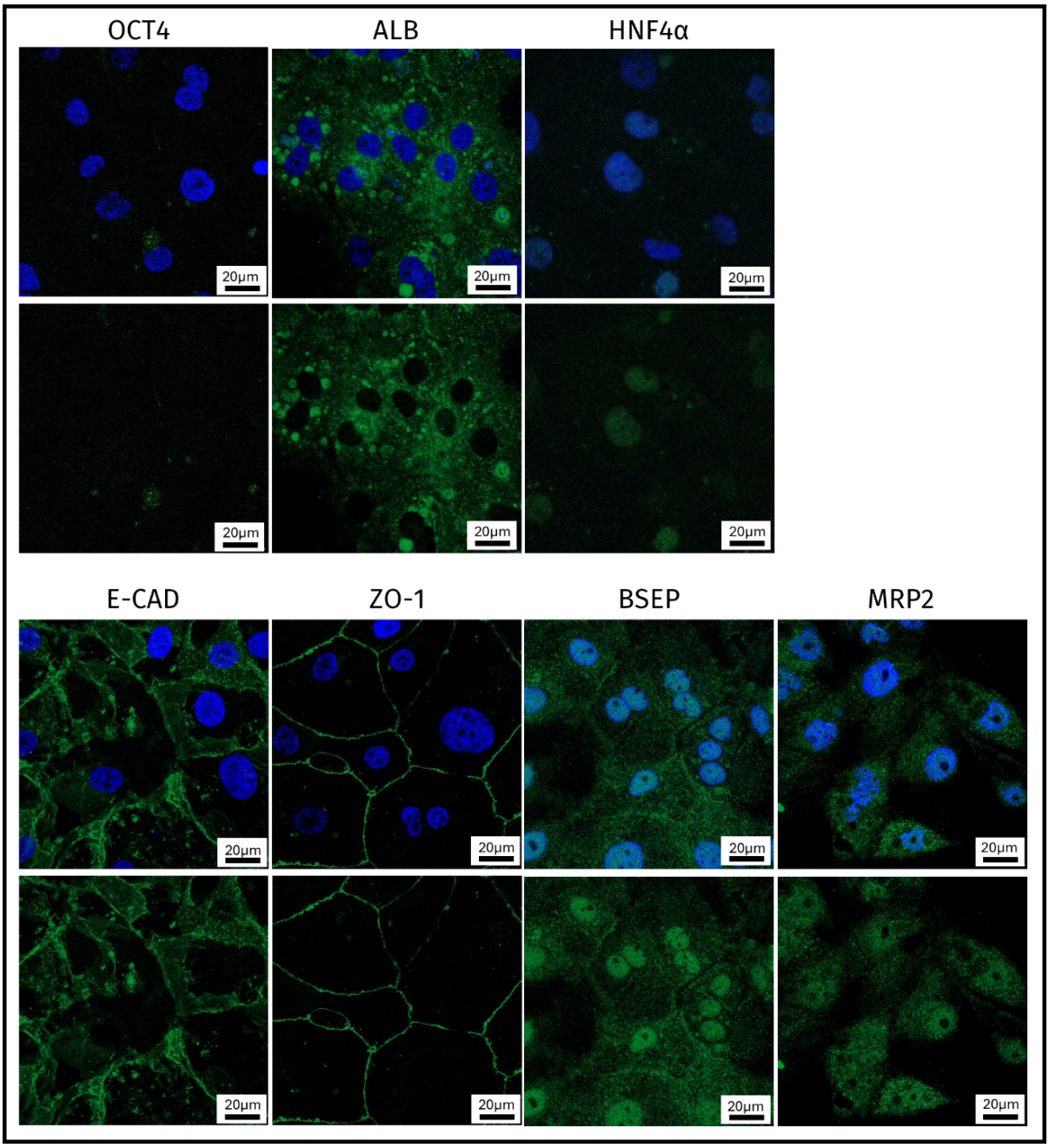

Figure 21: Immunofluorescence staining of HLC of pluripotency markers, hepatic markers and polarity markers at Day 20 of Liu et al protocol. For each marker, on the upper line DAPI is stained in blue and the protein of interest is stained in green; on the bottom line, the corresponding protein is shown alone. From left to right and top to bottom: the pluripotency marker OCT4 expression is not detectable; the hepatic markers Albumin (ALB) and HNF4α are properly expressed and localised in the cytoplasm and in the nucleus, respectively; the basal E-cadherin (E-CAD) and the apical Z0-1 were both detected along the cell membrane; the canalicular bile acid transporters BSEP and MRP2 signals showed a mostly cytosolic localisation, with some non-specific signal in the nucleus. BSEP exhibited a slightly more intense localisation on the cell membrane.

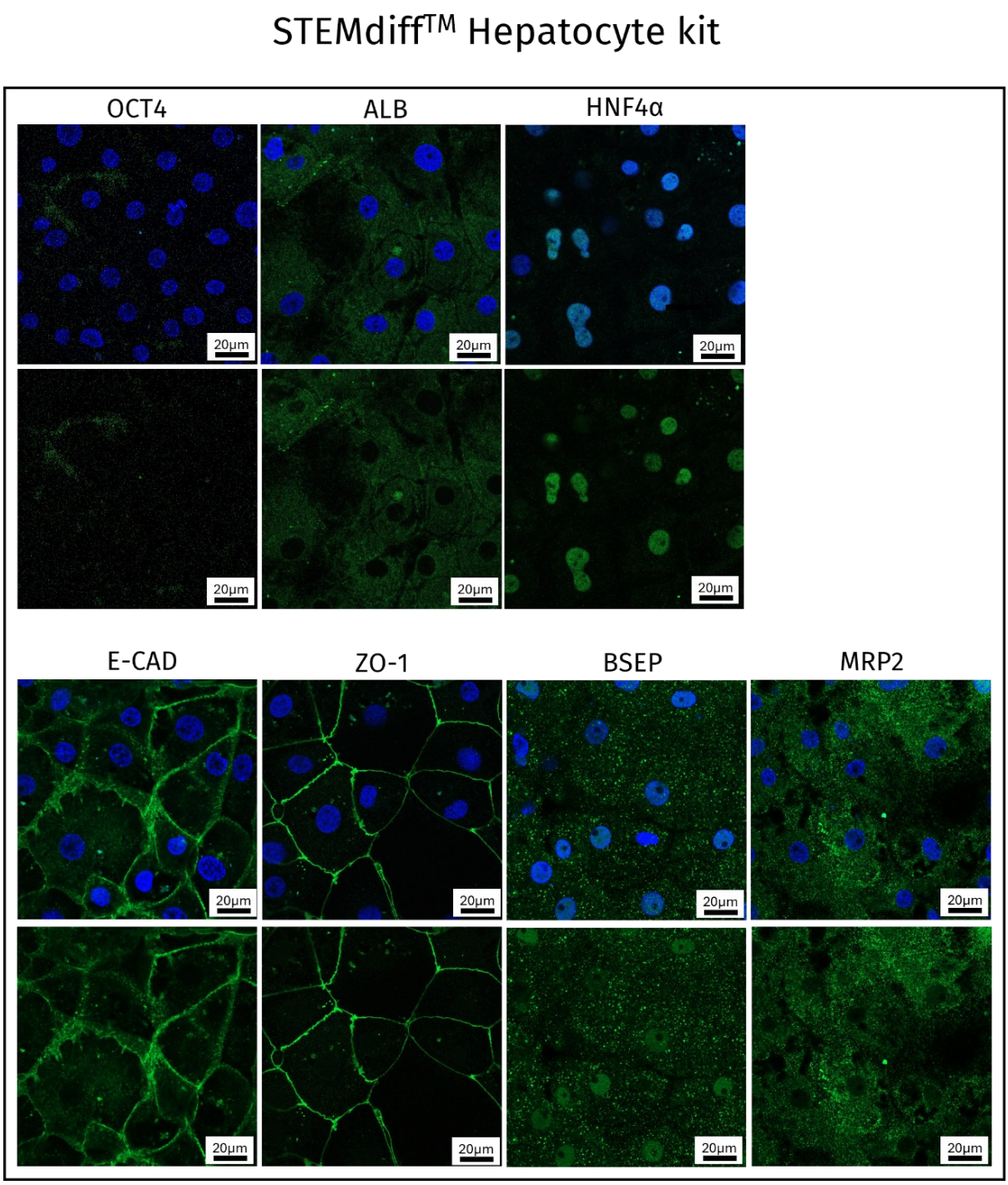

Figure 22: Immunofluorescence staining of HLC of pluripotency markers, hepatic markers and polarity markers at Day 21 of STEMdiff™ Hepatocyte kit protocol. For each marker, on the upper line DAPI is stained in blue and the protein of interest is stained in green; on the bottom line, the corresponding protein is shown alone. From left to right and top to bottom: the pluripotency marker OCT4 expression is absent; the hepatic markers Albumin (ALB) and HNF4α are correcly expressed and localised in the cytoplasm and in the nucleus, respectively; the basal E-cadherin (E-CAD) and the apical Z0-1 were both detected along the cell membrane; the canalicular bile acid transporters BSEP and MRP2 signals showed a mostly cytosolic localisation, with some non-specific BSEP signal in the nucleus.

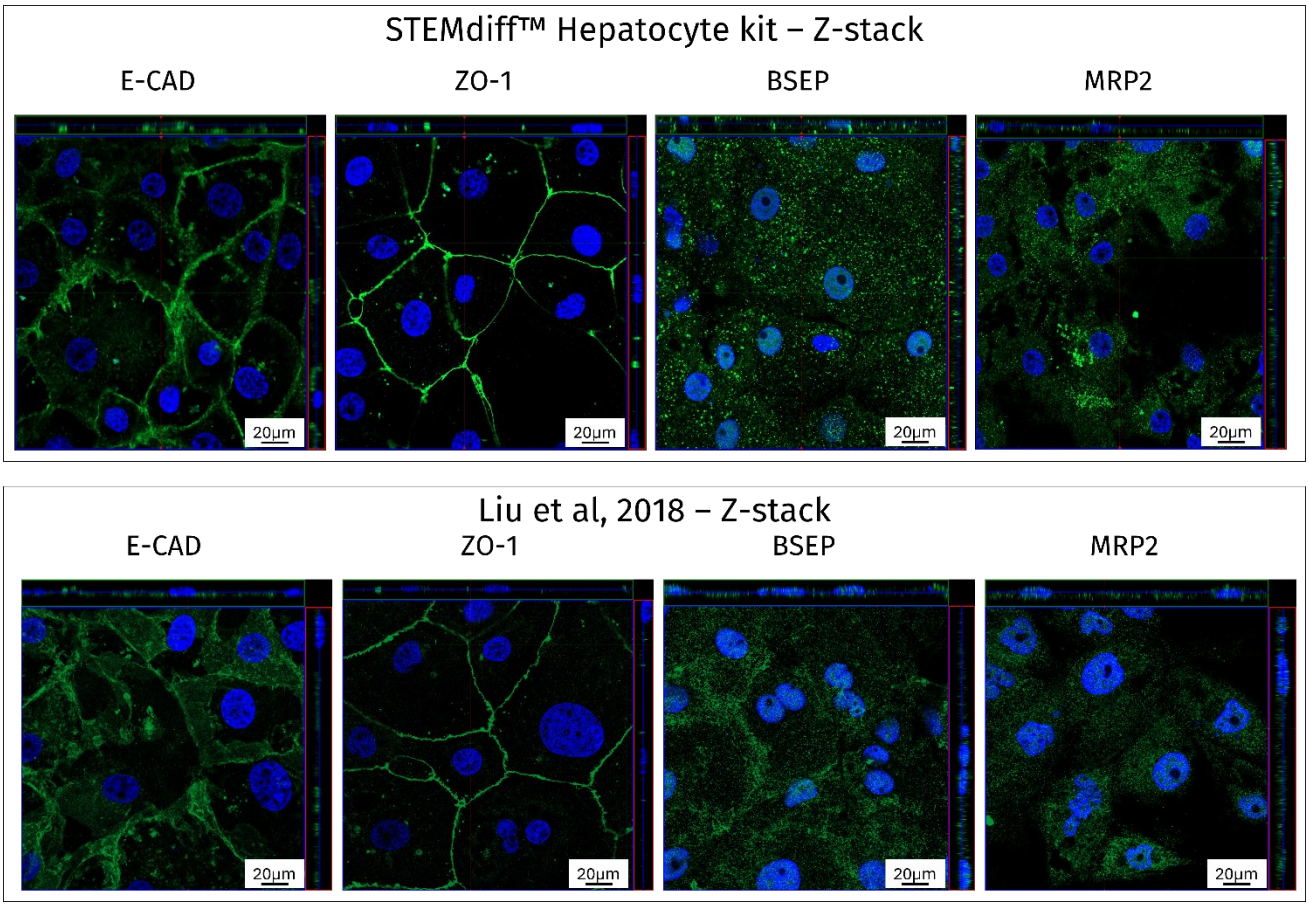

Figure 23: Z-stack imaging of hepatic-like cells monolayer at Day 20 for Liu et al protocol and Day 21 for STEMdiff™ Hepatocyte kit protocol. DAPI is stained in blue and the protein of interest is stained in green; for each staining, the central picture is the result of one focal plane imaging, on the side is shown the Z-stack imaging of a vertical axis, on the top is shown the Z-stack imaging of a horizontal axis. For both protocols, from left to right: E-cadherin signal is mainly on the cell membrane but does not display a basolateral localisation; the apical ZO-1 signal appears as defined spots between the cells; BSEP and MRP2 signals are diffuse in the entire cytoplasm, without a strong canalicular localisation.

6.4. Blood-derived iPSCs

iPSCs were reprogrammed from peripheral blood mononuclear cells (PMBCs) at prof. Cantz group at Hannover Medical School, Hannover, Germany; samples were collected from a healthy subject to use as control and from the patient HC01. This patient was diagnosed with MASLD and suffered from recurrent episodes of intrahepatic cholestasis; a genetic investigation revealed 3 heterozygous variants in *ABCB4*, *ABCB11*, and *MYO5B*. Pluripotency assessment of the generated iPSCs lines was provided by prof. Cantz group: both cell lines showed high pluripotency markers, both nuclear and membrane, evaluated respectively with immunofluorescence assays and flow cytometry; karyotyping analysis also revealed a normal

chromosomal asset. Moreover, both cell lines lost Sendai-virus genes expression after passage 8, confirmed by quantitative Real-Time PCR (Sgodda et al. 2025).

6.5. 3D organoids differentiation

Pluripotent stem cells derived from blood and urine were differentiated to 3D hepatobiliary organoids; the protocol was developed and optimized by professor Cantz group starting from an available manuscript from 2021 (Shinozawa et al. 2021; Sgodda et al. 2025). This differentiation procedure is divided into two steps: a first 2D differentiation from iPSCs to foregut endoderm, and a second 3D differentiation which results in spheroid structures that replicate some hepatic features; the cells are organized in a polarized arrangement, featuring an apical membrane inwards and a central canalicular space, while the basolateral membrane is positioned between the cells and along the outer surface of the organoids. Although these structures do not fully replicate the complexity of the liver, they have demonstrated the ability to recapitulate hepatobiliary transport *in vitro*, which is sufficient to investigate the effects of genetic variants associated with the cholestatic phenotype.

Representative brightfield pictures of the cells and the organoids at different stages of differentiation are shown in Figure 24 and 25.

Brightfield imaging of 2D differentiation of iPSCs to foregut endoderm highlights the stage-specific morphological changes: one day after seeding, cells displayed the expected iPSC morphology and had not yet reached confluence; following three days of culture in endodermal induction media, the monolayer became confluent and the cells assumed a more cuboidal

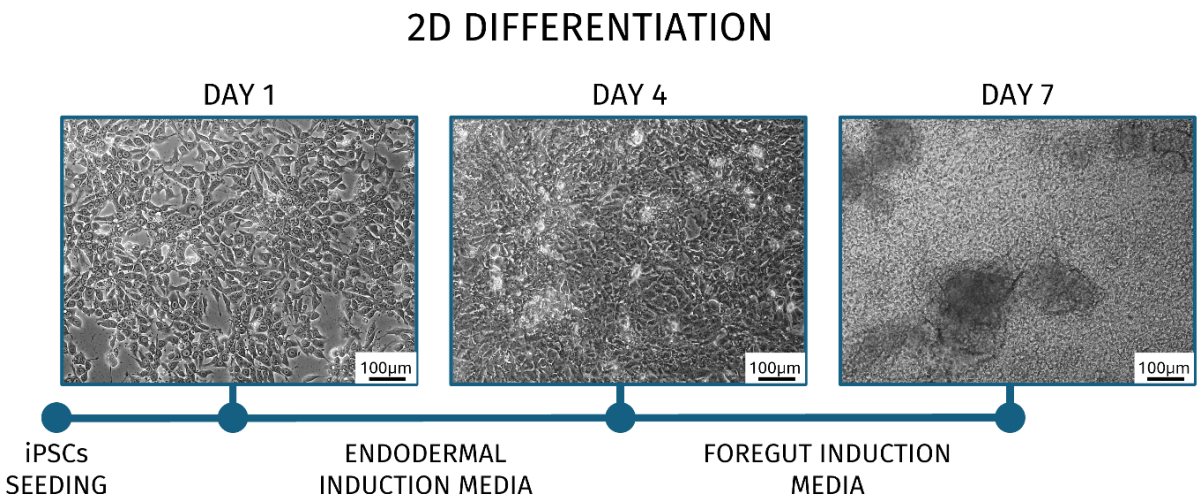

Figure 24: Representative brightfield pictures of 2D differentiation from iPSCs to foregut endoderm. From the left, cells the day after seeding (Day 1) show typical iPSCs morphology when freshly passaged and not confluent yet; after 3 days of endodermal induction media, cells are confluent, with a more cuboidal shape and some cell clusters start to form; at the Day 7, cells are remarkably dense, and clusters are growing on top of the monolayer.

shape, with early signs of clustering. By Day 7, the culture exhibited high density, characterized by the growth of cell aggregates over the established monolayer.

Figure 25 shows the development of organoids from foregut endoderm; single cells were encapsulated in pure Geltrex matrix to initiate the 3D culture, and this implicate that during the first 48 hours a portion of the population did not survive. The majority of the cells remained viable and began to proliferate, establishing small aggregates; by Day 5, these clusters expanded in size consistent with increasing cell division. On Day 9, some morphological divergence can be observed: part of the cells spread through the matrix forming a non-specific population, while the organoids adopted a spherical morphology, continuing to grow and establishing apical-basal polarity.

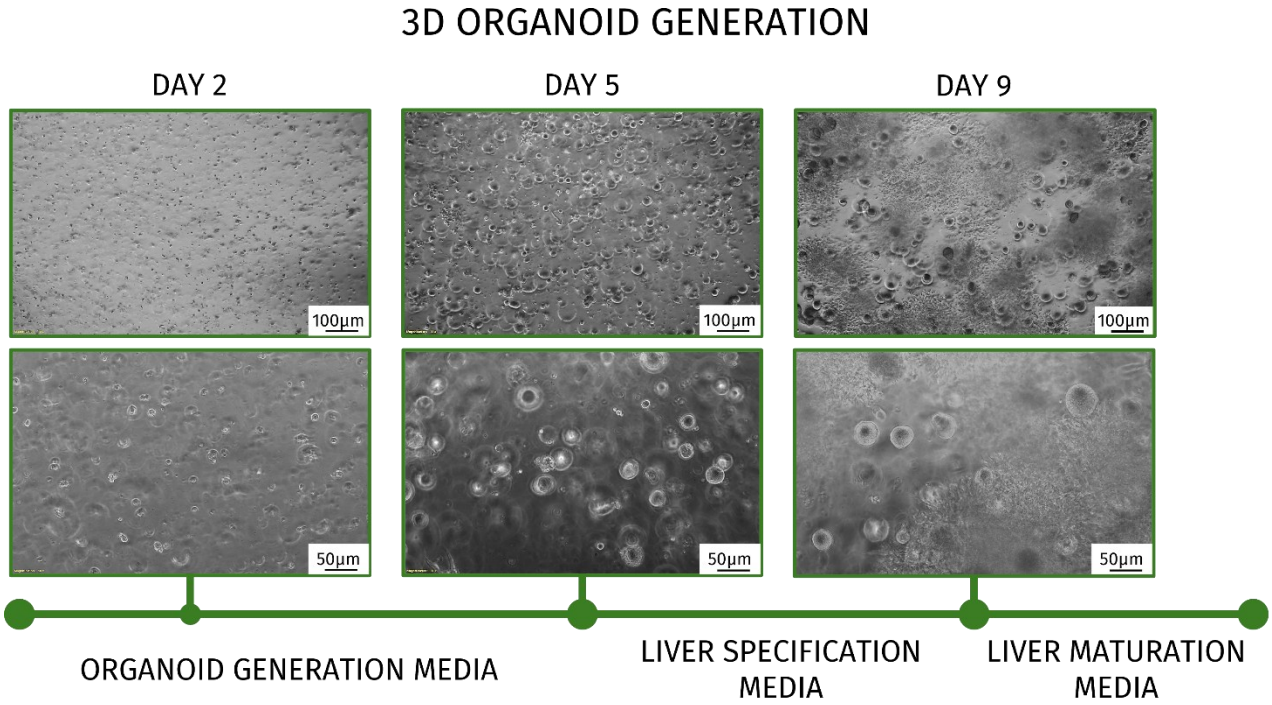

Figure 25: Representative brightfield pictures of 3D organoid generation. Foregut endoderm cells are seeded as single cells in pure Geltrex matrix; in the first 2 days part of the cell population doesn't survive, while the live cells start to proliferate in small clusters; at Day 5 this cell clusters are increasing in size because of increasing cell number; at Day 9, some cells are expanding in the matrix and proliferating into a net of non-specifically differentiated population, while the organoids are shaping into round structures which keep growing and gaining apical-basolateral polarization.

To evaluate the successful differentiation and polarization we stained two apical markers (the bile acid transporters BSEP and MRP2) and one basolateral marker (the bile acid uptake transporter OATP1B1) through immunofluorescence assays. In Figure 26 are reported pictures of the organoids generated from the blood-derived iPSCs; this figure is an adjustment of the data recently published by prof. Cantz group (Sgodda et al. 2025). The upper line contains the picture taken from the healthy control organoids, where BSEP and MRP2 are correctly localised along the inner apical membrane, while OATP1B1 is detected on the outer and between cells basolateral membrane. The bottom line includes the organoids generated from

the cholestatic patient HC01, where all three polarity markers are not clearly localised on any membrane but appear as cytoplasmatic.

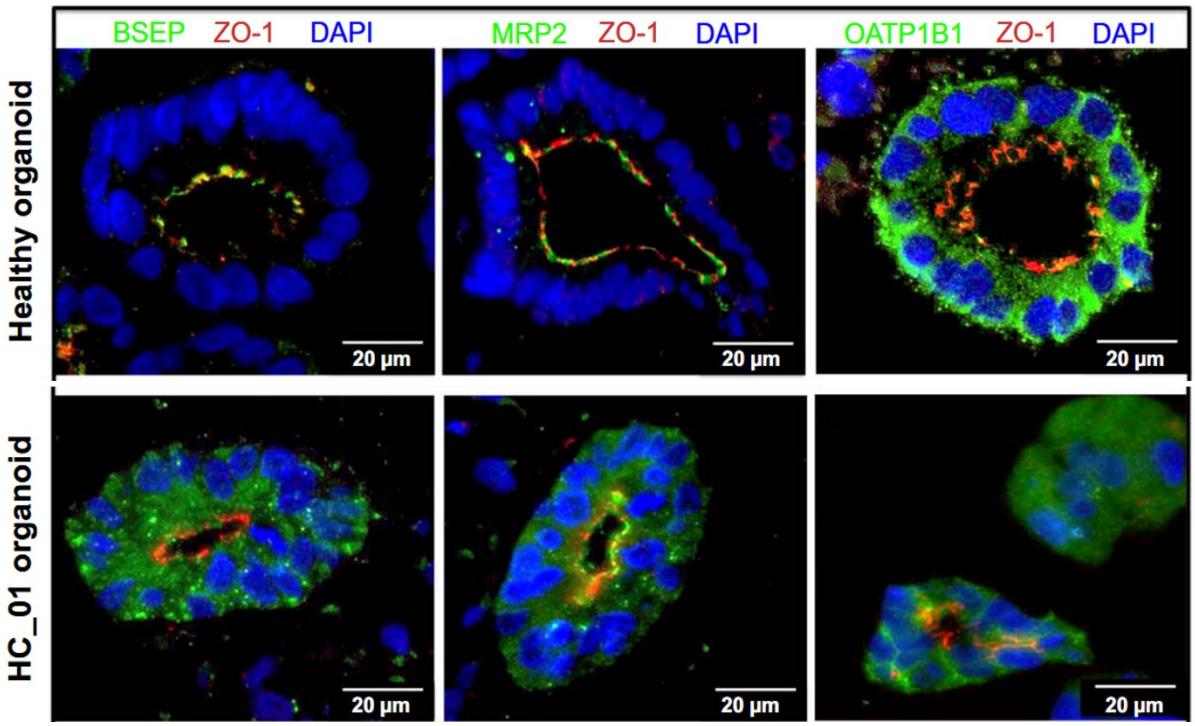

Figure 26: Immunofluorescence assay to evaluate polarization in healthy control and HC01 blood-derived cell lines, adapted from Sgodda et al, 2025. In every picture, nuclear DAPI is stained in blue, apical marker ZO-1 in red, and the protein of interest in green. On the upper line, healthy organoids exhibited correct localisation of BSEP and MRP2 on the inner apical membrane, while OATP1B1 is correctly localised on the basolateral membrane between the cells and on the outer side. On the bottom line, HC01-derived organoids displayed a smaller inner lumen, as well as a mostly cytoplasmatic localisation of the stained markers; MRP2 signal was weakly enriched in the canalicular membrane, and OATP1B1 in some organoids showed a stronger signal on the membrane between cells.

The following Figure 27 displays the organoids generated from the urine derived iPSCs, from the wild-type healthy donor cell line and from the *MYO5B*-edited cell line. It is evident that the localisation of the transporters is not correctly established, not even in the wild-type organoids; the BSEP and MRP2 signals were predominantly dispersed throughout the cytoplasm, although some signal suggested a slightly increased localisation of both proteins at the apical membrane. OATP1B1, particularly in the wild-type cell line, did not exhibit the expected basolateral membrane localisation, it showed instead a diffuse signal within the cytosol.

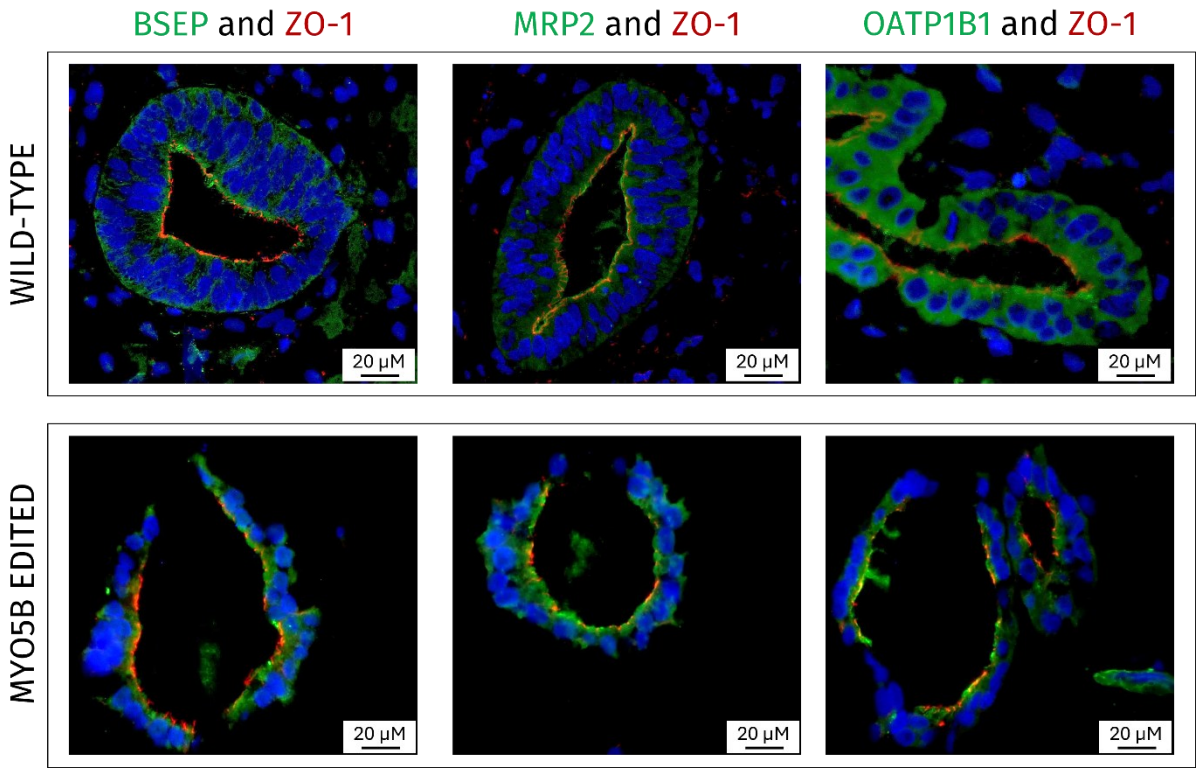

Figure 27: Pictures of immunofluorescent staining of organoids generated from urine derived iPSCs. For each picture, nuclear DAPI was stained in blue, the apical marker ZO-1 was stained in red, and the protein of interest was stained in green. On the upper line, organoids derived from the wild-type control cell line; despite some stronger signal on the canalicular membrane, BSEP and MRP2 are cytoplasmatic, while OATP1B1 signal is strong in the entire cytoplasm with no enrichment on any membrane. On the bottom line, organoids derived from the MYO5B edited cell line; all three markers are localised similarly, with some marked signal along the inner canalicular membrane and diffuse cytosolic signal alongside.

6.6. Transgene expression analysis on urine-derived iPSCs

Given the inefficient differentiation of both wild-type and *MYO5B* edited urine-derived iPSCs to 3D organoids, we first verified if the 2D differentiation of these cell lines from iPSCs to endoderm was successful; to do so, we stained foregut endoderm cells derived from urine and from blood with two membrane markers, named CD117 (or c-Kit) and CXCR4 (Holtzinger et al. 2015), labelled with APC and PE fluorophores respectively, and analysed them with flow cytometry. The corresponding results are shown in Figure 28; on the upper line, the blood-derived endoderm cells showed a distinct and strong staining of both markers, with a notable fluorescence histogram shift. On the bottom line, the urine-derived cells exhibited an unusual behaviour: CXCR4 staining resulted in a clear shift of the whole population, however unstained cells in the CD117 analysis displayed the same fluorescence intensity as stained cells in the PE channel, with only a small sub-population showing a low fluorescence intensity.

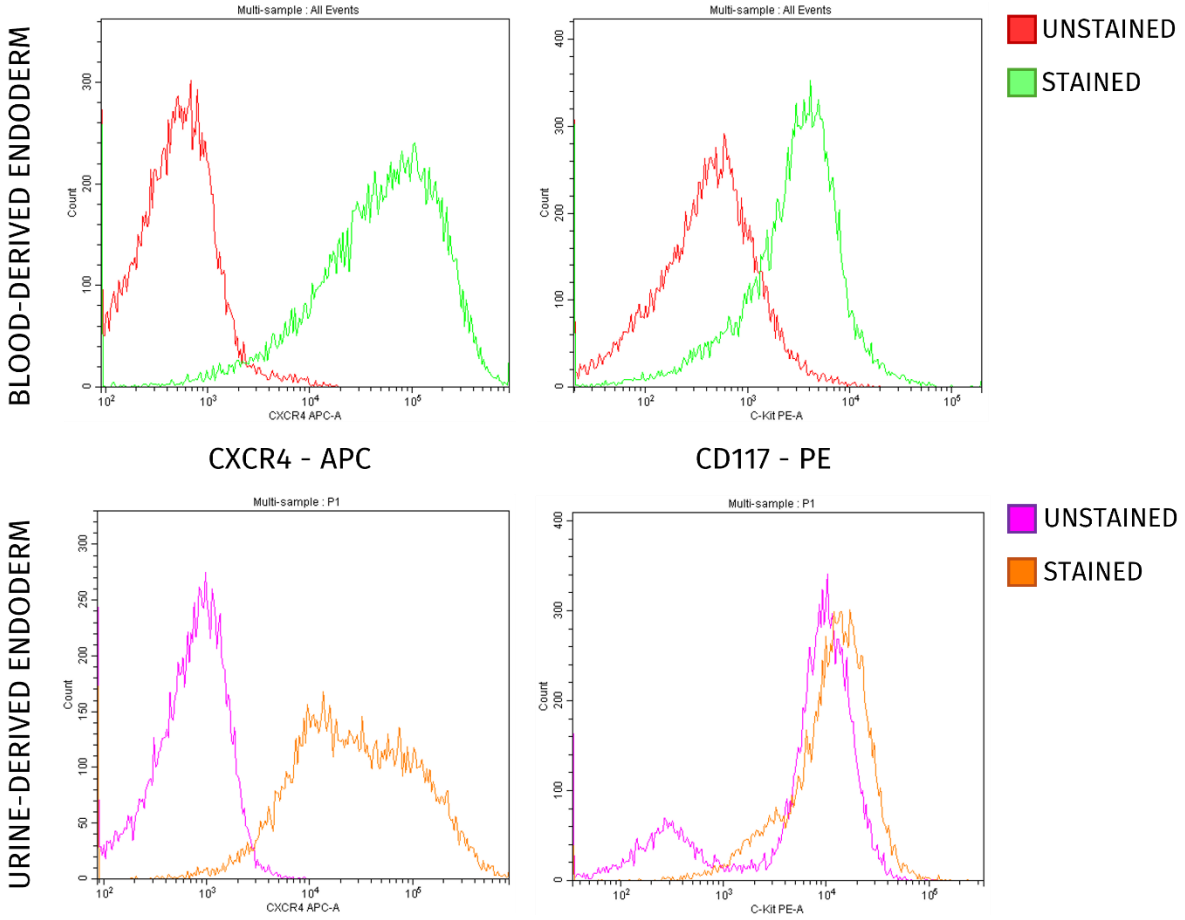

Figure 28: Flow cytometry analysis of endoderm markers, CXCR4 and CD117, on blood-derived and urine-derived cells. On the upper line, blood-derived endoderm histograms, unstained samples in red and stained samples in green. On the bottom line, urine-derived endoderm histograms, unstained samples in purple and stained samples in orange. For both lines, CXCR4-APC staining on the left and CD117-PE staining on the right.

We explained this unexpected result with a residual expression of the dTomato gene which was present as a reporter in the reprogramming plasmid used for the integrating method on the urinary cells (plasmid pRRL.PPT.SF.hOct34co.hKlf4co.hSox2co.hmyc.dTomato.pre.FRT, kindly donated to Doctor Bellarosa at FIF by Prof. Baum and Prof. Schambach from Hannover Medical School, Germany), since dTomato and PE excitation and emission spectrum are comparable; this assumption implies that the integrating transgenes are still expressed.

To verify if the viral integrated genes have been correctly silenced by the endogenous machinery of the cells, we performed a PCR on these urine-derived iPSCs cDNA. The PCR was set up as already described in the method section with primers Transgene RT from Table 2, which were designed to anneal specifically on the codon optimized viral gene and not on the endogenous DNA; therefore, if the inserted transgenes are still expressed we would find a corresponding amplicon of 721bp, on the contrary the absence of an amplicon means that the genes have been silenced.

The resulting agarose gel is shown in Figure 29: iPSC cDNA is the sample of interest, the negative control is cDNA from blood-derived iPSCs (reprogrammed without integration), then urine-derived iPSC genomic DNA and DNA from the reprogramming plasmid were amplified as positive controls.

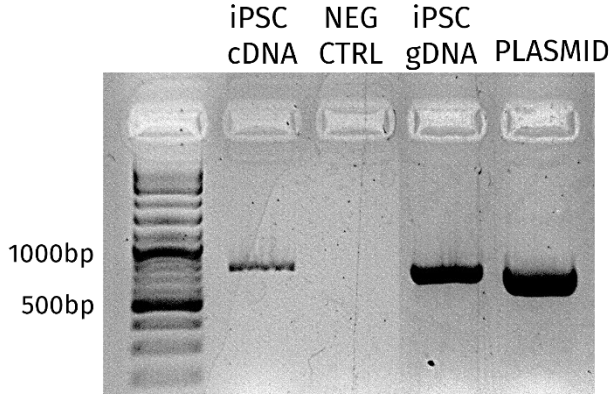

Figure 29: PCR amplification of lentiviral integrated transgenes. Quick-Load® 1 kb Plus DNA Ladder from NEB was used as molecular weight marker. iPSC cDNA is the sample of interest, reverse-transcribed from urine-derived iPSCs; NEG CTRL corresponds to blood-derived iPSCs; iPSC gDNA corresponds to urine-derived iPSC genomic DNA

PCR confirmed the presence of residual viral reprogramming gene expression in urine-derived iPSCs, consistent with the elevated autofluorescence detected in unstained controls. Given this persistent transgene expression, the integrating method-derived cell line and all subclones were excluded from further experimental work.

6.7. Biliary transport assays

MYO5B plays a crucial role in the trafficking of apical proteins to the canalicular membrane. To investigate how *MYO5B* mutations affect bile canaliculi formation and BSEP function, we performed functional transport assays in hepatic organoids. Biliary transport assay was performed on organoids differentiated from blood-derived iPSCs; this assay exploits two fluorescently labelled bile acid analogues, called CLF and Tauro-DBD, secreted in the canalicular space respectively by MRP2 and BSEP. The organoids were harvested at Day 12 of 3D differentiation and incubated with both molecules for different time intervals; at the end of each incubation, the organoids were washed and plated on a plate to capture brightfield images, as well as green channel and red channel images corresponding respectively to CLF and DBD-Tauro emission.

Figure 30 shows the results of the analysis of the biliary transport assay of the healthy control, determined as described in the method section. This semi-quantitative analysis revealed that the signals originating from both CLF (green dots) and Tauro-DBD (red dots) increased in a time-dependent manner; this trend indicates that the MRP2 and BSEP mediated

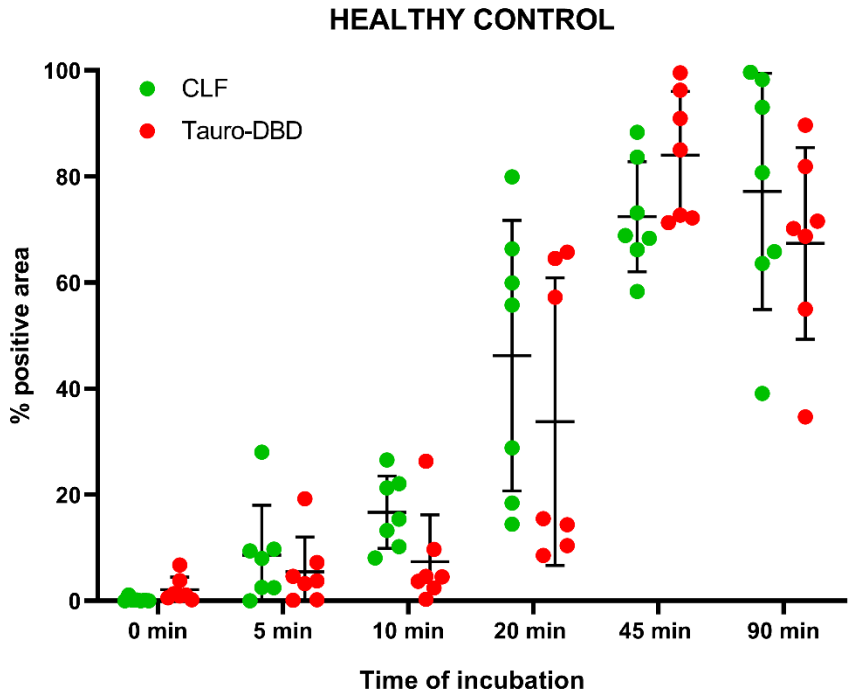

Figure 30: Biliary transport assay of healthy control organoids from blood-derived iPSCs. For each time point, every dot corresponds to at least 7 organoids, and the data are represented as the mean ± SD of the percentage of fluorescent positive organoids area.

transport responsible for the passage of these molecules through the 3D structures is functioning properly. The fluorescent signal of both bile acid analogues is already detectable after 5 minutes of incubation with similar intensity (CLF 5 min = 8,61±9,39; Tauro-DBD 5 min = 5,50±6,56); in 10 minutes CLF signal increases at a higher rate than Tauro-DBD (CLF 10 min = 16,71±6,80; Tauro-DBD 10 min = 7,38±8,84), and at 20 minutes we registered the wider fluctuation for both (CLF 20 min = 46,25±25,50; Tauro-DBD 20 min = 33,77±27,12). The analogues signals continue to increase together until 45 minutes (CLF 45 min = 72,42±10,37; Tauro-DBD 45 min = 84,01±12,04), while after a total of 90 minutes incubation the CLF increase is minimum and Tauro-DBD signal start to slowly decrease (CLF 90 min = 77,18±22,28; Tauro-DBD 90 min = 67,40±18,07), indicating that a saturation was reached and 45 minutes incubation is sufficient to track BSEP and MRP2 transport in the organoids.

The overall picture indicates that the biliary transport is reproduced *in vitro* by the generated organoids, making them a solid model to explore the genetic-driven cholestatic phenotype.

We then performed the same transport assay on the HC01 organoids to compare the results with the healthy control (Figure 31). While MRP2-associated transport of green CLF increases in parallel with longer incubation and a behaviour comparable to the healthy control (0 min = 3,19±3,44; 5 min = 8,85±6,42; 10 min = 25,42±18,38; 20 min = 57,02±13,97; 45 min = 83,60±11,56), the red signal of Tauro-DBD remain close to zero for up to 45 minutes (0 min = 0,00±0,00; 5 min = 0,07±0,10; 10 min = 0,15±0,22; 20 min = 0,12±0,13; 45 min = 0,12±0,10).

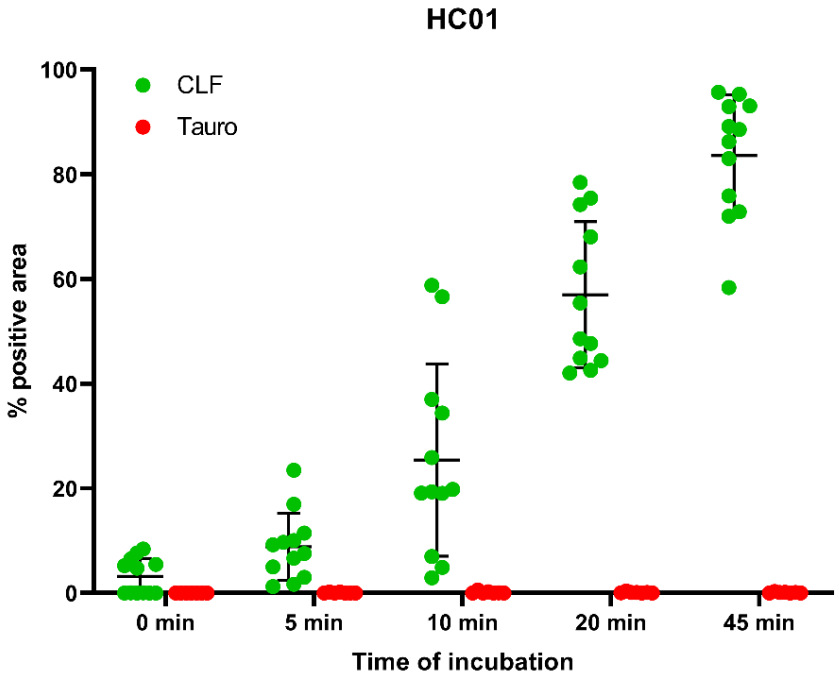

Figure 31: Biliary transport assay of HC01 organoids from blood-derived iPSCs. For each time point, every dot corresponds to at least 7 organoids, and the data are represented as the mean ± SD of the percentage of fluorescent positive organoids area.

It can be concluded that MRP2-mediated transport is not affected by the patient mutations in HC01 organoids; in contrast, in this *in vitro* model BSEP-mediated transport appears to be completely abolished, which was not expected for a *MYO5B* heterozygous mutation.

6.8. Generation of *MYO5B*-mRNA lipid nanoparticles

Prof. Cantz research group in Hannover demonstrated that the *MYO5B* mutation carried by HC01 patient cells is the main responsible of the disturbed polarity and BSEP impaired transport in the organoids (Sgodda et al. 2025).

To attempt a functional rescue of the BSEP-mediated transport we transfected HC01 derived organoids with liver specific lipid-nanoparticles delivering *MYO5B* mRNA; we hypothesized that the heterozygous mutation on the patient *MYO5B* gene may lead to an haploinsufficiency, therefore an overexpression of wild-type protein could recover partially or totally BSEP altered function.

The commercially acquired plasmid contains *MYO5B* full-length ORF tagged with DDK-tag and MYC-tag; first, due to a complication with two BspQI enzyme restriction sites for further experimental work, we performed two subsequent events of site-directed mutagenesis to delete those from the *MYO5B* ORF sequence.

The results of the control BspQI digestion of the isolated clones after the first and the second mutagenesis are shown in Figure 32. The original plasmid presents four BspQI restriction site, resulting in 4 fragments after the enzyme digestion (4174bp, 3344bp, 2697bp, 210bp); after the first site deletion the positive clones presented 3 restriction sites resulting in 3 fragments (7518bp, 2697bp, 210bp), and after the second mutagenesis the positive clones carried 2 restriction sites and 2 fragments (10215bp, 210bp).

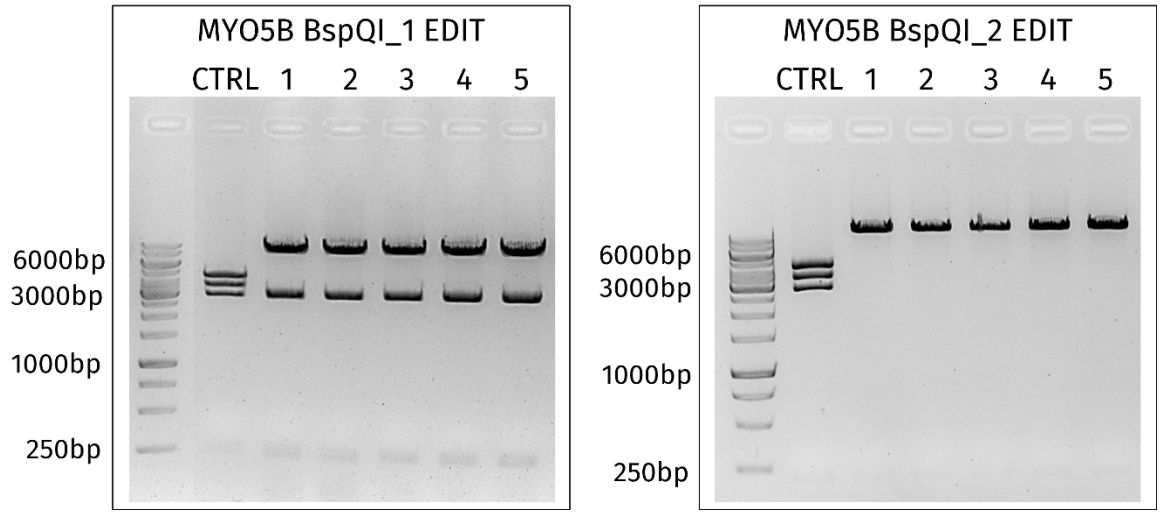

Figure 32: Results of the BspQI control digestion after site-directed mutagenesis. GeneRuler 1 kb DNA Ladder by Thermo Fisher Scientific was used as molecular weight marker. CTRL corresponds to the original plasmid before any edit (4174bp, 3344bp, 2697bp, 210bp); on the left the results of the deletion of the first restriction site (MYO5B BspQI_1 EDIT, Clones #1 to #5, 7518bp, 2697bp, 210bp), on the right the results of the second deletion (MYO5B BspQI_2 EDIT, Clones #1 to #5, 10215bp, 210bp).

Once both BspQI site were deleted from *MYO5B* sequence, we proceeded with deleting Exon 30 from the *MYO5B* sequence, since there is evidence in literature that the functional isoform of MYO5B in the liver lacks Exon 30 (Roland, Lapierre, and Goldenring 2009). We performed SDM with the same procedure, using the appropriately designed primers; to select the positive clones we ran a XhoI digestion, which led to 3 bands on agarose gel: if Exon 30 is included in the sequence, the detected fragments were 8600bp, 1470bp, and 333 bp long, while if Exon 30 is eliminated the resulting fragments corresponded to 8600 bp, 1470bp and 255bp. XhoI digestion of 5 clones with and without Exon 30 are reported in Figure 33, where as a control we digested the original *MYO5B* plasmid from OriGene before any mutagenesis experiment. Besides clone #3 of full-length *MYO5B* plasmid, any other clone presents the expected fragments length, indicating a correct Exon 30 deletion.

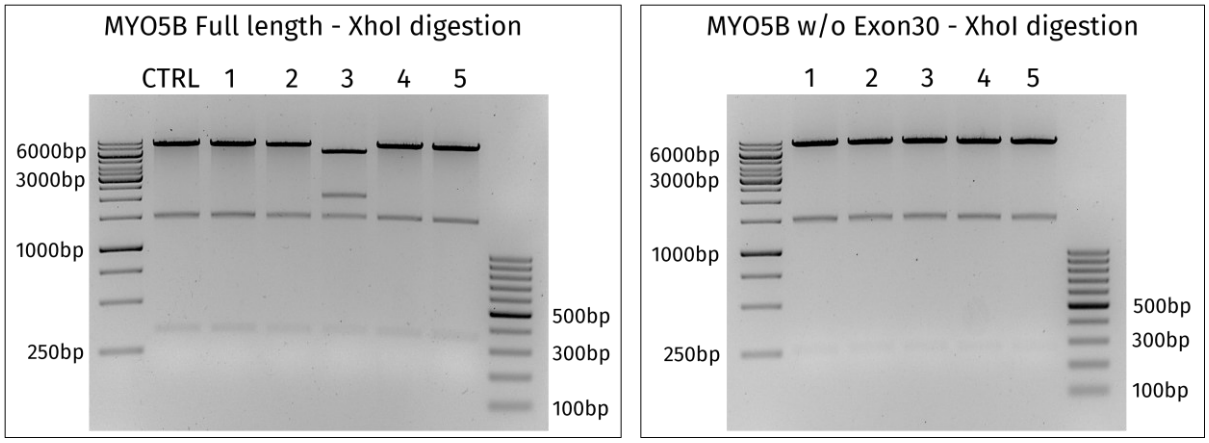

Figure 33: XhoI digestion of BspQI edited clones after Exon 30 deletion with SDM. GeneRuler 1 kb DNA Ladder and GeneRuler 100 bp DNA Ladder by Thermo Fisher Scientific were used as molecular weight marker. CTRL indicates MYO5B OriGene plasmid without any mutagenesis. On the left, CTRL and Clones #1 to #5 with Exon 30 (8600bp, 1470bp, 333 bp); on the right, Clones #1 to #5 without Exon 30 (8600bp, 1470bp, 255 bp).

Thus, we proceeded with cloning both ORF sequences in the specific *in vitro* transcription backbone vector with a HiFi cloning approach based on the Gibson Assembly Cloning. A PCR amplification was performed with the specific HiFi primers (HiFi MYO5B-IVT BB primers from Table 2), and the products were cloned into the previously digested backbone following instruction by *NEBuilder® HiFi DNA Assembly Cloning Kit* by NEB. The positively selected clones were digested with BspQI to verify the linearization of the plasmid (8350bp), as shown in Figure 34-A, where clone #4 represents an example of not successful cloning.

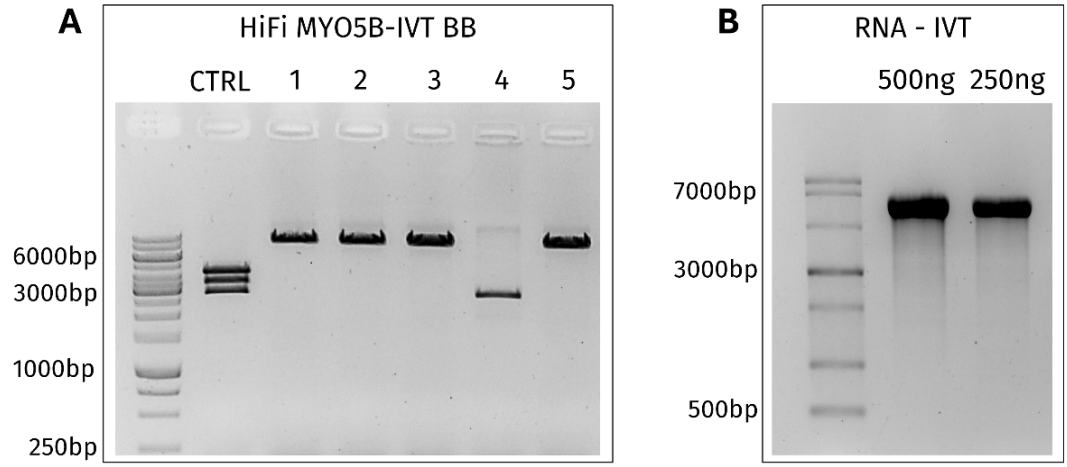

Figure 34: (A): Example of BspQI digestion of ampicillin selected clones after HiFi cloning. GeneRuler 1 kb DNA Ladder by Thermo Fisher Scientific was used as molecular weight marker. CTRL corresponds to the original MYO5B-ORF plasmid from OriGene (4174bp, 3344bp, 2697bp, 210bp). (B): Example of RNA resulting from In Vitro Transcription experiment, ssRNA ladder from NEB as RNA molecular weight marker.

We selected one of the positive clones for each isoform and sequenced the whole plasmid (Microsynth AG); once confirming the sequence accuracy, we advanced with *in vitro*

transcription following *HiScribe® T7 mRNA Kit with CleanCap® Reagent AG* indications from NEB. 500ng and 250ng of the resulting purified mRNA were denatured and loaded on agarose gel to validate integrity and length by electrophoresis (Figure 34-B).

LNP production was performed according to the protocol and optimization kindly shared with us by Doctor Sebastian Hook from the Cell and Gene Therapy group guided by professor Ott at Hannover Medical School (Hook 2023). Table 10 includes a selection of the calculations required for the LNP production and concentration: on the upper lines, the measurements for the *MYO5B* mRNA dilution in citrate, depending on the mRNA length and concentration; the middle part includes the measurement made on the Day 2 of production after the overnight dialysis, when the LNP are concentrated, sterile filtered and aliquoted. Lastly, the bottom lines are the results of the quantification and encapsulation efficiency assay achieved with RiboGreen assay.

For full-length LNP production, we obtained a total of 28 aliquots with 30µl of LNP solution each, concentrated at 145,4 ng/µl, while for Exon 30 depleted *MYO5B* we gained 19 aliquots with 25µl of LNP solution each, concentrated at 64,30 ng/µl; approximately 100ng to 200ng are required for each transfection.

Table 10: Calculation to produce and concentrate full-length MYO5B (Full-length) and Exon 30 depleted MYO5B (w/o Exon30) mRNA-LNPs; length of mRNA and mRNA concentration are the input to start the calculations.

mRNA DILUTION			
	Full-length	**w/o Exon 30**	
Length of mRNA	***6000***	***5922***	***bp***
mRNA concentration	***2260***	***1115***	***ng/µl***
Required RNA concentration in citrate	111,28	111,28	ng/µl
Volume to make mRNA solution	1,80	1,00	ml
Volume of mRNA	88,50	89,70	µl
Volume of citrate	1,709	0,910	ml
LNP PRODUCTION AND CONCENTRATION			
	Full-length	**w/o Exon 30**	
Estimated RNA amount post-production	162,74	62,59	µg
Volume after dialysis	820	500	µl
Add 52,11% sucrose to reach 5% final concentration	87,00	54,00	µl
Final volume	907,00	554,00	µl
Volume after filtering and aliquoting	750,00	475,00	µl
Expected RNA concentration with 100% encapsulation efficiency	179,40	90,39	ng/µl
mRNA ENCAPSULATION QUANTIFICATION			
	Full-length	**w/o Exon 30**	
Exact encapsulation efficiency	81	71	%
Exact encapsulation mRNA concentration	145,40	64,30	ng/µl

6.9. *MYO5B*-LNPs testing on Huh7 cells

Relying on the FLAG-tag located in frame downstream *MYO5B* sequence, we were able to test the produced liver-specific LNPs on a hepatic commercial cell line, the Huh7 cells; this test allowed us to confirm that the mRNA was correctly released inside the hepatocytes and translated into the corresponding protein.

We plated the Huh7 cells on 12mw plates, transfected them with increasing amounts of *MYO5B*-LNP per well, both full-length and Exon 30 depleted isoforms, and after 24 hours we stained them intracellularly with a FITC labelled anti-FLAG antibody and analysed the results through flow cytometry; since the FITC histograms of the LNP transfected samples were

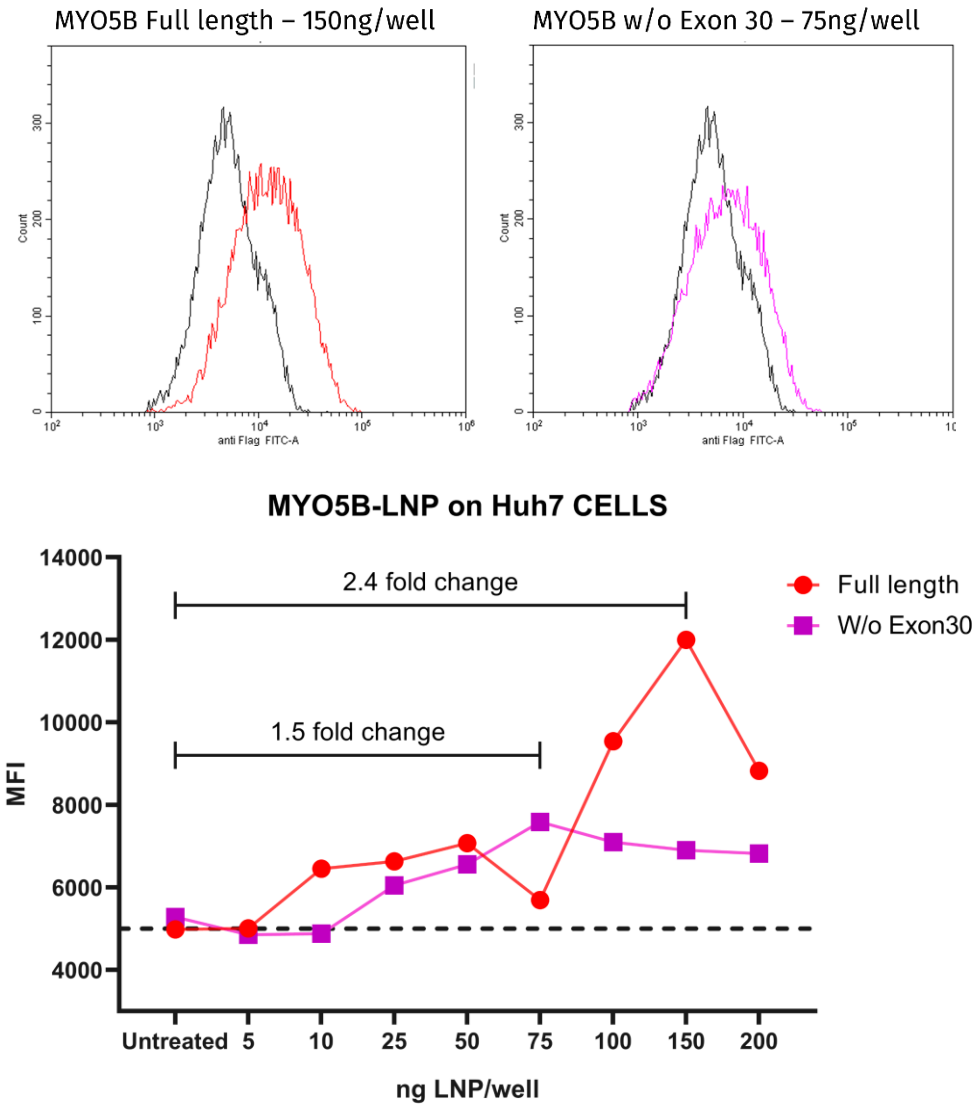

Figure 35: MYO5B-LNPs release test on Huh7 cells. On the upper line, two examples of the FITC fluorescence histograms: on the left, the results of the Huh7 treated with 150ng/well of full-length MYO5B-LNP, in black the untreated control and in red the treated sample; on the right, the resulting histogram of Huh7 cells treated with 75ng/well, in black the untreated control and in purple the treated sample. On the bottom line, the MFI of Huh7 cells treated with increasing concentrations of both MYO5B-LNPs; marked with a horizontal line, the baseline signal of untreated control.

globally shifted compared to the untreated samples, we analysed the results by comparing the MFI (Figure 35).

Full-length MYO5B signal increased in parallel with increasing amount of LNP (with an exception at 75ng/well), reaching a maximum at 150ng/well where the fold change with the signal of untreated cells is about 2,4. Exon 30 depleted MYO5B signal, instead, was overall lower; even so, an increasing MFI related to increasing LNP amount was detected, with the highest fold change of approximately 1,5 at 75ng/well.

Taken together, the results of *MYO5B*-LNPs transfection in Huh7 cells suggest that the mRNA is correctly delivered and translated in the hepatic environment.

6.10. *MYO5B*-LNPs transfection on HC01 organoids

To rescue BSEP-mediated transport function, HC01 organoids were harvested and transfected with *MYO5B* mRNA-LNP as described in the dedicated method section; initially, we tested 2 concentrations of LNPs (200ng and 500ng) and we performed the biliary transport assay 24 hours post LNP transfection, incubating CLF and Tauro-DBD for a total of 90 minutes to ensure maximum transport. The results are shown in Figure 36.

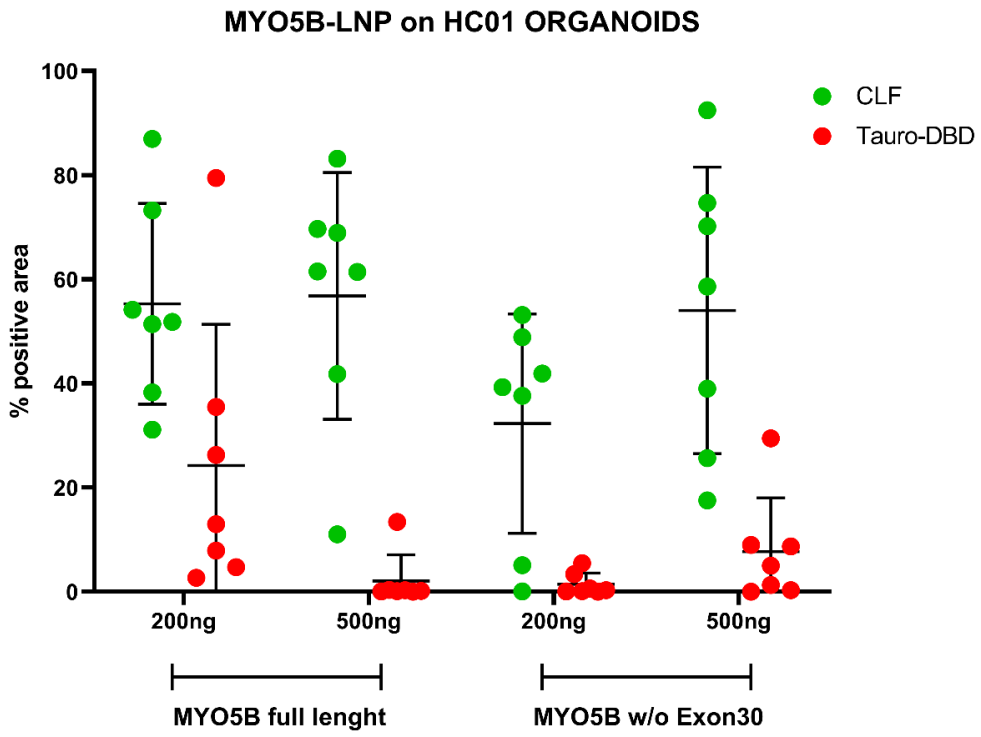

Figure 36: MYO5B mRNA-LNP transfection on HC01 organoids 24 hours after LNP transfection and 90 minutes of CLF and Tauro-DBD incubation. For each time point, every dot corresponds to at least 7 organoids, and the data are represented as the mean ± SD of the percentage of fluorescent positive organoids area. Tauro-DBD transport by MRP2 was possible after MYO5B-LNP transfection and showed a dose-dependency.

On the left, the results of MYO5B full-length overexpression indicate that 200ng of LNP per well are able to increase BSEP mediated transport of the bile acid analogue Tauro-DBD, even though a high variability is existing (200ng = 24,22±25,13; 500ng = 2,07±4,64). On the other hand, the overexpression of MYO5B without Exon 30 seems to be improving BSEP transport only when transfecting 500ng of LNP, even if the Tauro-DBD signal increase is less conspicuous (200ng = 1,43±1,99; 500ng = 7,69±9,55). The overall transport of CLF was not particularly affected in any LNP transfection condition (MYO5B full-length: 200ng = 55,29±17,84; 500ng = 56,80±21,94. MYO5B w/o Exon 30: 200ng = 32,29±19,48; 500ng = 54,03±25,49).

Taking these data into account, we tested the LNP transfection with 200ng of full-length *MYO5B*-LNP and 500ng of Exon 30 deleted *MYO5B*-LNP and we measured the MRP2 and BSEP transport 12, 24 and 36 hours after transfection (Figure 37).

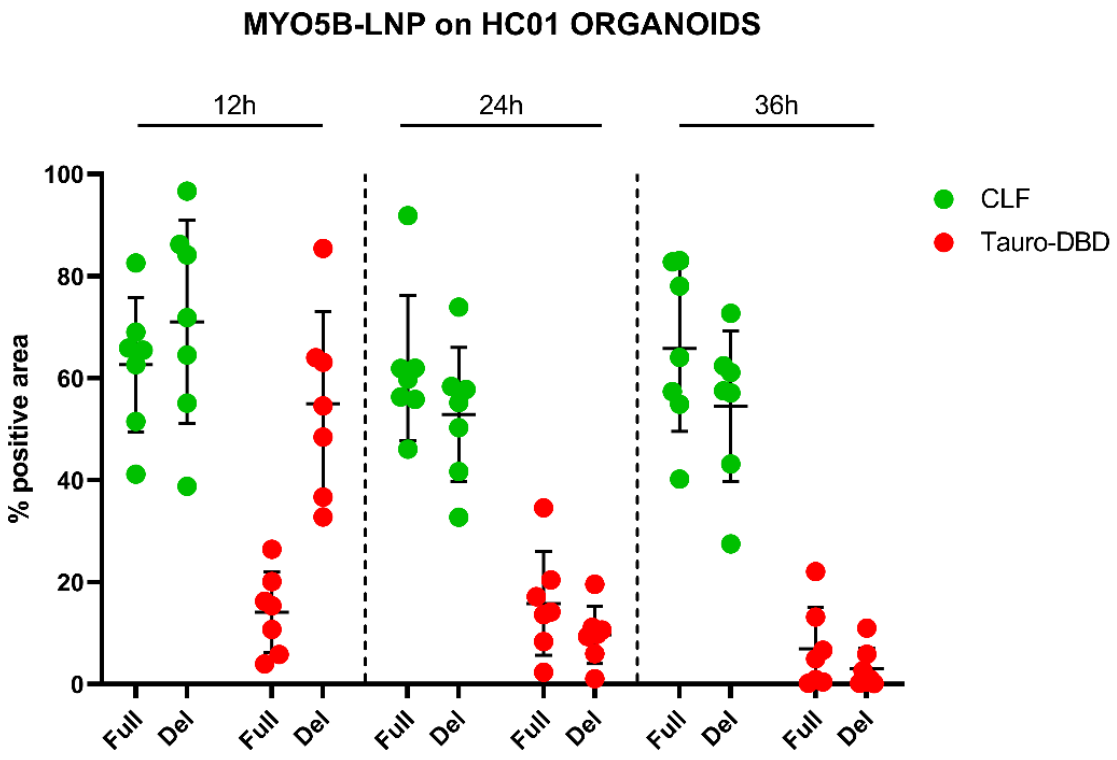

Figure 37: MYO5B mRNA-LNP transfection (full-length MYO5B-LNP, Full, and Exon 30 deleted MYO5B-LNP, Del) on HC01 organoids; 12, 24 and 36 hours after LNP transfection, 90 minutes of CLF and Tauro-DBD incubation. CLF signal didn't show any significant fluctuation between different time points, whereas Tauro-DBD showed a time-dependent and isoform-dependent response.

The CLF green fluorescence signal, indicative of MRP2-mediated transport, showed minimal variation throughout the examined time points, both when overexpressing full-length MYO5B or Exon 30 deleted MYO5B (*12h*: Full = 62,61±13,18; Del = 71,04±19,99. *24h*: Full = 61,96±14,27; Del = 52,85±13,16. *36h*: Full = 65,77±16,24; Del = 54,50±14,77). On the other hand, the red Tauro-DBD fluorescence showed some differences between the time points and

between complete length or Exon 30 deleted *MYO5B* transfection. Interestingly, the highest functional recover of BSEP was detected after 12 hours, by transfecting the protein without Exon 30 (55,00±18,01); this data support the hypothesis that the deleted isoform of MYO5B is liver-specific, however at 24 and 36 hours post LNP transfection the effect on Tauro-DBD transport is much less impacting, showing a time-dependent decrease (*24h*: 9,66±5,61; *36h*: 3,03±4,07). This may imply that the *MYO5B* mRNA is not stable enough in the organoids to maintain an effect over time.

The full-length MYO5B exhibited a less impacting effect on Tauro-DBD at every time point, nevertheless the Tauro-DBD signal was still enhanced compared to non-treated HC01 organoids (*12h*: 14,10±7,93; *24h*: 15,81±10,16; *36h*: 6,92±8,11).

7. DISCUSSION AND CONCLUSION

The liver is a complex metabolic organ organized into functional lobules, where hepatocytes orchestrate the production and secretion of the bile, a crucial process for lipid digestion and toxin excretion. Impairments in the mechanisms regulating bile secretion characterize Progressive Familial Intrahepatic Cholestasis (PFIC), a heterogeneous group of autosomal recessive diseases leading to severe defect in the bile flow and eventually in liver dysfunction. PFIC was initially classified into three subtypes connected with mutation on bile acid transporters genes, but recent genetic advancements have expanded PFIC classification to include defects in other cellular processes including intracellular trafficking, characterized by mutations in the *MYO5B* gene; this subtype of PFIC is now identified as PFIC10 (Roquelaure et al. 2025).

PFIC10 presents as isolated cholestasis characterized by jaundice, chronic pruritus, and hepatomegaly, as well as low to normal gamma-glutamyl transferase (GGT) levels and elevated serum bile acid concentrations. MYO5B is an actin-associated motor protein essential for cell polarity and vesicular transport; its function is regulated by alternative splicing, which may underlie the genotype-phenotype correlation distinguishing intestinal Microvillus Inclusion Disease (MVID) from liver-specific PFIC10 (Bowman et al. 2025). In PFIC10, *MYO5B* mutations typically lead to altered localization of bile acid transporters, resulting in impaired bile flow; however, a subset of patients exhibits correct transporters expression and localization, suggesting that the pathological mechanism is not fully understood and requires further studies (Matarazzo et al. 2022; Cockar et al. 2020).

To investigate these pathogenic mechanisms, adequate *in vitro* models capable of reproducing hepatocyte polarization are required. Current models include different approaches, such as immortalized cell lines and Primary Human Hepatocytes (PHH); however, these models present issue regarding stability and canalicular formation. Induced pluripotent stem cells (iPSCs) are a well-known model that have been developed in the last decade and used in a high variety of disease models (Cerneckis, Cai, and Shi 2024). iPSCs are generated by reprogramming adult somatic stem cells, which can be transfected through several methods with 4 reprogramming factors that reinstate the pluripotent state (Takahashi and Yamanaka 2006). Consequently, iPSCs represents an important advancement in PFIC modelling because of their potential to differentiate into hepatocyte-like cells and 3D organoids that more accurately recapitulate biliary structures and transport functions, offering a robust *in vitro* model (Ju et al. 2024).

The aim of this PhD work was to develop a reproducible and not-invasive *in vitro* hepatic model to investigate pathological mechanisms underneath genetic cholestasis, with a focus on mutation on *MYO5B* gene. In order to be a valid model, the hepatocyte-like cells have to be

arranged in a polarized manner and must be capable of reproducing *in vitro* the hepatocyte biliary transport.

For this project, different cell types of healthy and patient-specific origin were isolated for reprogramming. For a more convenient source, isolated renal epithelial cells from urine samples were used as well as peripheral blood mononuclear cells (PBMCs). Further isolation of CD34 positive cell fraction, an immature PBMC subpopulation, leads to a higher reprogramming efficiency (Ban et al. 2011).

Renal epithelial cells were isolated and expanded from urine starting from published protocols which were further improved by our group at Burlo Garofolo Hospital and by our collaborators at Italian Liver Foundation. Both enhancements improved the outcome of the isolation, in terms of samples that gave rise to cell colonies. Regarding the protocol enhancement we identified at our laboratories, the main differences that positively influenced the cell isolation include a dilution of the urine samples in a media containing FBS, and the resuspension in media containing Rho-associated protein kinase (ROCK) inhibitor until the cells are stable in the Proliferation Medium, confirming the already known ability of this compound to promote cell survival (Watanabe et al. 2007). Despite the differences between the female and male samples in the days following the seeding, no other significant difference was detected once the cell lines were established from the different donors; this confirms that the protocol can be exploited to successfully isolate cells from urine samples regardless of the donor age or gender. Moreover, a small fraction of samples was kept at 4°C for a total of 24 hours, to simulate the storage of a shipment from the patient's house to the laboratories; we were able to isolate the cells from each of these samples, validating again the reproducibility of the enhanced protocol.

These urinary cells were reprogrammed to iPSCs by Doctor Bellarosa group with lentiviral integrating approach following an available published protocol (Zhou et al. 2012).

With the goal of developing a model with broad applicability, we tested and enhanced CRISPR/Cas9 mediated gene editing to insert a *MYO5B* mutation of interest (c.356A>G; p.Tyr119Cys) into wild-type iPSCs genomic DNA. The selected mutation is a missense biallelic mutation described on a patient with paediatric cholestasis; this mutation was indicated as pathological, but the correlated mechanisms were not investigated (Gonzales et al. 2017).

We delivered the Cas9 enzyme and the single guide RNA (SgRNA) as a ribonucleoprotein (RNP) complex through nucleofection on wild-type iPSCs. To promote homology directed repair (HDR) we added a single strand DNA template (ssODN) which sequence included two silent mutations to prevent Cas9 to edit again the successfully knocked-in region. Moreover, the silent mutations allowed an easy selection of the positive clones by a mutation-specific PCR and an insertion-specific restriction enzyme digestion.

Once confirming the efficiency of the designed ssODN, we edited a pool of iPSCs and generated clonal cell lines. Out of 9 clones, 4 were successfully edited and the base change A>G was inserted; it's important to underline that given our results, the silent mutation should be on the same arm as the edit of interest to be more confident that it will be inserted correspondingly. In the clones we analysed, the silent mutation located on the same PAM-distal arm as the edit was always inserted, while the PAM-proximal NdeI silent mutation did not correspond to the edit insertion in every clonal population. This is only a possible explanation that would need additional evidence to be validated.

Regarding CRISPR/Cas9 gene editing, we were able to successfully insert the A>G edit in the iPSCs, developing a method that efficiently transfect these cell line and allow an easy screening of the positive clones; this implies that any mutation of interest on *MYO5B* gene, or possibly any other gene, may be inserted into wild-type iPSCs when the patient's sample is not available.

It should be noted that Cas9-mediated gene editing is nowadays broadly applied in gene therapy studies and disease modelling, and recent advances in research have led to new techniques such as base editing (Lebek et al. 2023) and prime editing (Chen and Liu 2023); the latter methods are safer when performing single-nucleotide editing because the modified enzymes nick one strand of the target DNA, thus resulting in higher efficiency and lower risk of off-targets editing (Gupta and Kumar 2025). These single-strand editing approaches are currently investigated as gene therapies in liver diseases, for example base editing in Alpha-1 antitrypsin deficiency (AATD) have shown promising results (Erion et al. 2025). Therefore, future projects focusing on iPSCs single nucleotide editing to resume PFIC phenotype in *in vitro* models may involve the latest advancements in Cas9-based gene editing.

As a first attempt to establish a cholestatic *in vitro* model, we tested two protocols to differentiate iPSCs to 2D hepatocyte-like cells, one based on a published protocol and the other exploiting a commercial kit; the first was selected due to its extensive validation through multiple assays on HLCs, as well as its reported efficiency and reproducibility (Liu, Lamprecht, and Duncan 2018; Deepak et al. 2020; Liu et al. 2023). The second method, utilizing a STEMCELL Technologies kit, was tested to exploit the consistency of commercial media, despite the current lack of literature describing cell polarity or membrane transporter function.

Both protocols can be divided into 3 main intermediate steps: from iPSCs to definitive endoderm (DE), then hepatic progenitors (HP) and lastly hepatocyte-like cells (HLC). We applied these methods to urine-derived iPSCs, and to compare the results we considered gene expression and protein expression and localisation (Figures 19-23). Both methods showed a decrease of pluripotency genes as the differentiation progressed, with a final undetectable expression in HLC (Figure 19). Alongside, hepatic marker expression increased, exhibiting a strong expression in HLC stage (Figure 20). However, immunofluorescent staining revealed improper localization of the polarization markers: rather than appearing at the expected

basolateral or apical membranes, their signal was distributed throughout the cytoplasm (Figure 21-23). This may have been caused either by incomplete maturation to hepatic stage or by intracellular trafficking disorders.

Taken together, the 2D differentiation data indicated that the generated HLCs exhibited hepatic features based on markers expression, nevertheless the mislocalization of key bile acid membrane transporters suggested an inability to establish proper cell polarity. To investigate PFIC pathological mechanisms, the *in vitro* model we aim to develop must produce cells with a well-organized arrangement and distinct basolateral and apical membrane; therefore, the tested 2D differentiation methods did not meet the desired requirements.

To obtain a polarized hepatic *in vitro* model we proceeded with 3D organoid generation according to the protocol optimized and characterized by prof. Cantz group at Hannover Medical School, where I had the possibility to spend part of my PhD. Liver-mimicking organoids are a recent but very promising disease modelling platform, and iPSCs-derived hepatobiliary organoids represent this advancement thanks to their great ability to resemble the complex architecture of the liver (Wu et al. 2019; Shiota, Samuelson, and Razumilava 2021). Plus, these 3D cultures show interesting potential in drug screening and drug toxicity research (Tan et al. 2026).

We employed the procedure by prof. Cantz group with the urine-derived iPSC lines as well as with 2 blood-derived pluripotent cell lines; the latter iPSC lines where generated from a healthy donor and from a cholestatic patient named HC01; this patient presented a complex clinical picture, suffering from a chronic liver disease and episodes of intrahepatic cholestasis, and genetic analysis revealed the presence of three heterozygous mutation on genes associated with PFIC, specifically *ABCB4*, *ABCB11* and *MYO5B*. HC01 liver biopsies displayed some polarization disturbances, including a cytoplasmatic localisation of membrane bile acid transporters.

Thus, we generated organoids from 4 iPSC lines, 2 blood-derived, a healthy control and patient HC01, and 2 urine-derived, a wild-type line and a *MYO5B* edited line. The resulting organoids were harvested to analyse the biliary transport and underlying transporters localisation.

The control blood-derived organoids showed a proper polarization, meaning that the apical transporters MRP2 and BSEP were detected on the inner canalicular membrane flanking the apical junction marker ZO-1, while the basolateral uptake protein OATP1B1 was detected along the outer membrane and between cells (Figure 26). The transport of the fluorescent bile acid analogues employed for the transport assay showed a time-dependent increase (Figure 30), confirming that the protocol is solid, reproducible and can resume *in vitro* the intracellular hepatocyte transport of bile acids. HC01 organoids, as expected, showed impaired polarization (Figure 26); MRP2 mediated transport appeared comparable to the control, while BSEP mediated transport was completely absent (Figure 31). This latest finding is not perfectly

matching the patient clinical situation and the liver biopsies, since a complete loss of BSEP-associated function normally cause a severe paediatric cholestasis; the observed inconsistency may be attributable to the artificial nature of the organoids: while these have been established as a valid hepatic model – successfully reproducing key functions like biliary transport – they remain a simplification of a complex organ characterized by numerous interacting and mutually influencing elements.

When differentiating iPSCs derived from renal epithelial cells into hepatobiliary organoids, we observed some differentiation defects: the 3D structure of both cell lines, wild-type and *MYO5B* edited, presented an acutely incorrect localisation of apical membrane markers. BSEP and MRP2 exhibited some canalicular localisation but also a cytoplasmatic signal, while OATP1B1 was detected as strongly and diffuse in the cytoplasm (Figure 27). Since both cell lines exhibited the identical issues, we ruled out the gene editing experiments as the likely cause; instead, we first hypothesized that the first step of the differentiation, from iPSCs to foregut endoderm, have not been successful. To verify this possibility, we stained the 2D differentiated epithelial-derived cells with endoderm membrane markers and analysed the results with flow cytometry, staining alongside the PMBCs-derived endoderm as a control. While the control cells showed an intense signal of both markers and a distinct histogram shift, the unstained epithelial-derived endoderm cells fluorescence intensity in the PE detection filter was almost entirely comparable with the stained cells, making it impossible to distinguish between the two (Figure 28). Considering that the reprogramming transgenes presented a dTomato reporter which excitation and emission fluorescence spectrum overlaps with PE spectrum, we supposed that a residual expression of the viral integrated cassette was the reason of this unusually high autofluorescence of the epithelial-derived cells in the PE channel.

To test this option, we performed a PCR on urine-derived iPSCs cDNA to verify the expected complete silencing of the genomic integrated transgenes (Figure 29); unfortunately, the PCR detected a residual expression of pluripotency transgenes, suggesting both a multiple number of integration events and a failure of the cellular endogenous regulatory machinery to achieve complete silencing (Okita, Ichisaka, and Yamanaka 2007). Since the genome inserted transgenes presents Flippase Recognition Target (FRT) sites, further experiments will focus on the use of Flippase-FRT recombination to excise the transgenes (Kuehle et al. 2014) and proceed with the 3D differentiation.

The comparison between the Sendai-virus based reprogramming and the lentiviral integrating method led to the conclusion that the first one is preferred in terms of virus clearance; even if the transgenes integration increases the reprogramming efficiency when using the lentiviral approach, the risk of a high number of integrations and the lack of control on their silencing and expression makes this method less safe, especially when the aim is differentiating the cells and thus driving gene expression towards the phenotype of interest. On the opposite, Sendai-based methodology, even if less efficient as regards iPSCs colonies

number, allows for a quick loss of the viral genes, which do not integrate in the genome and are removed by proliferating cells usually within 6 to 10 passages.

The recent work of prof. Cantz research group demonstrated that gene correcting *MYO5B* mutation in HC01 organoids significantly restored cellular polarity and led to an almost complete rescue of BSEP associated transport, indicating that MYO5B plays a major role in maintaining hepatocyte polarity and biliary transport activity. Following this finding, as a part of this thesis project we attempted a functional recovery of BSEP-mediated transport in HC01 organoids by overexpressing *MYO5B* wild-type delivered as *in vitro* transcripted mRNA encapsulated in liver-specific lipid nanoparticles (LNPs) (Hook 2023). LNPs represent nowadays a useful delivery method, especially *in vivo* to the liver or *in vitro* to hepatocytes; the formulation can be enriched to assure specificity, moreover the introduction of Apolipoprotein E notably increased the LNPs uptake thanks to its binding to hepatic membrane LDL receptor (Sarode et al. 2025).

We purchased a vector containing *MYO5B* full-length ORF sequence and removed with site-directed mutagenesis (SDM) two BspQI restriction sites because of experimental needs; moreover, given the evidence that the functional isoform of MYO5B in the liver might be missing Exon 30 (Roland, Lapierre, and Goldenring 2009), we used the same SDM approach to generate a version of *MYO5B* coding sequence depleted of Exon 30. Both transcripts were used to produce *MYO5B* mRNA, which was lastly encapsulated in liver-specific LNPs; the LNPs formulation and production have been studied and characterized by Professor Ott group at Hannover Medical School, Germany.

To confirm the delivery, release and translation of the mRNA encapsulated in the LNPs, we tested increasing concentration (from 5 to 200 ng/well) into Huh7 cells, a commercial hepatic cell line. To evaluate the protein levels inside the cells we exploited the FLAG tag located at the end of *MYO5B* sequence, which we stained into permeabilized cells with a FITC-labelled antibody and detected the signal with flow cytometry. Both isoforms were correctly delivered and led to the protein production, with an MFI fold change of 2,4 for full-length MYO5B and 1,5 for Exon 30 depleted MYO5B (Figure 35). These data assessed that the LNPs formulation targets hepatocytes and the mRNA that they deliver is intact and can be translated into the corresponding protein, even if Exon 30 depleted MYO5B is less efficient than expected.

We proceeded then by transfecting HC01 organoids; we started by delivering two amounts of LNPs for each isoform in HC01 organoids and selected the one with a highest impact on BSEP mediated transport after 24 hours (Figure 36); the selected concentration was then tested again and the biliary transport was evaluated 12, 24 and 36 hours after transfection. The LNPs delivering of full-length mRNA did not have any significant effect at any time-point on BSEP transport (Figure 37); this result suggests that either this is not the functional isoform of

MYO5B in hepatocytes, or the hypothesized haploinsufficiency is not the cause of BSEP-associated transport defect and overexpressing MYO5B do not bring any benefit.

The Exon 30 depleted version of MYO5B, instead, showed a beneficial effect on BSEP function at 12h time, with a positive signal improvement of 55,00±18,01; however, at 24h and 36h time points this impact rapidly declined (Figure 37). These finding may confirm that the Exon 30 depleted isoform of MYO5B is the biologically active form in liver tissue; even so, the brief duration of the positive effect suggests problems with mRNA stability for extended periods of time or the presence of a cytotoxic effect. Cell response defence mechanisms to exogenous RNA are known (Tang et al. 2023), therefore a deeper investigation is needed to explore the decrease of *MYO5B* mRNA effect over time.

Taken together, the mRNA *MYO5B*-LNPs transfection in HC01 organoids suggested that overexpressing this protein in the hepatic environment is not an effective method to restore MYO5B associated BSEP function impairment in a cholestatic scenario; this implies that other approaches must be pursued to achieve BSEP functional rescue.

In conclusion, through the enhancement of non-invasive cell isolation protocols from urine and peripheral blood, and the development of an efficient CRISPR/Cas9 gene editing strategy for iPSCs, we successfully generated control and cholestatic cell lines. We tested 2D hepatocyte differentiation methods; the resulting cells showed hepatic marker expression, however failed to establish the necessary cell polarity, leading to the mislocalization of key bile acid transporters.

This necessitated a shift to a three-dimensional approach: by employing a validated protocol for hepatobiliary organoid generation, we were able to establish a functional *in vitro* model, where control organoids displayed proper cell polarization and a time-dependent biliary transport, confirming the solid and reproducible nature of the model. The organoids derived from patient HC01, which carried a complex genotype including a *MYO5B* mutation, successfully recapitulated the cholestatic phenotype, thereby validating the 3D organoid model as a powerful tool to study the disease pathological manifestations *in vitro*.

Furthermore, 3D organoids can be a platform to modulate the cholestatic phenotype and attempt a functional rescue; for this purpose, we overexpressed MYO5B by delivering mRNA through liver-specific LNPs, which positively sustained BSEP associated transport. However, the ability to provide lasting benefit was insufficient, suggesting the need of future research to pursue alternative approaches to restore MYO5B-associated BSEP transport impairment.

Taken together, these findings demonstrates that the *in vitro* cellular model developed for this PhD project is a valuable model to investigate and regulate different aspects of MYO5B-associated Progressive Familial Intrahepatic Cholestasis.

8. REFERENCES

Baker, Alastair, Nanda Kerkar, Lora Todorova, Binita M. Kamath, and Roderick H. J. Houwen. 2019. "Systematic Review of Progressive Familial Intrahepatic Cholestasis." *Clinics and Research in Hepatology and Gastroenterology* 43 (1): 20–36. doi:10.1016/j.clinre.2018.07.010.

Baliña-Sánchez, Carmen, Yolanda Aguilera, Norma Adán, Jesús María Sierra-Párraga, Laura Olmedo-Moreno, Concepción Panadero-Morón, Rosa Cabello-Laureano, Catalina Márquez-Vega, Alejandro Martín-Montalvo, and Vivian Capilla-González. 2023. "Generation of Mesenchymal Stromal Cells from Urine-Derived iPSCs of Pediatric Brain Tumor Patients." *Frontiers in Immunology* 14 (January): 1022676. doi:10.3389/fimmu.2023.1022676.

Ban, Hiroshi, Naoki Nishishita, Noemi Fusaki, Toshiaki Tabata, Koichi Saeki, Masayuki Shikamura, Nozomi Takada, et al. 2011. "Efficient Generation of Transgene-Free Human Induced Pluripotent Stem Cells (iPSCs) by Temperature-Sensitive Sendai Virus Vectors." *Proceedings of the National Academy of Sciences* 108 (34). Proceedings of the National Academy of Sciences: 14234–39. doi:10.1073/pnas.1103509108.

Behrendt, Annika, Pegah Golchin, Filip König, Daniel Mulnaes, Amelie Stalke, Carola Dröge, Verena Keitel, and Holger Gohlke. 2022. "Vasor: Accurate Prediction of Variant Effects for Amino Acid Substitutions in Multidrug Resistance Protein 3." *Hepatology Communications* 6 (11): 3098–3111. doi:10.1002/hep4.2088.

Bell, Catherine C., Anita C. A. Dankers, Volker M. Lauschke, Rowena Sison-Young, Roz Jenkins, Cliff Rowe, Chris E. Goldring, et al. 2018. "Comparison of Hepatic 2D Sandwich Cultures and 3D Spheroids for Long-Term Toxicity Applications: A Multicenter Study." *Toxicological Sciences: An Official Journal of the Society of Toxicology* 162 (2): 655–66. doi:10.1093/toxsci/kfx289.

Bell, Catherine C., Delilah F. G. Hendriks, Sabrina M. L. Moro, Ewa Ellis, Joanne Walsh, Anna Renblom, Lisa Fredriksson Puigvert, et al. 2016. "Characterization of Primary Human Hepatocyte Spheroids as a Model System for Drug-Induced Liver Injury, Liver Function and Disease." *Scientific Reports* 6 (May): 25187. doi:10.1038/srep25187.

Bowman, Deanna M., Leslie M. Meenderink, Kyra S. Thomas, Elizabeth H. Manning, Matthew J. Tyska, and James R. Goldenring. 2025. "Microvillus Inclusion Disease-Causing MYO5B Point Mutations Exert Differential Effects on Motor Function." *Journal of Biological Chemistry* 301 (4): 108328. doi:10.1016/j.jbc.2025.108328.

Boyer, James L. 2013. "Bile Formation and Secretion." *Comprehensive Physiology* 3 (3): 1035–78. doi:10.1002/j.2040-4603.2013.tb00519.x.

Bridgman, Paul C., and Mostafa Ahmed. 2009. "Myosin Transport and Neuronal Function," January. Academic Press, 1187–93. doi:10.1016/B978-008045046-9.00709-9.

Bull, Laura N., and Richard J. Thompson. 2018. "Progressive Familial Intrahepatic Cholestasis." *Clinics in Liver Disease* 22 (4): 657–69. doi:10.1016/j.cld.2018.06.003.

Cerneckis, Jonas, Hongxia Cai, and Yanhong Shi. 2024. “Induced Pluripotent Stem Cells (iPSCs): Molecular Mechanisms of Induction and Applications.” *Signal Transduction and Targeted Therapy* 9 (1). Nature Publishing Group: 112. doi:10.1038/s41392-024-01809-0.

Chen, Peter J., and David R. Liu. 2023. “Prime Editing for Precise and Highly Versatile Genome Manipulation.” *Nature Reviews. Genetics* 24 (3): 161–77. doi:10.1038/s41576-022-00541-1.

Cockar, Iram, Pierre Foskett, Sandra Strautnieks, Yasmin Clinch, Jana Fustok, Obydur Rahman, Harry Sutton, et al. 2020. “Mutations in Myosin 5B in Children With Early-Onset Cholestasis.” *Journal of Pediatric Gastroenterology and Nutrition* 71 (2): 184–88. doi:10.1097/MPG.0000000000002740.

Culenova, Martina, Andreas Nicodemou, Zuzana Varchulova Novakova, Michaela Debreova, Veronika Smolinská, Sona Bernatova, Dana Ivanisova, et al. 2021. “Isolation, Culture and Comprehensive Characterization of Biological Properties of Human Urine-Derived Stem Cells.” *International Journal of Molecular Sciences* 22 (22). Multidisciplinary Digital Publishing Institute: 12503. doi:10.3390/ijms222212503.

Deepak, Hiraganahalli Bhaskar, Nellikalaya Shreekrishna, Zaheerbasha Sameermahmood, Niranjan Naranapur Anand, Raghotham Hulgi, Juluri Suresh, Sonal Khare, and Saravanakumar Dhakshinamoorthy. 2020. “An in Vitro Model of Hepatic Steatosis Using Lipid Loaded Induced Pluripotent Stem Cell Derived Hepatocyte like Cells.” *Journal of Biological Methods* 7 (3): e135. doi:10.14440/jbm.2020.330.

Deharde, Daniela, Christin Schneider, Thomas Hiller, Nicolas Fischer, Victoria Kegel, Marc Lübberstedt, Nora Freyer, et al. 2016. “Bile Canaliculi Formation and Biliary Transport in 3D Sandwich-Cultured Hepatocytes in Dependence of the Extracellular Matrix Composition.” *Archives of Toxicology* 90 (10): 2497–2511. doi:10.1007/s00204-016-1758-z.

Di Ciaula, Agostino, Gabriella Garruti, Raquel Lunardi Baccetto, Emilio Molina-Molina, Leonilde Bonfrate, David Q.-H. Wang, and Piero Portincasa. 2017. “Bile Acid Physiology.” *Annals of Hepatology* 16 (November). Elsevier: S4–14. doi:10.5604/01.3001.0010.5493.

Duclaux-Loras, Rémi, Corinne Lebreton, Jérémy Berthelet, Fabienne Charbit-Henrion, Ophelie Nicolle, Céline Revenu des Courtils, Stephanie Waich, et al. 2023. “UNC45A Deficiency Causes Microvillus Inclusion Disease–like Phenotype by Impairing Myosin VB–Dependent Apical Trafficking.” *The Journal of Clinical Investigation* 132 (10). American Society for Clinical Investigation. doi:10.1172/JCI154997.

Ellinger, Philipp, Jan Stindt, Carola Dröge, Katharina Sattler, Claudia Stross, Stefanie Kluge, Diran Herebian, et al. 2017. “Partial External Biliary Diversion in Bile Salt Export Pump Deficiency: Association between Outcome and Mutation.” *World Journal of Gastroenterology* 23 (29): 5295–5303. doi:10.3748/wjg.v23.i29.5295.

Erion, Derek M., Leah Y. Liu, Christopher R. Brown, Stephen Rennard, and Humam Farah. 2025. “Editing Approaches to Treat Alpha-1 Antitrypsin Deficiency.” *CHEST* 167 (2): 444–52. doi:10.1016/j.chest.2024.09.038.

Fleishman, Joshua S., and Sunil Kumar. 2024. “Bile Acid Metabolism and Signaling in Health and Disease: Molecular Mechanisms and Therapeutic Targets.” *Signal Transduction and Targeted Therapy* 9 (1). Nature Publishing Group: 97. doi:10.1038/s41392-024-01811-6.

Gijbels, Eva, Vânia Vilas-Boas, Neel Deferm, Lindsey Devisscher, Hartmut Jaeschke, Pieter Annaert, and Mathieu Vinken. 2019. “Mechanisms and in Vitro Models of Drug-Induced Cholestasis.” *Archives of Toxicology* 93 (5): 1169–86. doi:10.1007/s00204-019-02437-2.

Gonzales, Emmanuel, Sarah A. Taylor, Anne Davit-Spraul, Alice Thébaut, Nadège Thomassin, Catherine Guettier, Peter F. Whitington, and Emmanuel Jacquemin. 2017. “MYO5B Mutations Cause Cholestasis with Normal Serum Gamma-Glutamyl Transferase Activity in Children without Microvillous Inclusion Disease.” *Hepatology (Baltimore, Md.)* 65 (1): 164–73. doi:10.1002/hep.28779.

Guan, Yuan, Dan Xu, Phillip M. Garfin, Ursula Ehmer, Melissa Hurwitz, Greg Enns, Sara Michie, et al. 2023. “Human Hepatic Organoids for the Analysis of Human Genetic Diseases.” *JCI Insight* 2 (17). American Society for Clinical Investigation. doi:10.1172/jci.insight.94954.

Gupta, Pushpendra K., and Sourabh Kumar. 2025. “Third-Generation Novel Technologies for Gene Editing.” *Trends in Biotechnology* 0 (0). Elsevier. doi:10.1016/j.tibtech.2025.07.012.

Hassan, Sara, and Paula Hertel. 2022. “Overview of Progressive Familial Intrahepatic Cholestasis.” *Clinics in Liver Disease* 26 (3): 371–90. doi:10.1016/j.cld.2022.03.003.

Hay, David C., Debiao Zhao, Judy Fletcher, Zoë A. Hewitt, Doris McLean, Alai Urruticoechea-Uriguen, James R. Black, et al. 2008. “Efficient Differentiation of Hepatocytes from Human Embryonic Stem Cells Exhibiting Markers Recapitulating Liver Development in Vivo.” *Stem Cells (Dayton, Ohio)* 26 (4): 894–902. doi:10.1634/stemcells.2007-0718.

Holtzinger, Audrey, Philip R. Streeter, Farida Sarangi, Scott Hillborn, Maryam Niapour, Shinichiro Ogawa, and Gordon Keller. 2015. “New Markers for Tracking Endoderm Induction and Hepatocyte Differentiation from Human Pluripotent Stem Cells.” *Development (Cambridge, England)* 142 (24): 4253–65. doi:10.1242/dev.121020.

Hook, Sebastian Andreas. 2023. “Development of Lipid Nanoparticle-Mediated Delivery of Plasmid DNA for Gene Supplementation Therapy.” https://opac.tib.eu/DB=2/SET=1/TTL=1/SHW?FRST=1.

JEDLITSCHKY, Gabriele, Inka LEIER, Ulrike BUCHHOLZ, Johanna HUMMEL-EISENBEISS, Brian BURCHELL, and Dietrich KEPPLER. 1997. “ATP-Dependent Transport of Bilirubin Glucuronides by the Multidrug Resistance Protein MRP1 and Its Hepatocyte Canalicular Isoform MRP2.” *Biochemical Journal* 327 (1): 305–10. doi:10.1042/bj3270305.

Ju, Ruobing, Siyuan Tian, Yulong Shang, Shuoyi Ma, Miao Zhang, Jingyi Liu, Keshuai Sun, Lina Cui, Xia Zhou, and Ying Han. 2024. “Hepatocyte-like Cells and Liver Organoids:

The Application of iPSCs and Their Derivants for Treating Liver Diseases." *Materials Advances* 5 (21). Royal Society of Chemistry: 8419–31. doi:10.1039/D4MA00373J.

Kaur, Impreet, Ashwini Vasudevan, Preety Rawal, Dinesh M. Tripathi, Seeram Ramakrishna, Savneet Kaur, and Shiv K. Sarin. 2023. "Primary Hepatocyte Isolation and Cultures: Technical Aspects, Challenges and Advancements." *Bioengineering* 10 (2). Multidisciplinary Digital Publishing Institute: 131. doi:10.3390/bioengineering10020131.

Knowles, Byron C., Joseph T. Roland, Moorthy Krishnan, Matthew J. Tyska, Lynne A. Lapierre, Paul S. Dickman, James R. Goldenring, and Mitchell D. Shub. 2014. "Myosin Vb Uncoupling from RAB8A and RAB11A Elicits Microvillus Inclusion Disease." *Journal of Clinical Investigation* 124 (7): 2947–62. doi:10.1172/JCI71651.

König, Jörg, Yunhai Cui, Anne T. Nies, and Dietrich Keppler. 2000. "A Novel Human Organic Anion Transporting Polypeptide Localized to the Basolateral Hepatocyte Membrane." *American Journal of Physiology-Gastrointestinal and Liver Physiology* 278 (1). American Physiological Society: G156–64. doi:10.1152/ajpgi.2000.278.1.G156.

Krishna, Murli. 2013. "Microscopic Anatomy of the Liver." *Clinical Liver Disease* 2 (Suppl 1): S4–7. doi:10.1002/cld.147.

Kuehle, Johannes, Soeren Turan, Tobias Cantz, Dirk Hoffmann, Julia D Suerth, Tobias Maetzig, Daniela Zychlinski, et al. 2014. "Modified Lentiviral LTRs Allow Flp Recombinase–Mediated Cassette Exchange and *In Vivo* Tracing of 'Factor-Free' Induced Pluripotent Stem Cells." *Molecular Therapy* 22 (5): 919–28. doi:10.1038/mt.2014.4.

Le Vee, Marc, Emilie Jigorel, Denise Glaise, Philippe Gripon, Christiane Guguen-Guillouzo, and Olivier Fardel. 2006. "Functional Expression of Sinusoidal and Canalicular Hepatic Drug Transporters in the Differentiated Human Hepatoma HepaRG Cell Line." *European Journal of Pharmaceutical Sciences* 28 (1): 109–17. doi:10.1016/j.ejps.2006.01.004.

Lebek, Simon, Francesco Chemello, Xurde M. Caravia, Wei Tan, Hui Li, Kenian Chen, Lin Xu, Ning Liu, Rhonda Bassel-Duby, and Eric N. Olson. 2023. "Ablation of CaMKIIδ Oxidation by CRISPR-Cas9 Base Editing as a Therapy for Cardiac Disease." *Science (New York, N.Y.)* 379 (6628): 179–85. doi:10.1126/science.ade1105.

Li, Chao Zheng, Hiromi Ogawa, Soon Seng Ng, Xindi Chen, Eriko Kishimoto, Kokoro Sakabe, Aiko Fukami, et al. 2022. "Human iPSC-Derived Hepatocyte System Models Cholestasis with Tight Junction Protein 2 Deficiency." *JHEP Reports* 4 (4). doi:10.1016/j.jhepr.2022.100446.

Li, Peilin, Daisuke Miyamoto, Masayuki Fukumoto, Yuta Kawaguchi, Mampei Yamashita, Hanako Tetsuo, Tomohiko Adachi, et al. 2024. "Generation of Human Hepatobiliary Organoids with a Functional Bile Duct from Chemically Induced Liver Progenitor Cells." *Stem Cell Research & Therapy* 15 (August): 269. doi:10.1186/s13287-024-03877-z.

Li, Qinghong. 2023. *MYO5B in Health and Disease*. [Groningen]: University of Groningen. doi:10.33612/diss.675737136.

Liu, Jui-Tung, Caren Doueiry, Yu-lin Jiang, Josef Blaszkiewicz, Mary Paige Lamprecht, James A. Heslop, Yuri K. Peterson, et al. 2023. "A Human iPSC-Derived Hepatocyte Screen Identifies Compounds That Inhibit Production of Apolipoprotein B." *Communications Biology* 6 (1). Nature Publishing Group: 452. doi:10.1038/s42003-023-04739-9.

Liu, Jui-Tung, Mary Paige Lamprecht, and Stephen A. Duncan. 2018. "Using Human Induced Pluripotent Stem Cell-Derived Hepatocyte-like Cells for Drug Discovery." *Journal of Visualized Experiments : JoVE*, no. 135 (May): 57194. doi:10.3791/57194.

Lou, Yue, Yao Lv, Jindan Yu, Weizhong Gu, Ming Jiang, and Jie Chen. 2024. "MYO5B Gene Mutations May Promote the Occurrence of Very Early Onset Inflammatory Bowel Disease: A Case Report." *BMC Medical Genomics* 17 (July): 187. doi:10.1186/s12920-024-01962-z.

Matakovic, Lavinija, Arend W. Overeem, Karin Klappe, and Sven C. D. van IJzendoorn. 2022. "Induction of Bile Canaliculi-Forming Hepatocytes from Human Pluripotent Stem Cells." In *Hepatocytes: Methods and Protocols*, edited by Naoki Tanimizu, 71–82. Methods in Molecular Biology. New York, NY: Springer US. doi:10.1007/978-1-0716-2557-6_4.

Matarazzo, Lorenza, Anna Monica Bianco, Emmanouil Athanasakis, Marco Serveres, Paola Francalanci, Giovanna Cenacchi, Giuseppe Maggiore, and Adamo Pio D'Adamo. 2022. "MYO5B Gene Mutations: A Not Negligible Cause of Intrahepatic Cholestasis of Infancy With Normal Gamma-Glutamyl Transferase Phenotype." *Journal of Pediatric Gastroenterology and Nutrition* 74 (5). doi:10.1097/MPG.0000000000003399.

Namipashaki, Atefeh, Kealan Pugsley, Xiaodong Liu, Kirra Abrehart, Sue Mei Lim, Guizhi Sun, Marco J. Herold, Jose M. Polo, Mark A. Bellgrove, and Ziarih Hawi. 2023. "Integration of Xeno-Free Single-Cell Cloning in CRISPR-Mediated DNA Editing of Human iPSCs Improves Homogeneity and Methodological Efficiency of Cellular Disease Modeling." *Stem Cell Reports*, November, S2213671123004150. doi:10.1016/j.stemcr.2023.10.013.

Nelson, Leonard J., Katie Morgan, Philipp Treskes, Kay Samuel, Catherine J. Henderson, Claire LeBled, Natalie Homer, M. Helen Grant, Peter C. Hayes, and John N. Plevris. 2017. "Human Hepatic HepaRG Cells Maintain an Organotypic Phenotype with High Intrinsic CYP450 Activity/Metabolism and Significantly Outperform Standard HepG2/C3A Cells for Pharmaceutical and Therapeutic Applications." *Basic & Clinical Pharmacology & Toxicology* 120 (1): 30–37. doi:10.1111/bcpt.12631.

Nirgude, Snehal, Elisia D. Tichy, Zhengfeng Liu, Sanam L. Kavari, Rose D. Pradieu, Mariah Byrne, Feikun Yang, et al. 2025. "Single-Nucleus Multiomic Analysis of Beckwith-Wiedemann Syndrome Liver Reveals PPARA Signaling Enrichment and Metabolic Dysfunction." *Communications Biology* 8 (March): 495. doi:10.1038/s42003-025-07961-9.

Noé, Johannes, Bruno Stieger, and Peter J. Meier. 2002. “Functional Expression of the Canalicular Bile Salt Export Pump of Human Liver.” *Gastroenterology* 123 (5): 1659–66. doi:10.1053/gast.2002.36587.

Okita, Keisuke, Tomoko Ichisaka, and Shinya Yamanaka. 2007. “Generation of Germline-Competent Induced Pluripotent Stem Cells.” *Nature* 448 (7151). Nature Publishing Group: 313–17. doi:10.1038/nature05934.

Penman, Sophie L., Parveen Sharma, Hélène Aerts, B. Kevin Park, Richard J. Weaver, and Amy E. Chadwick. 2019. “Differential Toxic Effects of Bile Acid Mixtures in Isolated Mitochondria and Physiologically Relevant HepaRG Cells.” *Toxicology in Vitro* 61 (December): 104595. doi:10.1016/j.tiv.2019.104595.

Pinon, Michele, and Binita M. Kamath. 2024. “What’s New in Pediatric Genetic Cholestatic Liver Disease: Advances in Etiology, Diagnostics and Therapeutic Approaches.” *Current Opinion in Pediatrics* 36 (5): 524. doi:10.1097/MOP.0000000000001380.

Qiu, Yi-Ling, Jing-Yu Gong, Jia-Yan Feng, Ren-Xue Wang, Jun Han, Teng Liu, Yi Lu, et al. 2017. “Defects in Myosin VB Are Associated with a Spectrum of Previously Undiagnosed Low Γ-glutamyltransferase Cholestasis.” *Hepatology* 65 (5): 1655. doi:10.1002/hep.29020.

Roland, Joseph T., David M. Bryant, Anirban Datta, Aymelt Itzen, Keith E. Mostov, and James R. Goldenring. 2011. “Rab GTPase–Myo5B Complexes Control Membrane Recycling and Epithelial Polarization.” *Proceedings of the National Academy of Sciences of the United States of America* 108 (7): 2789–94. doi:10.1073/pnas.1010754108.

Roland, Joseph T., Lynne A. Lapierre, and James R. Goldenring. 2009. “Alternative Splicing in Class V Myosins Determines Association with Rab10 *.” *Journal of Biological Chemistry* 284 (2). Elsevier: 1213–23. doi:10.1074/jbc.M805957200.

Roquelaure, Bertrand, Marco Sciveres, Tassos Grammatikopoulos, Eberhard Lurz, Folke Freudenberg, Dalila Habes, Lionel Thevathasan, Fatine Elaraki, and Emmanuel Gonzales. 2025. “Odevixibat Therapy in Progressive Familial Intrahepatic Cholestasis with MYO5B Variants: A Retrospective Case Series.” *Orphanet Journal of Rare Diseases* 20 (May): 227. doi:10.1186/s13023-025-03728-x.

Saran, Chitra, and Kim L. R. Brouwer. 2023. “Hepatic Bile Acid Transporters and Drug-Induced Hepatotoxicity.” *Toxicologic Pathology* 51 (7–8). SAGE Publications Inc: 405–13. doi:10.1177/01926233231212255.

Sarode, Ashish, Christian Ortiz, Tadeh Derstepanian, Natalia Vargas-Montoya, Priyal Patel, Nikita Khadse, Saikat Manna, et al. 2025. “Potent Liver-Tropic mRNA Lipid Nanoparticles: ApoE-Mediated Delivery Through a Low-Density Lipoprotein Receptor Independent Uptake Mechanism.” *Advanced Materials (Deerfield Beach, Fla.)*, November, e17893. doi:10.1002/adma.202517893.

Schneider, Caroline A., Wayne S. Rasband, and Kevin W. Eliceiri. 2012. “NIH Image to ImageJ: 25 Years of Image Analysis.” *Nature Methods* 9 (7). Nature Publishing Group: 671–75. doi:10.1038/nmeth.2089.

Sgodda, Malte, Evelyn Gebel, Lennart Dignas, Susanne Alfken, Reto Eggenschwiler, Amelie Stalke, Carola Dröge, et al. 2025. “iPSC-Based Hepatic Organoids Reveal a Heterozygous MYO5B Variant as Driver of Intrahepatic Cholestasis.” *Hepatology Communications* 9 (10): e0812. doi:10.1097/HC9.0000000000000812.

Shinozawa, Tadahiro, Masaki Kimura, Yuqi Cai, Norikazu Saiki, Yosuke Yoneyama, Rie Ouchi, Hiroyuki Koike, et al. 2021. “High-Fidelity Drug-Induced Liver Injury Screen Using Human Pluripotent Stem Cell–Derived Organoids.” *Gastroenterology* 160 (3). Elsevier: 831-846.e10. doi:10.1053/j.gastro.2020.10.002.

Shiota, Junya, Linda C. Samuelson, and Nataliya Razumilava. 2021. “Hepatobiliary Organoids and Their Applications for Studies of Liver Health and Disease: Are We There Yet?” *Hepatology (Baltimore, Md.)* 74 (4): 2251–63. doi:10.1002/hep.31772.

Suleman, Saqlain, Sharmin Alhaque, Andrew Guo, Aaron Zhang, Serena Fawaz, Stefany Perera, Mohammad S. Khalifa, Hassan Rashidi, David C. Hay, and Michael Themis. 2025. “Transcriptomic Profiling of iPS Cell-Derived Hepatocyte-like Cells Reveals Their Close Similarity to Primary Liver Hepatocytes.” *Cells* 14 (12): 925. doi:10.3390/cells14120925.

Suominen, Siiri, Tinja Hyypijev, Mari Venäläinen, Alma Yrjänäinen, Hanna Vuorenpää, Mari Lehti-Polojärvi, Mikko Räsänen, et al. 2023. “Improvements in Maturity and Stability of 3D iPSC-Derived Hepatocyte-like Cell Cultures.” *Cells* 12 (19). Multidisciplinary Digital Publishing Institute: 2368. doi:10.3390/cells12192368.

Takahashi, Kazutoshi, and Shinya Yamanaka. 2006. “Induction of Pluripotent Stem Cells from Mouse Embryonic and Adult Fibroblast Cultures by Defined Factors.” *Cell* 126 (4). Elsevier: 663–76. doi:10.1016/j.cell.2006.07.024.

Tan, Shiyi, Yun Yang, Li Ma, Xulei Zuo, Jianhua Rao, Yuepu Pu, Feng Cheng, Zhongze Gu, and Juan Zhang. 2026. “Ceritinib-Ibuprofen Synergistic Hepatotoxicity: Insights from Real-World Data and Liver Organoid Models.” *Toxicology* 519 (January): 154321. doi:10.1016/j.tox.2025.154321.

Tang, Danxu, Yan Liu, Chundi Wang, Lifang Li, Saleh A. Al-Farraj, Xiao Chen, and Ying Yan. 2023. “Invasion by Exogenous RNA: Cellular Defense Strategies and Implications for RNA Inference.” *Marine Life Science & Technology* 5 (4): 573–84. doi:10.1007/s42995-023-00209-7.

Targher, Giovanni, Christopher D. Byrne, and Herbert Tilg. 2024. “MASLD: A Systemic Metabolic Disorder with Cardiovascular and Malignant Complications,” April. BMJ Publishing Group. doi:10.1136/gutjnl-2023-330595.

Tayhan, Seçil Erden, Gönül Tezcan Keleş, İsmet Topçu, Erol Mir, and Saime İsmet Deliloğlu Gürhan. 2017. “Isolation and in Vitro Cultivation of Human Urine-Derived Cells: An Alternative Stem Cell Source.” *Turkish Journal of Urology* 43 (3): 345–49. doi:10.5152/tud.2017.93797.

Trivedi, Darshan V., Suman Nag, Annamma Spudich, Kathleen M. Ruppel, and James A. Spudich. 2020. “The Myosin Family of Mechanoenzymes: From Mechanisms to

Therapeutic Approaches." *Annual Review of Biochemistry* 89 (June): 667–93. doi:10.1146/annurev-biochem-011520-105234.

Vij, Mukul, and Vaibhav Shah. 2022. "Compound Heterozygous Myosin 5B (Myo5b) Mutation with Early Onset Progressive Cholestasis and No Intestinal Failure." *Fetal and Pediatric Pathology* 41 (5): 811–17. doi:10.1080/15513815.2021.1959690.

Vitale, Giovanni, Marco Sciveres, Claudia Mandato, Adamo Pio d'Adamo, and Angelo Di Giorgio. 2025. "Genotypes and Different Clinical Variants between Children and Adults in Progressive Familial Intrahepatic Cholestasis: A State-of-the-Art Review." *Orphanet Journal of Rare Diseases* 20 (February): 80. doi:10.1186/s13023-025-03599-2.

Watanabe, Kiichi, Morio Ueno, Daisuke Kamiya, Ayaka Nishiyama, Michiru Matsumura, Takafumi Wataya, Jun B. Takahashi, et al. 2007. "A ROCK Inhibitor Permits Survival of Dissociated Human Embryonic Stem Cells." *Nature Biotechnology* 25 (6). Nature Publishing Group: 681–86. doi:10.1038/nbt1310.

Wu, Fenfang, Di Wu, Yong Ren, Yuhua Huang, Bo Feng, Nan Zhao, Taotao Zhang, Xiaoni Chen, Shangwu Chen, and Anlong Xu. 2019. "Generation of Hepatobiliary Organoids from Human Induced Pluripotent Stem Cells." *Journal of Hepatology* 70 (6). Elsevier: 1145–58. doi:10.1016/j.jhep.2018.12.028.

Zahumenska, Romana, Vladimir Nosal, Marek Smolar, Terezia Okajcekova, Henrieta Skovierova, Jan Strnadel, and Erika Halasova. 2020. "Induced Pluripotency: A Powerful Tool for In Vitro Modeling." *International Journal of Molecular Sciences* 21 (23): 8910. doi:10.3390/ijms21238910.

Zhang, Zhonghui, Yongxing Gao, Albert Gordon, Zack Z. Wang, Zhijian Qian, and Wen-Shu Wu. 2011. "Efficient Generation of Fully Reprogrammed Human iPS Cells via Polycistronic Retroviral Vector and a New Cocktail of Chemical Compounds." *PLOS ONE* 6 (10). Public Library of Science: e26592. doi:10.1371/journal.pone.0026592.

Zheng, Yu, Yuming Peng, Shuju Zhang, Hongmei Zhao, Weijian Chen, Yongjia Yang, Zhengmao Hu, Qiang Yin, and Yu Peng. 2022. "Case Report: MYO5B Homozygous Variant c.2090+3A>T Causes Intron Retention Related to Chronic Cholestasis and Diarrhea." *Frontiers in Genetics* 13 (May). Frontiers. doi:10.3389/fgene.2022.872836.

Zhou, Ting, Christina Benda, Sarah Dunzinger, Yinghua Huang, Jenny Cy Ho, Jiayin Yang, Yu Wang, et al. 2012. "Generation of Human Induced Pluripotent Stem Cells from Urine Samples." *Nature Protocols* 7 (12). Nature Publishing Group: 2080–89. doi:10.1038/nprot.2012.115.

UNIVERSITÀ
DEGLI STUDI
DI TRIESTE

La borsa di dottorato è cofinanziata con risorse dell'Unione Europea, NextGeneration EU - Piano Nazionale di Ripresa e Resilienza, Missione 4 – Componente 1 – Investimento 4.1 CUP J92B22000940007